

PVMaT Improvements in the BP Solar Photovoltaic Module Manufacturing Technology

**Final Subcontract Report
4 May 1998—30 November 2001**

J. Wohlgemuth and S. Shea
*BP Solar
Frederick, Maryland*



NREL

National Renewable Energy Laboratory

1617 Cole Boulevard
Golden, Colorado 80401-3393

NREL is a U.S. Department of Energy Laboratory
Operated by Midwest Research Institute • Battelle • Bechtel

Contract No. DE-AC36-99-GO10337

PVMaT Improvements in the BP Solar Photovoltaic Module Manufacturing Technology

**Final Subcontract Report
4 May 1998—30 November 2001**

J. Wohlgemuth and S. Shea
*BP Solar
Frederick, Maryland*

NREL Technical Monitor: R.L. Mitchell

Prepared under Subcontract No. ZAX-8-17647-05



NREL

National Renewable Energy Laboratory

1617 Cole Boulevard
Golden, Colorado 80401-3393

NREL is a U.S. Department of Energy Laboratory
Operated by Midwest Research Institute • Battelle • Bechtel

Contract No. DE-AC36-99-GO10337

NOTICE

This report was prepared as an account of work sponsored by an agency of the United States government. Neither the United States government nor any agency thereof, nor any of their employees, makes any warranty, express or implied, or assumes any legal liability or responsibility for the accuracy, completeness, or usefulness of any information, apparatus, product, or process disclosed, or represents that its use would not infringe privately owned rights. Reference herein to any specific commercial product, process, or service by trade name, trademark, manufacturer, or otherwise does not necessarily constitute or imply its endorsement, recommendation, or favoring by the United States government or any agency thereof. The views and opinions of authors expressed herein do not necessarily state or reflect those of the United States government or any agency thereof.

Available electronically at <http://www.osti.gov/bridge>

Available for a processing fee to U.S. Department of Energy
and its contractors, in paper, from:

U.S. Department of Energy
Office of Scientific and Technical Information
P.O. Box 62
Oak Ridge, TN 37831-0062
phone: 865.576.8401
fax: 865.576.5728
email: reports@adonis.osti.gov

Available for sale to the public, in paper, from:

U.S. Department of Commerce
National Technical Information Service
5285 Port Royal Road
Springfield, VA 22161
phone: 800.553.6847
fax: 703.605.6900
email: orders@ntis.fedworld.gov
online ordering: <http://www.ntis.gov/ordering.htm>



PREFACE

This Final Technical Progress Report covers the work performed by BP Solar for the period May 4, 1998 to November 30, 2001 under DOE/NREL Subcontract # ZAX-8-17647-05 entitled "PVMaT Improvements in the BP Solar Photovoltaic Module Manufacturing Technology".

The following personnel at BP Solar have contributed to the technical efforts covered in this report.

Fiore Artigliere	Scott Chen
James Cliber	Mark Conway
Tomas Corman	Joseph Creager
George Kelly	Bonnie Kinsey
Timothy Koval	Mohan Narayanan
William Poulin	Steve Roncin
Madhumita Roy	Paul Schneider
Jay Shaner	Stephen Shea
Doug Stark	Mark Susol
Timothy Tomlinson	John Wohlgemuth
Haibin Yu	

BP Solar has been supported by subcontracts at the Automation and Robotics Research Institute at the University of Texas at Arlington (ARRI), at Specialized Technology Resources, Inc., SiNaF Products, Inc. and the Physics Department at North Carolina State University.

ARRI staff that worked on the subcontract included:

Heather Beardsley	Raul Fernandez
Peter Tanguy	

STR staff that worked on the subcontract included:

James Galica	Norman Sherman
Daniel Wells	

SiNaF Products staff that worked on the subcontract included:

Ronald Gehringer

NCSU work on the subcontract was performed under the direction of Professor Gerald Lucovsky.

Gratings Incorporated staff that worked on the subcontract included:

Saleem Zaidi

EXECUTIVE SUMMARY

The objective of this three year PVMaT program was to continue the advancement of BP Solar PV manufacturing technologies in order to design and implement a process which produces polycrystalline silicon PV modules that can be sold profitably for \$2.00 per peak watt or less and which increases the production capacity of the Frederick plant to at least 25 megawatts per year. Achieving these major objectives was based on meeting the following specific task goals.

Develop a process to produce silicon feedstock from Na_2SiF_6 that can be sold profitably for less than \$15/kilogram in large quantities. Demonstrate the process in a pilot facility.

Optimize and improve control of the casting process to increase the process yield (kilograms of silicon out divided by kilograms of silicon in) by 7% and to improve material quality such that average cell efficiency increases by 4%.

Reduce the center-to-center cut distance on the wire saw to less than 450 μm in production, and develop a wire saw process that reduces the consumable costs by at least \$0.05/wafer, that does not require organic cleaners nor result in generation of hazardous waste material.

Develop, demonstrate and implement a cost-effective cell process that produces a minimum average cell efficiency of 15% and improves the cell line electrical yield by 5% when applied to BP Solar cast polycrystalline silicon wafers.

Develop and qualify an encapsulation system that meets all technical and reliability requirements and can be laminated and cured in less than 6 minutes.

Improve BP Solar's product and materials handling (including efforts in at least 3 separate areas) to increase line yield by 3% and reduce handling labor to save \$0.05/watt.

Improve process measurement and control in the production line (including efforts in at least 3 separate areas) to improve yield by 3% and reduce rework by 50%.

ACCOMPLISHMENTS

Accomplishments during the program include:

- Developed processes to produce high purity SiF_6 gas from a number of available commercial sources.
- Developed relationships with silicon feedstock vendors to ensure long-term supplies of feedstock and control costs.
- Designed and implemented a new control system for casting. Added features, alarms and troubleshooting functions that contributed to a 4% increase in yield.
- Designed and implemented an automatic loading and unloading system for casting.
- Verified the relationship between higher minority carrier lifetime in cast Si and the resultant cell efficiency. BP Solar is now tracking material quality by making measurements of minority carrier lifetime for each production casting.
- Verified that large-scale casting furnaces produced cast silicon with characteristics equivalent to that cast in the older, smaller stations. Successfully transferred the large-scale casting process to production, resulting in expanded casting capacity.
- Reduced the wire saw pitch to 450 microns with no loss in downstream yield.

- Demonstrated the ability to separate and recycle the components of the wire saw cutting slurry.
- Demonstrated the ability to change from oil-based to glycol-based slurry.
- Re-tooled several older saws to increase their capacity by 40%.
- Demonstrated that the wire saws are capable of cutting wafers down to 140 microns or thinner with reasonable quality and yield.
- Identified and demonstrated a new method for finding cracked wafers in real-time either before or after metallization.
- Demonstrated in full production an 8% improvement in average cell efficiency using PECVD silicon nitride.
- Developed and implemented low-maintenance production dopant applicator with higher uptime and reduced process variability.
- Demonstrated advanced processes using silicon nitride to enable cell efficiency up to 15% with a reduced-footprint equipment set.
- Developed a technology roadmap for implementation of high-efficiency processes in all BP Solar factories in 2002.
- Developed a new EVA formulation and demonstrated a 6 minute process to achieve adequate cure of PV modules in standard lamination equipment.
- Designed and debugged a new automated assembly line for large area modules. The new line reduced rework, increased yield and improved labor productivity by 50%.
- Demonstrated an improved soldering head configuration and initiated a study of the soldering process in order to develop an improved control method.
- Implemented a factory wide data collection and tracking system. Production volumes and performance parameters are now monitored in real time through the local area network. The network is being expanded to other BP Solar factories.

TABLE OF CONTENTS

<u>Section</u>		<u>Page</u>
1.0	Introduction	1
2.0	Baseline Process	3
3.0	PVMaT Program Efforts	5
3.1	Silicon Feedstock Development	5
3.1.1	Raw Materials Generating Silicon Tetrafluoride Gas	5
3.1.2	Gas Reduction and Silicon Production	8
3.1.3	Future Efforts	14
3.2	Casting Optimization and Control	15
3.2.1	66 kg Station Development	15
3.2.2	240 kg Station Implementation	17
3.3	Wire Saw Cost	19
3.3.1	Wafer Thickness	19
3.3.2	Slurry Reclaim	21
3.3.3	Wire Saw Cost Reductions	21
3.4	Cell Process Development	22
3.4.1	Selective Emitter	22
3.4.2	PECVD Silicon Nitride	27
3.4.3	New Doper Process	28
3.4.4	Fast-cure Silver Ink and Rotary Print	28
3.4.5	RIE Texturing of Polycrystalline Silicon	29
3.4.6	Silicon Nitride AR Coating – Understanding the mechanism for improved performance	35
3.5	Faster Cure Encapsulant	42
3.5.1	Faster Curing Encapsulation System	42
3.5.2	Moisture Vapor Transmission Rate	66
3.5.3	Flame Retardant EVA	67
3.5.4	Cure Monitoring	73
3.6	Handling	75
3.6.1	Assembly Automation	75
3.6.2	Ceramic Handling	82
3.6.3	Handling in Casting	88
3.6.4	Handling in Cell Line	89
3.7	Measurement and Control	89
3.7.1	Brick ID System	89
3.7.2	Doping and Diffusion Measurements / MES	89
3.7.3	Vision Inspection of Solder Tab	90
3.7.4	Wafer Fracture Detection	91
	References	94

LIST OF FIGURES

<u>Figure</u>	<u>Page</u>
1 New Casting Stations	17
2 Cell Efficiency and Current versus Brick Lifetime Measurement	18
3 Wire Saw Wafer Thickness	20
4 Sawing Yields	20
5 Selective Emitter Profiles for Junction Analysis	25
6 Optical Scattering from Texture Features	29
7 SEM Pictures of Three Random RIE Texture Profiles	30
8 Spectral Reflectance Measurements for Several Textured Surfaces	30
9 Efficiency and J_{SC} Measurements for RIE Textured Cells – no RCA Clean	31
10 Efficiency and J_{SC} Measurements for RIE Textured cells – with RCA Clean	32
11 Efficiency and J_{SC} Measurements for RIE Textured Cells – with RCA Clean and Nitric DRE	33
12 Internal Quantum Efficiency and Reflectance for RIE-textured Cells with and without Nitric DRE	33
13 Efficiency for Small Area, RIE Textured Devices Fabricated at Georgia Tech with and without Nitric DRE	34
14 Short Circuit Current for Small Area, RIE Textured Devices Fabricated at Georgia Tech with and without Nitric DRE	35
15 Stack System for the Diffusion Experiment.	37
16 The ND and NH FTIR Peaks for the 10Å Samples	38
17 D and H Bond Density Inverse Temperature Dependence	39
18 SIMS Profile of the Diffusion Stack System after 900°C Anneal	40
19 Moving Die Rheometry Results @ 150°C	55
20 Moving Die Rheometry Results @ 155°C	55
21 Moving Die Rheometry Results @ 160°C	56
22 Lay-up of the Prototype Laminates	58
23 UV Stability of Candidate Formulations vs. 15295P Control	61
24 Moving Die Rheometry Results @ 150°C	62
25 Stress–strain Curve of EVA films with Different Degrees of Crosslinking	74
26 Glass Handling Vacuum Pickup	76
27 Cell Tabbing Machine	77
28 Cell Stringing Machine	77
29 Transport, Inspection Table and Lay-up Buffer	78
30 Automatic Load-Unload Laminator	78
31 Transport Tables, Rotary Table for trim and Flip Table for Inspection	79
32 Framing Magazine and Butyl Pump	79
33 Automatic Framing Table	80
34 Vacuum Module Lift and Solar Simulator	80
35 Flip Table for Final Inspection	81
36 Boxing System	81
37 Ball Mold Rack	85
38 Stages that Occur during the Ball Drying Process	87
39 New Ingot Loading Cart – Extended	88
40 New Ingot Loading Cart – In Place	88
41 Solder Reflow Inspection Using Vision System	90

LIST OF TABLES

<u>Table</u>	<u>Page</u>
1 Cast Polycrystalline Si Process Sequence	3
2 Gas Impurities within the Sampled SiF ₄	7
3 GDMS Analysis of SiNaF Si from Run 1	9
4 GDMS Analysis of SiNaF Si from Run 2	10
5 GDMS Analysis of SiNaF Si from Run 3	11
6 GDMS Analysis of SiNaF Si from Run 4	12
7 Gti Casting Station Experimental Results	18
8 Selective Emitter RTC Trial 5	24
9 Selective Emitter RTC Trial 6	26
10 Shimadzu SiN CVD fire through Trial –3	27
11 Chemical Reactions Involving Si _x N _y H _z likely in Silicon Nitride.	41
12 Candidate Encapsulant Resin Percent Light Transmission Values	44
13 Percent Moisture and Volatile Content of EVA Resin and EVA-Based Encapsulant	46
14 Results of “Faster-Curing” Lamination Trials	48
15 EVA Processing Experiments	50
16 Gel Contents vs. Peroxide Type, Curative Concentration, and Platen Temperature	51
17 Gel Contents vs. Curative & Concentration at 10 Minutes at 166°C	51
18 Gel Contents of 15295P EVA vs. Lamination Temperature	51
19 Gel Content Determination Using Larger Laminates vs. TBEC Concentration	52
20 Modified X15303P EVA at TBEC Peroxide Concentration E	53
21 Modified X15303P EVA at TBEC Peroxide Concentration D	53
22 Modified X15303P EVA at Alternative Curative Concentration E	53
23 Qualification of the Gel Test Results	54
24 Cure Level of Laboratory Laminate Specimens Prepared @ 140°C	57
25 Moving Die Rheometry Results for the Faster-Curing Formulations vs. the Controls	57
26 Time to Achieve Full Cure of Control @ Process Temperature	58
27 Six-Minute Lamination Trial Results	59
28 Five-Minute Lamination Trial Results	59
29 Physical Properties of Candidate Encapsulant	60
30 Key Physical Properties of X34643-4P versus 15295P at 80% Cure Level	61
31 Brabender Processing Trials of Candidate Faster-Curing EVA	63
32 Key Physical Properties of Prototype X34928-4P EVA	64
33 Cure Level Comparisons of X34928-4P Faster-Curing EVA vs. 15295P	65
34 Moisture Vapor Transmission Rates and Adhesion Properties of Candidate Encapsulants	67
35 Flame Retardant Reactivity Temperatures	68
36 Description of the Prototype MSX-60 Fire Resistant PV Modules	71
37 Flammability Resistance of Various Candidate Substrates	72
38 NMR Measurements of EVA Film Crosslinking Density	75
39 Viscosity of Common Liquids	82
40 Dispensing Equipment Classification	84
41 Test of Shunted Cells on Crack Detection System	93

1.0 INTRODUCTION

The goal of BP Solar's Crystalline PVMaT program was to improve the Polycrystalline Silicon manufacturing facility to reduce cost, improve efficiency and increase production capacity. Key components of the program were:

- Develop a solar-grade silicon feedstock.
- Optimize and improve process control in casting.
- Reduce wire diameter and wafer thickness to reduce silicon feedstock requirements.
- Reduce wire saw operating costs.
- Develop a faster cure encapsulant to reduce labor and equipment requirements.
- Increase cell efficiency and use more robust processes.
- Improve handling and eliminate non-value added handling steps.
- Improve measurement and control throughout the production line.

The results of these efforts were to reduce PV module production costs, to increase the production capacity of the Frederick plant to at least 25 megawatts per year and to improve the average cell efficiency to 15%, a secondary effect of which is to reduce the customer's balance of systems (BOS) costs. These goals were to be achieved while improving the already high reliability of the crystalline silicon modules.

Four subcontractors supported BP Solar in this effort:

1. SiNaF Products, Inc. worked on developing a process and the equipment necessary to produce a solar-grade silicon feedstock.
2. Specialized Technology Resources, Inc. (STR) worked on development, qualification and production of a faster cure encapsulation system.
3. Automation and Robotics Research Institute of the University of Texas at Arlington assisted BP Solar in developing equipment for automated handling and improved measurement and control on the production line.
4. North Carolina State University supported BP Solar in characterizing silicon nitride films and determining how these films can be used to passivate BP Solar cast polycrystalline silicon.

The baseline for this PVMaT program is the polycrystalline process and production line as it existed at the conclusion of BP Solar's previous PVMaT Contract NREL # ZAI-4-11294-01 entitled "Cast Polycrystalline Silicon Photovoltaic Manufacturing Technology Improvements".^{1, 2} This baseline is described in more detail in Section 2.0.

The rationale behind this program was to identify specific areas in the baseline process where improvements in handling, process control or the process itself could significantly reduce cost, increase efficiency and/or improve capacity. In addition to these process issues, a materials availability analysis indicated that silicon feedstock must be addressed for the long-term success of crystalline silicon PV.

Most of BP Solar's (and the crystalline Si PV industry's) silicon feedstock is scrap purchased from the semiconductor industry. Until 1995 most of this material consisted of tops and tails purchased at low cost. In 1995 a shortage of semiconductor grade silicon lead the crystal growers to follow the PV industry lead and reuse their own tops and tails. As the supply of tops and tails dried up, BP Solar and the rest of the PV industry were forced to find new sources of silicon feedstock. While this shortage has alleviated due to the down turn in semiconductor sales, the cost has never returned to pre-shortage levels, nor will the available supply of scrap be adequate to meet the needs of an expanding PV industry.

Therefore, BP Solar worked with SiNaF Products, Inc. to develop a solar-grade silicon process to produce the large quantities of silicon feedstock necessary to support growth in the PV industry. BP Solar has also worked with existing silicon feedstock manufacturers to identify variations in the manufacturing process that could lead to lower manufacturing costs for the vendor and thence to lower feedstock costs for BP Solar.

The casting stations, as configured at the start of the contract, were limited in the amount of data that they could collect and in the number and variety of parameters they could control. Production data showed that average cell efficiency and yields varied considerably from station to station and even from run to run in the same station. Efforts were made to improve control and to optimize the casting process leading to improvements in both yields (casting and cell line) and material quality, which translate into higher average cell efficiencies.

In 2001 BP Solar identified an external vendor to provide large capacity casting stations for the expansion of the BP Solar Frederick casting facility. Material quality from these stations was shown to be equivalent to that made in the BP Solar baseline stations. Advanced control systems on these units had the potential for improved run-to-run repeatability.

The wire saw technology is still evolving and improving. A number of potential changes have been identified that can reduce cost and increase even further the number of wafers/cm of brick that can be cut, thereby reducing the amount of silicon necessary per watt of modules produced.

Work on cell processing is designed to increase the average cell efficiency to 15% (at Standard Test Conditions) while improving process control and reducing the overall module manufacturing cost. Areas of investigation include new process steps (PECVD silicon nitride AR coating and selective emitter diffusion) and modifications to some of the present process steps (doping, edge isolation and screen printing) to develop a more robust process sequence, that is easier to control to achieve higher yields and better efficiency.

The present "Fast Cure" EVA encapsulation system is a significant improvement over the old "Standard Cure" system. However, even with this system, increasing production volume still requires a significant investment in lamination equipment, plant floor space and handling equipment. STR worked on developing a new encapsulation system, with the goal of reducing the lamination time to less than 6 minutes.

Although most cell and wafer handling functions have been automated or are in the process of being automated, there are still a number of areas in the plant where handling improvements can significantly reduce labor cost and/or improve yield. ARRI assisted BP Solar in identifying those areas in which improvements in handling can have the greatest impact on reducing cost and increasing capacity.

Improved measurement and control during processing should lead to improved yields and higher average cell efficiency. Three specific areas in the plant have been identified, where additional inline measurements are expected to significantly improve control of the process.

First and second year efforts in each of these technical areas were discussed in the first two annual report^{3,4}. These efforts, along with work done in the third contract year, will be discussed in detail in Section 3.0.

2.0 BASELINE PROCESS

BP Solar's Crystalline Silicon Technology is based on use of cast polycrystalline silicon wafers. The process flow at the end of NREL Contract # ZAI-4-11294-01 is shown in Table 1.⁵

Table 1
Cast Polycrystalline Si Process Sequence

**Casting
of
9 Brick Ingots**

Wire Saw Wafering

**Cell Process
(All Print with Al BSF)**

**Module Assembly
(XY Positioners)**

**Lamination
(Fast Cure EVA)**

Finishing

The various segments of BP Solar's module manufacturing process as practiced at the beginning of this PVMaT program are described below.

Casting

BP Solar had developed and patented a directional solidification casting process specifically designed for photovoltaics⁶. In this process, silicon feedstock is melted in a ceramic crucible and solidified into a large grained semicrystalline silicon ingot. During BP Solar's earlier PVMaT program the size of the cast ingot was increased so that each ingot yielded 9 - 11.4 cm by 11.4 cm bricks. This change was implemented in production resulting in a significant reduction in operating costs and in a doubling of the casting capacity at approximately 20% of the cost that would have been required if the same amount of capacity was added by purchasing new casting stations.

Wafering

During the previous PVMaT Program BP Solar developed wire saw technology for cutting large area polycrystalline wafers. The major advantages of wire saws are the reduced kerf and increased production volume. During the course of the previous PVMaT program we demonstrated:

- That each new wire saw cut as many wafers as 22 to 24 ID saws.
- Wire saws can cut wafers on 475 μm centers versus 600 μm centers for the ID saws, resulting in at least 20% more wafers from each cast ingot.
- Wire saws can cut larger wafers (in our case 11.4 cm by 15.2 cm and 15.2 cm by 15.2 cm) while the ID saws are limited by the blade diameter.

All of BP Solar's wafering is now done with wire saws.

Cell Process

The cell process sequence is based on the use of Thick Film Paste (TFP) metallization, where a commercially available screen-printed silver paste is applied as the current carrying grid on the front of the solar cell. This process has been designed to be as cost effective as possible. The high temperature process steps, including: diffusion, firing of the front and back print pastes and Chemical Vapor Deposition (CVD) of a TiO₂ antireflective (AR) coating are all performed in belt furnaces.

During the previous PVMaT Program, BP Solar developed a cost effective aluminum paste back surface field (BSF) process. This process was implemented on the BP Solar production line, using a fully automated screen-printing system provided by Baccini. The system has provided a 6.5% increase in average cell efficiency.

Module Assembly

The first part of the module assembly sequence is to solder two solder plated copper tabs onto the front of the solar cells. BP Solar procured new automated machines to perform the tabbing operation. Tabbed cells are then laid up into a matrix and the tabs are then soldered to the backs of the solar cells using XY positioners developed in the previous PVMaT program.

Module Lamination

The module construction consists of a low iron, tempered glass superstrate, EVA encapsulant and a Tedlar backsheet. The lamination process, including the cure, is performed in a vacuum lamination system. Then the modules are trimmed and the leads are attached. Finally, every module is flash tested to determine its STC power output.

3.0 PVMAT PROGRAM EFFORTS

The following sections detail the progress made during the three year program.

3.1 Silicon Feedstock Development

In this effort, BP Solar worked with subcontractor, SiNaF Products, Inc. to develop a process to produce silicon feedstock from commercial grade H_2SiF_6 that can be sold profitably for less than \$15/kilogram in large quantities. The approach of the subcontract was to combine the work previously completed by SRI International with the ongoing SiNaF activities to produce a low cost silicon feedstock for the PV industry.

The SRI work was completed under DOE and Jet Propulsion Laboratory (JPL) grants (references) with private and industry funding between 1976 and 1986. The result of their work demonstrated the feasibility of the process by producing silicon, which was subsequently used to make state-of-the-art solar cells. The SRI process is divided into two separate segments. The first is the generation of an intermediate silicon containing gas from a by-product salt of the phosphate fertilizer industry. SRI only demonstrated that the gas could be produced by their process, but did not generate this gas to produce their silicon. The second segment is the reduction of this gas with sodium metal to generate solar grade silicon feedstock.

SiNaF's activities focused on identifying environmentally sensitive materials that could be reprocessed to allow the accumulation, separation and economical delivery of the contained metals. During this work a silicon containing gas was generated and found compatible with the work of SRI. These activities were first centered on fly ash, which is generated by the combustion of coal in power plants. The second group of materials to be considered was spent catalysts from the petroleum industry. Work concentrated on the spent fluidized catalytic cracking material, because of the large volume going into landfills in the United States. The third material was a by-product of the phosphate fertilizer industry from which the SRI gas generating material was derived. The fourth was hard rock mine and mill tailings. The fly ash proved impractical because it contained too much unburned coal. The spent catalyst, phosphate fertilizer by-product and the tailings materials represent an almost unlimited raw material source for the production of the intermediate gas and therefore the production of solar grade silicon.

Under this subcontract, SiNaF demonstrated the feasibility for the production of the intermediate gas from the three raw material technologies. However, it was gas generated from the phosphate fertilizer by-product using SiNaF technology, that was used in the production of silicon in this effort. The gas generation and reduction technologies developed by SiNaF, have the potential to be more economic and of higher efficiency than those developed by SRI International.

The next section, 3.1.1, describes the gas generation work performed during the contract. The following sections, 3.1.2, discusses the effort to produce silicon from the specified gases. Finally, section 3.1.3 discusses the next steps necessary to commercialize the SiNaF process for producing solar grade silicon feedstock.

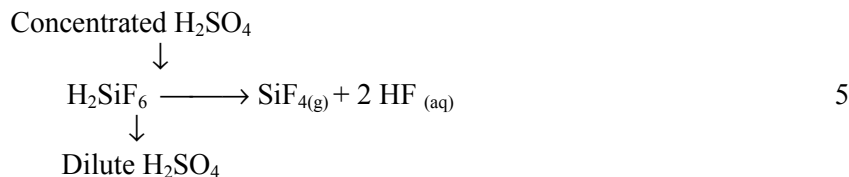
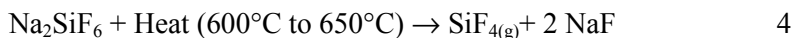
3.1.1 Raw Materials Generating Silicon Tetrafluoride Gas

Phosphate Fertilizer By-product Discussion

Silicon tetrafluoride (SiF_4) gas is generated from two (2) by-products of the phosphate fertilizer industry, sodium fluosilicate (Na_2SiF_6), a salt, and fluosilicic acid (H_2SiF_6), a 20% to 50% concentrated aqueous acid. The sodium fluosilicate salt is generated by the sodium hydroxide (NaOH) neutralization of the acid (see equation 1), the precipitation with sodium fluoride (NaF) (see equation 2), and the silicon tetrafluoride capture by sodium fluoride (NaF) at 200°C (see equation 3).



The SiF_4 gas is generated from Na_2SiF_6 salt by thermal decomposition (see equation 4) or by the dehydration with sulfuric acid (H_2SO_4) of H_2SiF_6 aqueous acid (see equation 5).



SRI's proposed process combines equations 2 and 4. These reactions generate the gas as well as recycle the NaF salt. The steps include mixing, precipitation, filtration, production of hydrofluoric acid (HF) and drying of the Na_2SiF_6 before its thermal decomposition. The thermal decomposition of the Na_2SiF_6 salt is carried out between 600°C and 650°C. As demonstrated by SRI the purity of the gas is sufficient to provide a gas feed for the reduction process.

In SiNaF's study of the SRI process, references were identified stating that during the thermal decomposition of the Na_2SiF_6 salt the product NaF became "sticky" and adhered to the contact heat exchange surfaces. To prevent this stickiness from lowering the heat exchange capability a system of scrapers would have to be installed in the rotating drum of the decomposition furnace. Therefore, the design of the decomposition furnace must include two sets of gas tight seals at each end of the rotating drum. This would be an expensive system without a guarantee that it would work. SiNaF abandoned the SRI process for gas generation.

Gas Generation from Fluosilicic Acid

After an extensive review of literature pertaining to the production of SiF_4 , hydrofluoric acid (HF) and hydrogen fluoride (HF), SiNaF began laboratory investigation of the direct dehydration of the H_2SiF_6 with sulfuric acid (H_2SO_4). A design was developed and equipment purchased for a laboratory gas generation system using this technology. This system provided gas generation for all evaluations and reduction runs carried out by SiNaF during the program. Using this equipment, continuous gas production was only limited by the storage tank capacity, 36 liters at 100 psi, of the system.

With the assistance of Sandia National Laboratories, a comparative analysis between a sample of SiF_4 generated by SiNaF and a commercial sample obtained from MEMC was completed. The Fourier Transform Infrared Spectroscopy (FTIR) comparative estimates, provided in Table 2, are believed to be good to within a 25% error of the reported number.

The result of this comparative study was very encouraging, since not only can the gas be generated using this technology, but the purity of the gas is equal to or surpasses that which is currently in commercial production. These results have allowed SiNaF to optimize the process allowing easy scaling to pilot plant and production gas generation volumes.

Table 2
Gas Impurities within the Sampled SiF₄

Origin of Generated Gas Sample	Hydrogen Fluoride (HF)	Hydrogen Chloride (HCl)
SiNaF Products, Inc.	25 ppm	15 ppm
MEMC	40 ppm	500 ppm

The primary feed material (H₂SiF₆) for gas generation is produced as a by-product of the phosphate fertilizer industry. This acid is over produced by that industry. However, the over production is not sufficient to meet the photovoltaic (PV) industry projected needs for silicon based on future expansion plans. This has led SiNaF to search for and identify other inexpensive starting materials that can supplement the raw material supply. The technologies developed by SiNaF for added gas production have established an almost unlimited raw material base for the production of PV grade silicon.

Gas Generation from Spent Petroleum Catalysts

A US Patent was issued to Ronald Gehringer in Sept. 1993⁷. This process patent described the production of silicon tetrafluoride gas starting with a spent petroleum catalyst. A newly developed process technology has superseded this patented technology. This new process technology has lowered the capital costs of the process by an order of magnitude. In addition, an increase in efficiency has been demonstrated in the associated metal separation and recovery processes.

This work is very timely in another respect. In February 2000 the Environmental Protection Agency (EPA) issued new guidelines for the disposal of spent catalysts from the petroleum refining industry. The leach-able content of the heavy metals has been lowered to below that achievable with current disposal technology. The method developed by SiNaF could solve this disposal problem for the petroleum refining industry. SiNaF and the industry have discussed a fee associated with the delivery of this material to SiNaF. The net results of these negotiations could result in a negative raw material cost for the production of silicon by SiNaF Products, Inc.

SiNaF's current efforts centers around this spent fluidized catalytic cracking material. However, these efforts can be expanded to include any silica/alumina (SiO₂/Al₂O₃) matrix materials. The SiNaF digestion process liberates a silicon containing gas that is then used to produce PV grade silicon. Because this gas is generated and then consumed, it will be referred to as the intermediate gas.

In addition to producing PV grade silicon, the matrix metals of the spent catalyst, mainly aluminum, are recoverable. After removal of the silica for silicon and the alumina for aluminum, the non-digested and soluble residual "trace" metals are reduced to between 10% and 15% of the original spent catalyst volume. About half of this material is a non-digested solid while the residual soluble metals comprise from 2% to 5% of the original matrix.

Based upon a 50:50 ratio of silica (SiO₂) to alumina (Al₂O₃), SiNaF will need to digest 25,000 pounds of the spent material per day to produce 1,000 metric tons of solar grade silicon feedstock annually. In addition, 7,500 tons of aluminum salt, 120 tons of titania, and about 250 tons of other metals including gallium (Ga) and germanium (Ge) could be recovered per year. This technology would remove approximately 4,500 tons of spent catalyst from further environmental concern for every 1,000 metric ton per year of silicon produced.

Gas Generation from Hard Rock Mine and Mill Tailings

The “endless supply” of available hard rock mine and mill tailings produced over the some 150 years of mining activity in the US, provides an unlimited raw material source of silica (SiO_2). One source of this material is located in the southwest corner of New Mexico, and can be delivered for \$7.00 per standard ton. This is equivalent to \$10.00 per ton of silica or \$20.00 per ton or \$40 per metric ton of converted silicon. Most locations are rural and located near railroad routes, thereby minimizing exposure of hazardous conditions to populated areas. With millions of tons on private and Bureau of Land Management (BLM) lands, this may be the lowest cost raw material for the production of silicon.

The study of the mineralogy of the New Mexico mine tailing deposit has resulted in the identification of the silica containing minerals of quartz, muscovite and clinocllore. The non-silica minerals include magnetite, hematite, calcite and rutile. During one type of laboratory experiment, an acid digestion of the tailings resulted in an acid solution and non-digested solids. The acid solution contained recoverable quantities of manganese (Mn), copper (Cu), zinc (Zn), lead (Pb), strontium (Sr), and molybdenum (Mo). The non-digested solids were density separated with the heavy fraction containing mainly magnetite (Fe_3O_4) and rutile (TiO_2), while the lighter fraction contained 88% silica (SiO_2). The 88% silica content fraction contained quartz (SiO_2) and muscovite (a potassium aluminosilicate mineral) for a combined 96% recovery. The 88% silica content is sufficient to be used as a feed for the silica digestion process to generate SiF_4 effectively. Both the acid solution metals and the heavy fraction are capable of further processing for their metals recovery.

3.1.2 Gas Reduction and Silicon Production

In the SiNaF Products process, the SiF_4 gas is reacted directly with molten sodium to produce silicon with sodium fluoride as a by-product. Materials analysis has shown that the SiF_4 gas produced by SiNaF Products is pure enough to be used directly in the reduction process. The sodium metal is available from DuPont in the purity and quantities required.

A small research reactor was designed and built for development and demonstration of the reduction process. The reactor consists of:

- A sodium chamber where a four (4) pound brick of sodium is heated to 110°C to melt;
- A pressurized container of silicon tetrafluoride (SiF_4) gas;
- Mass flow controllers and check valves; and
- A reaction chamber capable of being preheated to above 150°C , the reaction initiation temperature.

In the process, sodium is melted and forced into the reaction chamber with a flow of argon. After preheating the reaction chimney and reaction crucible to above 150°C , the reaction initiation temperature, the liquid sodium and gaseous SiF_4 react producing silicon (Si), sodium fluoride (NaF), and heat. The cooling fluid of both the reaction chimney and reaction crucible will dissipate the heat. The temperature range for the controlled reaction is between 800°C and 1200°C .

Using the exiting gas flow calibration curve, the SiF_4 gas flow was adjusted to establish minimal exit gas flow equilibrium conditions. After flow equilibrium was established, only monitoring and recording of data were needed. The end of the run was determined by the increase in flow rate (from zero (0) to set point) through the sodium melt pot signifying the complete transfer of the reaction sodium. At this point, the SiF_4 gas feed was terminated, still allowing for an argon purge. Argon was also allowed to purge the SiF_4 and sodium pot transfer tube lines for safety. The furnace was allowed to ramp down in temperature until ambient conditions were obtained.

To date there have been four reduction runs completed. During each of the first three runs, the reaction containment did not proceed as originally designed. The main problem in containment resulted from the interaction of the graphite linings with the sodium metal liquid and/or vapor. As this interaction proceeded, the graphite expanded far beyond that expected by simple thermal expansion. This graphite expansion resulted in fracturing and rupturing the outer ceramic crucible in Runs I and III and caused severe spalling during Run II. In Run II the product stalagmite that formed reached the bottom of the gas inlet tubes and caused reaction product to accumulate there. This apparently allowed liquid sodium to contact the graphite of the chimney resulting in its expansion and failure of the chimney ceramic. It was observed that in all the runs the silicon carbide gas inlet tubes and stainless steel sodium inlet tube were not affected by the reduction process.

Reduction Run I

With the failure of the ceramic/graphite bottom crucible, only a small amount of material could be collected. Care was taken to avoid crucible graphite contamination of the sample but it was not 100% effective. This material was washed and sent out for Glow Discharge Mass Spectroscopy (GDMS) elemental analysis. The results for run 1 are given in Table 3. Those elements not listed were determined to be present at less than the detection limit of the analysis.

Table 3: GDMS Analysis of SiNaF Si from Run 1

Element	Concentration (ppmwt)
Li	0.05
B	0.5
C	~900
N	~140
O	~ 6 wt %
Na	Matrix
Mg	11
Al	35
Si	Matrix
P	4.8
S	3.5
Cl	~0.6 wt %
L	17
Ca	58
Ti	1.5
V	0.05
Cr	1.2
Mn	0.,54
Fe	7.7
Ni	-.98
As	0.91
Sr	0.84
Y	0.06
Zr	1.7
Ba	0.16
La	0.04
Ce	0.06
Pb	0.48

In examining data from Run I, the following issues were identified:

- Na is a matrix material so much of the feedstock Na has not been removed.
- The ~900 ppm (wt) of C, indicating excess reaction of the chamber walls.
- The ~ 140 ppm (wt) of N, probably indicating excess air.
- The 6 wt% O also indicating excess air and that the fine powder probably oxidized after formation, likely during washing.
- Many of the other impurities may have been introduced because the sample was washed in tap water. Future samples should either not be washed or be washed only in DI water.
- The ratio of iron, chromium and nickel are consistent with the composition of 316 stainless steel. This contamination is likely due to the corrosion of the stainless steel in the gas compression, storage system and transfer lines to the reactor. With a better engineered system this corrosion source could be rectified.

Reduction Run II

When the reactor was opened, a stalagmite was observed within the crucible assembly. It was metallic gray in color and about 9 inches in length and 1 inch in diameter. The top of the stalagmite apparently plugged the gas inlet orifice causing the failure as described above. As the material from the chimney was being removed it was observed to contain a significant proportion of un-reacted sodium metal. No, or very little, sodium metal was observed in processing of the stalagmite.

The stalagmite material and the debris around the stalagmite were crushed and washed with water and then with a 10% solution of hydrofluoric acid (HF). During this process the sodium silicate (Na_2SiO_3) and sodium carbonate (Na_2CO_3) phases dissolved while all of the other phases increased in concentration. Hot water and 10% HF were again used to wash the material, followed by a final water rinse.

The GDMS results for run 2 are given in Table 4. Those elements not listed were determined to be present at less than the detection limit of the analysis.

Table 4: GDMS Analysis of SiNaF Si from Run 2

Element	Concentration (ppmwt)
Li	0.7
B	25
C	Matrix
N	Matrix
O	Matrix
F	Matrix
Na	Matrix
Mg	60
Al	1300
Si	Matrix
P	2
S	150
Cl	100
K	80
Ca	800
Ti	20
V	3.5
Cr	3
Mn	1.5
Fe	130
Co	0.5

Element	Concentration (ppmwt)
Ni	10
Cu	10
As	0.7
Sr	30
Y	8
Zr	0.9
Nb	0.25
Mo	0.5
Sb	2
Te	5
Ba	5

Matrix elements include C, N, O, Na, F and Si. The C, N and O are likely due to air leaking into the gas generation system and to the washing procedures used to prepare these samples. Improvements to the equipment and with improved handling of the reactant product should reduce the level of C, N and O contamination. Removal of the Na and F will require re-melting.

Reduction Run III

The reduction reaction during Run III resulted in a rupture of the outer ceramic crucible and generated a problem with the furnace such that it could not be used to heat the reaction products to the melting point of NaF. A washing procedure was carried out on the resultant material. During the washing, a gas was noted evolving from the solution. Silicon reacts with water producing amorphous silica (SiO₂) and hydrogen (H₂). The result of this was to dissolve the smaller particle sized Si thus decreasing the crystalline Si content and allowing the identification of calcium silicide (CaSi₂) in the reaction product. Hot water washing increased the Si content. Several additional hot water rinses resulted in weight loss with no observable increase in Si concentration, but with a substantial decrease in NaF concentration.

The GDMS results for run 3 are given in Table 5. Those elements not listed were determined to be present at less than the detection limit of the analysis.

Table 5: GDMS Analysis of SiNaF Si from Run 3

Element	Concentration (ppmwt)
B	15
C	Matrix
N	~2000
O	Matrix
F	Matrix
Na	Matrix
Mg	15
Al	200
Si	Matrix
P	7
S	20
Cl	170
K	300
Ca	200
Ti	3

Element	Concentration (ppmwt)
V	0.9
Cr	2
Mn	0.5
Fe	20
Co	0.5
Ni	4
Cu	15
As	0.5
Sr	0.5
Y	0.5
Zr	0.5

The results are similar to, but a little better than run 2.

Reduction Run IV

Run IV was accomplished with a bottom crucible made of 316 stainless steel to study its usage as a reaction containment material. A sodium inlet orifice was used to better control the sodium flow. The furnace equilibrium temperature was established at 800°C and reaction initiated. With no apparent contact between liquid sodium and the graphite of the chimney, the same graphite/ceramic failure as described above was observed. This failure indicates that graphite should not be used as a reaction containment material. The stainless steel bottom crucible showed no signs of corrosion or failure related to the reduction reaction conditions. However, both the exterior and interior surfaces of the crucible were discolored. The empty crucible was retained for future determination as to if its discoloration is oxidation or thermal degradation of the surface areas. This discoloration may provide further indication of the exothermic nature of the reaction being studied.

Run IV was the most efficient reduction run completed to date. The reaction products contained less sodium contaminant than previously obtained. In addition, the amount of silicon product was the most obtained from a charge of sodium. It is believed that the tighter control of the sodium flow rate allowed the increased efficiency of the reaction conversion, though still only at a 50% yield. Although the stainless steel crucible contained the reaction, the interior of the crucible showed some degradation when the products were removed. It is believed that atmospheric moisture reacted with sodium oxide (Na₂O), (see equation 6) in the product mix creating a caustic solution. When this caustic solution was mixed with the sodium fluoride the solution appears to have reacted with the stainless crucible. When the reaction product was washed, a yellowish solution was produced which had not been observed before. Although subsequent washings removed the color, the iron, chromium and nickel of the stainless steel could have contaminated the silicon.



GDMS results for run IV are given in Table 6.

Table 6: GDMS Analysis of SiNaF Si from Run 4

Element	Concentration (ppmwt)
B	11
C	Matrix
N	Matrix

Element	Concentration (ppmwt)
O	Matrix
F	Matrix
Na	Matrix
Mg	8
Al	130
Si	Matrix
P	3.7
S	300
Cl	6000
K	5000
Ca	30
Ti	120
V	1.2
Cr	320
Mn	39
Fe	1000
Co	0.1
Ni	200
Cu	60
As	80
Sr	0.9

Ambient Gas Contamination of the SiF₄ and Therefore the Silicon

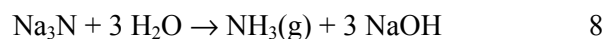
Because of the nature of the laboratory equipment used in the construction of the gas generation system, a closed system was intended but not obtained. The apparatus construction was of glassware available for general laboratory use. All glass to glass joints were standard tapered 24/40 ground joints equipped with appropriate Teflon sleeves secured with appropriate clamps. Because of safety considerations in handling the SiF₄ gas, it was decided to operate the system at a slight vacuum versus atmospheric pressure. During actual gas production and collection periods, the vacuum pressure of the system approached and topped 10 inches of mercury. This vacuum pressure apparently opened leak points within the apparatus.

Therefore, contaminants within the product matrix may have come from ambient gas contamination of the SiF₄ gas matrix. Three of the major contaminants, nitrogen (N), oxygen (O) and carbon (C) are of course found in the atmosphere.

The odor of ammonia (NH₃) was observed as being liberated during product washing. This was qualified by allowing the generated gases from the washing process to bubble through a copper sulfate solution. The solution turned from blue to green signifying the presence of amine in the copper solution. It is believed that the only way ammonia can be generated from the reaction product matrix is if sodium azide (Na₃N) was produced by reaction 7 below,



The sodium azide then reacts with the water during washing to produce the ammonia (see equation 8). The original contaminant nitrogen (N₂) could, at reaction temperatures ranging from the reaction set point of 800°C to above 1410°C, produce silicon nitride (Si₃N₄) and/or other compounds that would retain their nitrogen content and be determined during analysis.



The carbon contaminants could have been originally atmospheric carbon monoxide (CO) and/or carbon dioxide (CO₂) or could have originated in decomposition of the graphite reaction chamber.

The oxygen content of the reaction product matrix could have multiple origins. In the first two runs, x-ray diffraction (XRD) analyses identified multiple silicates present in the matrix. The large silicate or silicon oxide content of the sample(s) indicate that oxygen (O₂) was present to react with the sodium during the reduction process. The reaction run temperature was 600°C for both Runs I and II. Run III was initiated at 800°C yielding no evidence of silicate formation while elemental analysis identified oxygen as present. All four run product matrices were washed with water. For all these runs it is assumed that oxidation of the fine powdered silicon took place resulting in the formation of insoluble oxides.

Discussion of results

The gas generation system describe above using H₂SiF₆ as a raw material provided the SiF₄ gases for reduction. The problem associated with leaks in the system are inherent to the laboratory system and can not be addressed simply. However, as the gas system is enlarged approaching and including commercialization, better engineering of a sealed system will solve the leak problem.

The materials of construction problem seen with the graphite associated with the reaction location can be solved by replacing the graphite with a silicon based ceramic.

The dissolving of small sized Si by water is apparent. This reaction is aided by the addition of HF solution dissolving the SiO₂ of the water reaction process with the final product being malladrite. This problem can be addressed by raising the temperature of the product mixture to above the silicon sintering point. At that temperature, the fine silicon powder disseminated thought out the co-product sodium fluoride (NaF) will agglomerate and become larger in size thereby becoming less accessible to oxidation. Raising the temperature of the product mix above the melting points of silicon should form large pools of molten silicon in the molten sodium fluoride. When cooled, these pools should form large pieces of polycrystalline silicon within the molten sodium fluoride. After the molten sodium fluoride is drained, these larger pieces of silicon will not have to be washed with water.

A surprise in the data was the presence of calcium silicide (CaSi₂). After considering the elemental data and the XRD results, it appears that the calcium contaminant content could come from either a calcium contamination contained in the original sodium metal or from calcium contamination of the water used to wash the samples. In addition, the concentration of the calcium silicide increased as the NaF and other phases were removed from the reaction products. If the calcium is coming from the sodium, a simple filtration of the molten sodium before it enters the reduction reactor could solve the problem. DuPont currently filters their sodium during processing to remove the calcium content.

3.1.3 Future Efforts

The next step in SiNaF's efforts to commercialize the technology for the production of solar grade silicon is the production expansion to 4 to 5 kilograms of silicon per batch. A larger vacuum furnace would be modified to include a reaction chimney that would be constructed of a stainless steel outer casing and a silicon carbide lining. The length of the chimney would initially be adjustable, to determine the length of fall that will allow the reaction to go to completion before the reactants (liquid and vapor sodium) are exposed to the collection crucible. The desired result is to have the actual reduction reaction of SiF₄ with sodium take place inside the chimney. The reaction products should then fall into the crucible. The crucible in the proposed equipment is capable of collecting a reaction product mix volume complementary to 4 to 5 kgs silicon content.

An added bonus of this equipment is that this crucible can be heated under argon to above the melting point of silicon. Data, obtained earlier, showed the compatibility of the molten products of silicon and sodium fluoride with a graphite crucible to a temperature exceeding 1450°C. Thus, the temperature of sintering of the silicon metal within the molten sodium fluoride salt can be studied at temperatures below the silicon melt point. This information will provide data related to the formation of a silicon “sponge” within the molten sodium fluoride salt. If the formation of the sponge is successful, the molten sodium fluoride will be drained through a proper drain in the bottom of the crucible and collected. When successful, the melt separation of the products will eliminate the water leaching process and the problems it causes.

The silicon sponge will then be heated to above its melting point consolidating the sponge into an ingot upon cooling. A thin layer of sodium fluoride may coat the polycrystalline silicon ingots produced in the above manner. This material should be able to be removed through washing with an aqueous solution. After removal of this layer the polysilicon ingot will be broken into pieces determined usable by the PV industry.

The basic designs of the above equipment were developed with full commercialization in mind. Therefore, it is anticipated that the technology developed above will be directly cloned to larger chambers. A pilot plant capable of producing 125-kg silicon per batch will be upgraded to a continuous process where a 200 metric ton production level can be obtained. The technology of this facility will be capable of being up-sized to a 1,000 metric ton per year of solar grade silicon production plant.

3.2 Casting Optimization and Control

In this effort BP Solar was to improve control of and optimize the casting process to increase the process yield (kilograms of silicon out divided by kilograms of silicon in) by 7% and improve the material quality, such that average cell efficiency increased by 4%. This was to be achieved by improved definition of the salient casting parameters and implementation of new automated casting control systems. In addition, the Frederick casting facility is being expanded by up to a factor of five. The first phase of this expansion was completed in mid-2001. In mid-2000 a decision was made to facilitate the expansion using casting equipment purchased from an outside vendor. GTi was chosen to provide this equipment. The new stations produce 240 kg ingots from which 25 – 12.5 cm x 12.5 cm bricks can be cut. Advanced process control software is expected to provide better run-to-run repeatability relative to the heritage BP Solar station design, as well as more flexibility for advanced process development.

3.2.1 66 kg Station Development

The BP Solar 66 kg casting stations represent the evolution of a proprietary design first implemented in the early 1980's. They have operated with microprocessor controls for a number of years. These units were state of the art when first implemented, but are now obsolete. They are impossible to replace, hard to repair and do not provide sufficient memory for the additional monitoring and control we would like to add to the system. Therefore, the first step in the casting optimization was to replace these controllers with new PC based systems. A new generation, PC based controller was configured and programmed to run exactly the same process as the old controllers. During the first year of the contract, this was installed on a new group of four stations (a quad). This quad was made operational using the new PV based controller.

With the old controllers, the casting process was never fully in control, resulting in a high coefficient of variation (COV) in the downstream processes. An engineering and operations task team was assigned to identify the causes of variation and bring the area under control. The team identified several areas of concern. New work procedures were implemented, along with visual indicators of station status. These were posted on the casting stations and produced better coordination among the operators, engineers and maintenance technicians responsible for the area. The incidence of failed runs and cracked ingots fell

dramatically and remained low resulting in a stabilized coefficient of variation (COV). Overall factory COV showed a more controlled distribution and a slight improvement in the average. Average cell efficiency returned to expected levels. The team then phased out of daily control of the casting, providing revised work instructions and operator training to maintain the progress. However, this effort delayed the introduction of the new controllers onto the remaining stations.

In order to accelerate the transition, a decision was made to begin implementation of the controller upgrades using the existing program, while a software contractor developed specifications, wrote, debugged and implemented the next generation program in a parallel effort.

The first replacement controller included several new features developed under the contract. One station in the quad was equipped with a prototype automatic load/unload unit, a larger bottom heater enclosure prototype, and additional water flow and temperature instrumentation. Two more quads were then switched to the new controllers.

Software was received from the contract programmers to automate station leak testing and gas handling, and permit the saving and loading of recipes to facilitate tailoring of the run parameters for different charge types. Automatic leak detection is now operating on three quads.

An entire new quad was also added. These units incorporate many of the prototype features developed in the previous year, including mass flow controllers and vacuum gauges. The new system performs an auto-leak detect. These stations also incorporate a "second generation" version of the ingot load/unload mechanism, which was prototyped earlier. Unlike the prototype, these lift tables are controlled by the Opto22 controller rather than a dedicated small PLC. The operator interface consists of a set of illuminated push buttons. The controllers can enable/disable the buttons based on station temperature, and input from the proximity switches and through-beam receivers. Only the enabled buttons will be lit. These stations are shown in Figure 1.

The new stations are equipped with the newly designed large bottom heaters. They produce ingots with a 2 micro second cut off an average of approximately 1.2 cm lower than the older bottom heater design. In addition this design eliminates one gasketed joint from the station and employs a newly designed graphite heater element made from a very inexpensive grade of graphite.

The load unload prototype used large pneumatic cylinders to move the lift table out from under the station automatically. The production stations are moved manually with a 'T' bar mounted on the front of the station. The elimination of these cylinders makes it easier to service the station and reduces the cost significantly. All clamping of the gasketed joint between the bottom heater and the station is done with pneumatic clamps rather than bolts. This eliminates any need for operators crawling under the stations and is much safer.

Major improvements to the freeze out can were also developed on the prototype. Seven holes in the freeze out can design were eliminated to reduce the possibility of outside air entering the inert atmosphere of the station. The hole in the large steel plate, which is the bottom of the freeze out can, was increased to move the steel further away from the corners of the ingot. This improved the linear growth of the crystals near the side of the ingot and reduced the possibility of creating cracks at the corners of the ingot.

In addition, the insulation package was completely re-designed. The amount of insulation surrounding the ingot was increased to improve directional heat flow and reduce power consumption. Average electrical consumption for the heaters was reduced by approximately 1.5 KW. It is now possible to replace an entire insulation package from below the station without disassembling the station. This will greatly reduce maintenance down time.

We have also used a brick lifetime system to establish correlations between average lifetime and final cell performance (see Figure 2 below). This allows us to use the brick lifetime measurement itself as the measure of quality for the casting process. In the past, cell performance was used as the measure of quality. This greatly lengthened the feedback loop between casting and the measurement, and introduced noise from the downstream processes. Future casting optimization work will be driven by effects on the brick lifetime signature.

Figure 1
New Casting Stations



3.2.2 240 kg Station Implementation

In the second quarter of 2000, BP Solar participated in 11 casting runs using a casting station located in the GTi facility in Nashua, NH. The objectives of the exercise were: 1) to determine if the quality of HEM-cast material was at least equivalent to that cast in BP Solar-design stations, (using identical starting material) and; 2) to determine if the HEM equipment was suitable for BP Solar production use.

Quality of Cast Silicon

Material from six of the HEM runs was processed through the Frederick cell line. Data from runs #1, #2 and #4 consists of about 24,000 GTi-cast cells and about 19,000 BP Solar cast cells from matched starting material, as shown in the Table 7.

Figure 2
Efficiency and Current vs Lifetime

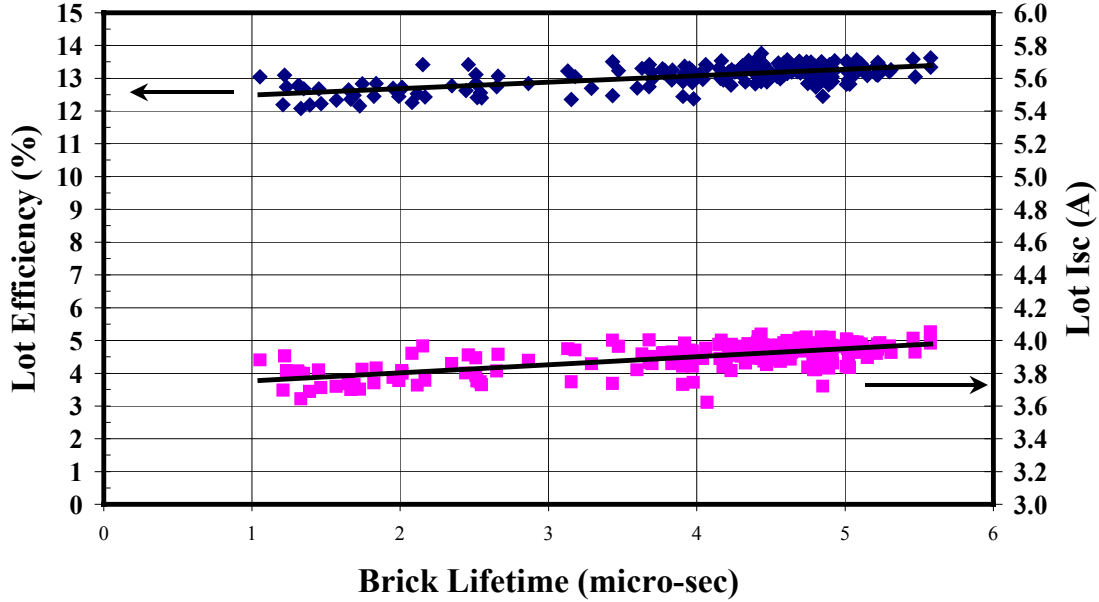


Table 7: Gti Casting Station Experimental Results

	BP Solarex Cast			GTi HEM Cast			Statistical Comparison	
	Average	StDev	COV	Average	StDev	COV	T-Test P Value	Significant (5%)?
Efficiency	12.23	0.24	1.9%	12.39	0.17	1.4%	0.044	Yes
Isc	3.70	0.05	1.4%	3.74	0.04	1.1%	0.022	Yes
FF	73.8	0.51	0.7%	73.8	0.61	0.8%	0.984	No
Voc	581.4	3.23	0.6%	582.5	2.94	0.5%	0.340	No
# Cells	19437			23921				

The GTi-cast material was statistically superior in average efficiency, with the improvement being driven primarily by short-circuit current.

Material from runs #6, #7, and #8 also produced acceptable cell results, although process issues in the Frederick line prevented a clean statistical comparison with matched starting material. Ingots from runs #3 and #5 were compromised due to issues unrelated to the overall suitability of the station. Material from later runs confirmed the initial result. Overall, we processed about 40,000 cells from material cast in the GTi-HEM station. The quality of these cells was at least equivalent to that produced using the BP Solar stations.

We also saw no fundamental issues with this station to prevent its use in production. Several issues that came up during the trial runs were addressed by the vendor. BP Solar then purchased a number of these units to populate a new casting facility that was built on the Frederick manufacturing campus starting in January 2001. The new facility is equipped to provide all the raw material preparation for both the old and the new stations as well as for the next expansion of casting capacity planned for 2001-2002. The area also includes space for sizing the large ingots into bricks, which are then moved to the sawing area in the original campus building.

The new facility was completed in June 2001 and is now operational with the GTi units. Future planned expansions will use high-capacity stations rather than the internal BP Solar design. Future process development and optimization work will be heavily concentrated on these stations.

3.3 Wire Saw Cost

In this effort BP Solar worked to reduce the center-to-center cut distance on the wire saws in production to less than 450 μm , and evaluating slurry, oil and silicon carbide recycle approaches.

3.3.1 Wafer Thickness

BP Solar Operations first completed the transition to thinner wire without changing the center-to-center spacing.

Reduction of wire guide center-to-center “pitch” was then undertaken in several, incremental steps. In each step, wire guide pitch was reduced a few microns on a single machine and the resulting wafers checked for thickness distribution and downstream yield. Then, the pitch reduction was implemented on all machines, and again the process was monitored for thickness distribution and downstream yield. Equivalent wafer thickness for etched wafers is also measured by weighing all cells processed through the automated screen print equipment in the cell line.

This approach was repeated until the wire guide pitch reached the target 450-micron spacing. We achieved the anticipated increase in saw room yield, but suffered no degradation in downstream process yields during this time. Figures 3 and 4 show the evolution of etched wafer thickness as the wire guide pitch was reduced from 475 microns to 450 microns, followed by the improvement in saw room silicon yield over the past several years. Improvements in saw yield prior to 1999 were dominated by the transition from ID saws to wire saws.

Further reductions in wafer thickness are limited not by the wire saws themselves, but by the downstream handling steps and the cell process. Experimental wire guides were purchased to cut wafers with an as-cut thickness of 150 microns. These wire guides were used to cut approximately 5000 wafers, which had an actual average thickness of about 140 microns. Cut yields were reasonable, although there were increased losses in demounting and cassetting. There appears to be no fundamental problem with current-generation wire saws cutting 150 micron wafers, and thinner wafers are also probably manufacturable with appropriate automation of the demounting step.

However, an examination of cell line yield as a function of wafer thickness shows that the present process limits wafer thickness to a minimum of 200-210 microns. Wafers thinner than this limit bow excessively during the back aluminum firing step and then cannot survive subsequent handling. This constraint means that the average etched wafer thickness must be high enough that the lower tail of the thickness distribution produces very few wafers below the 200-210 micron limit.

Further reductions in wafer thickness below an average, as-cut thickness of 250 microns were therefore not attempted.

Equivalent Etched Wafer Thickness

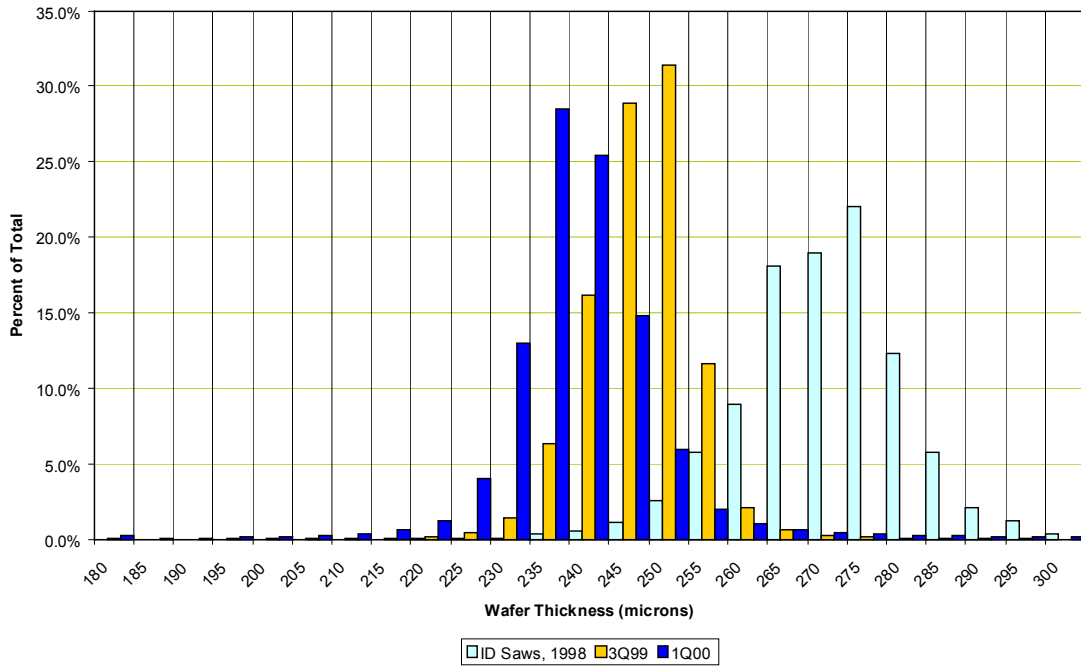


Figure 3

Sawing Yields (Sq. m Per Sized kg) Relative to 1993

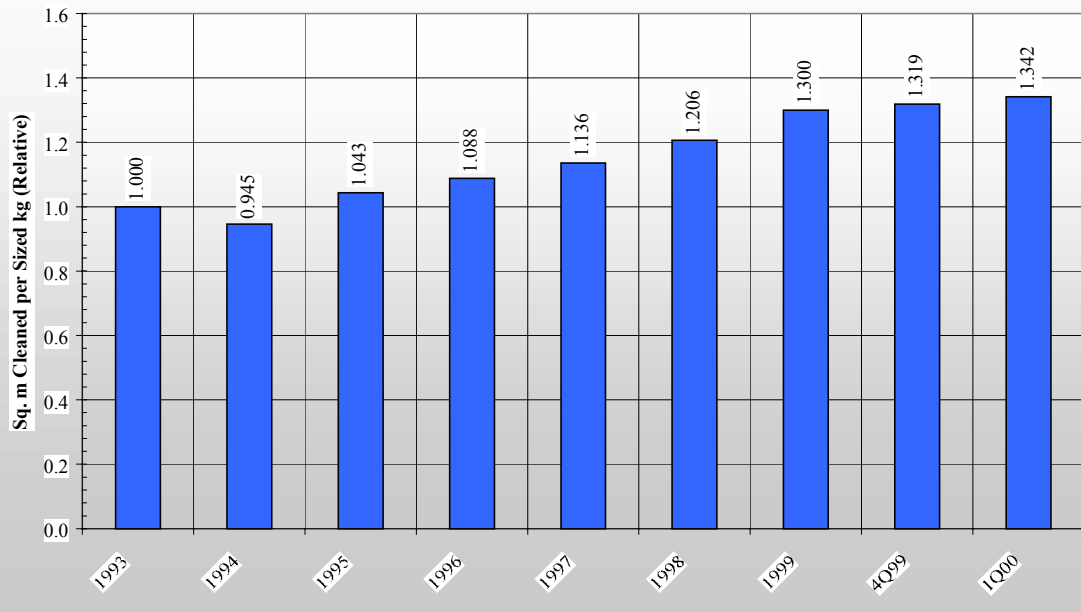


Figure 4

3.3.2 Slurry Reclaim

SiC Reclamation

BP Solar initially leased a reclamation system from GTI. It was a decanter type centrifuge system that extracts the larger particles (SiC) out of used slurry. The solids that are discharged are in a thick sludge or cake form. Fresh oil is added to this cake and is mixed to the desired specific gravity before being used again in the wire saw process.

After achieving acceptable results on the leased system, a production system was installed in 1999. The installed process uses 50% used slurry and 50% reclaimed slurry to make up each manufacturing run, thereby reducing run-to-run variation in the slurry. The GTi system ran very well for over four months, then began running with reduced efficiency because of a worn centrifuge. A new part was installed, but it was determined that the part had to be hard-coated to prevent the premature deterioration of the centrifuge. The part was then replaced with a tungsten carbide tile-coated part, which was expected to have acceptable life. This system was released to production.

A second slurry treatment unit, this one from SUI, was also installed on a single machine. This unit was designed to remove silicon fines from used slurry. The manufacturer claimed that the unit could maintain silicon levels within the slurry at 5-8% throughout a cutting run. (Silicon levels after a typical run, are ~10%). This unit underwent a single day trial. Although the processed slurry was acceptable, the operator interface to the machine was not acceptable. The machine was returned to the vendor for an automation and operator interface upgrade. The improved version of the machine completed 15 successful runs. Wafer quality remained very stable, and the TTV (total thickness variation) of the wafers did not drift over time. After fifteen runs the machine suffered a mechanical failure and was again returned to the vendor for redesign. When the system was returned it was again found to still be unacceptable for a production environment. The machine was returned to the vendor and this approach was dropped.

Oil Recovery

The SiC recovery process described above dramatically reduces the consumption of Silicon Carbide, results in an increased consumption of oil. By feeding the waste stream of the grit recovery system through a decanter centrifuge we have been able to recover clean oil. This product has been tested successfully in several wire saw runs.

The centrifuge system was been integrated with the GTi grit recovery system and run under engineering control. Further development of the system was halted because of lack of acceptance of the system by the operations group.

Glycol-based Slurries

After analyzing the cost savings possible with oil recovery and grit reclaim, this approach no longer appeared to be cost effective and was dropped in favor of oil recovery in 1999. However, environmental and factory cleanliness concerns about oil-based systems have led us to reconsider the introduction of glycol-based systems. Glycol-based coolant was introduced on a trial basis in 2000. The trial established the need for glycol-specific handling and cleaning systems as well as for glycol-specific slurry recycling and replenishment systems. New handling and cleaning stations were purchased and installed in 2001, and glycol-based slurry was reintroduced on selected saws in September 2001. Initial results have been favorable, and the glycol system may be expanded to the rest of the saw area in late 2001.

3.3.3 Wire Saw Cost Reductions

Double Table

A prototype brick mounting system was purchased from HCT. The unit allows two bricks to be mounted, side-by-side, on a wire saw, thereby dramatically increasing the throughput of the machine. After

overcoming some initial problems with control of the machine during the cut, the first trials resulted in 37% better throughput than the baseline process.

Larger trials continued to show 30%-40% better throughput on the double-table machine, and this equipment has been released to production. Several additional machines were also converted to double tables capable of running either three or four mounted bricks. Subsequent expansion of the wafering area used newer-generation machines that were already facilitated for high mounting capacity.

Wire Re-Use

A fixture was designed to allow re-spooling and subsequent second use of the wire saw wire. The fixture worked very well in engineering trials. However, operator acceptance was poor. At the same time, the double table fixture was coming into production. Wire wear in the double table process is too high to allow reuse of the wire. This approach was then dropped.

Wet Wafer Cassetting

The Wet Wafer Cassetting machine was dropped because the vendor was unable to produce an acceptable design.

Diamond Wire

Laser Tech West manufactures a diamond-impregnated wire, which has several possible applications. One is the use of this wire in the wire saw process. This would eliminate the need for slurry and has the potential for faster process times. Two different spools were tested on one wire saw. Neither run was successful. However, the wire appeared to cut well, and the problems were due almost entirely to spool and winding issues. Further tests were planned, but never carried out due to the vendor's inability to provide sufficient quantities for large-scale wire sawing.

At the same time, we investigated the use of diamond wire in the sizing process. The kerf loss in this process is currently close to 4mm per cut. A process using diamond wire would drop the kerf down to .3mm, providing large savings in silicon use and reduced waste streams. Also, the application of diamond wire to sizing would require far less wire than a wafering application and would, in general be a far less demanding application for the wire itself.

A diamond wire sizing saw was ordered in 2000 for delivery in early 2001. The saw is presently scheduled for delivery in late 2001 after considerable delay in its construction and demonstration of acceptable performance at the manufacturer's site.

3.4 Cell Process Development

In this effort BP Solar was to develop, demonstrate and implement a cost-effective, robust cell process that produces a minimum average cell efficiency of 15% and improves the cell line electrical yield. Process areas being evaluated and optimized included a new style doper, the selective emitter process, PECVD silicon nitride antireflective coating (with the assistance of North Carolina State University), and RIE (Reactive Ion Etching) texturing of polycrystalline silicon (with the assistance of Gratings, Inc.).

3.4.1 Selective Emitter

One approach to increased cell efficiency is the use of a selective emitter with a deeper junction under the metallization and a shallower junction in the emitter field. In this way the current collection in the emitter can be decoupled from the requirement of the screen-printed metallization to have a high surface concentration of phosphorus. This approach has been evaluated at BP Solar in the past using masking and etch-back techniques to produce the shallower junction in the emitter field. Efficiency gains in excess of 4% were demonstrated. However, cost analysis indicated that this process is not cost effective⁸.

Another approach to achieve a selective emitter is to use a screen printable dopant paste for the deeper diffusion under the metallization area. It was thought that this system might be cost effective, if rapid thermal processing could be used for the light emitter diffusion. For the emitter diffusion, a process was developed that matches the cell efficiency while producing 2.5 times the throughput of diffused cells in the same equipment footprint as the baseline process now in use at BP Solar.

We then looked at processes in which we would first print a commercial dopant paste in the pattern to be metallized, diffuse this area heavily, and then add a separate and lighter diffusion to the whole cell. The screen-printed metal can then be applied only in the heavily diffused area. The alignment of the metal to the heavily doped region is critical to the process. We also found that the thickness of the initial dopant print was critical to downstream processing. Thicker layers were not readily removed in the HF step typically used to clean up diffusion oxides before metallization printing.

To address this issue, we tested several new screens for their ability to print the thinnest possible dopant films. At the same time, we tested grid alignment onto a much finer pattern, designed to reduce shading losses and to thereby increase short circuit current. We achieved a 60% reduction in printed dopant paste weight, resulting in a diffusion glass that was barely visible, and easily removed by the standard HF etches. This also eliminated the need for an additional ultrasonic step.

A potential benefit of the very thin film is that it may no longer require a separate HF etch step at all prior to field diffusion. Although the problem of phosglass removal was solved, it created a secondary problem. The previously dark phosglass grid (non- HF etched wafer) was necessary for use as a setup wafer to print the grid metallization precisely over the dopant grid. With the grid now barely visible this is no longer possible. We developed a technique to overcome this problem using the Baccini printer.

Subsequently, trials were run to optimize the sheet resistivity of the field emitter, to obtain maximum current gain without losing too much fill factor. Four different profiles were used to obtain sheet resistivity ranging from 95Ω/sq to 120Ω/sq. A 30Ω/sq dopant paste grid was used for all selective emitter groups.

Best performance showed an increase in current of 1.9% relative to production controls, (see Table 8). However, the FF was down by 3%. (Also note that these cells had poor Voc due to a lack of passivating oxide.) This group incorporated a flat diffusion profile that yielded a 97Ω/square emitter. Good N-factors and shunt resistances proved that metal grid did not go beyond the finer dopant paste gridline boundaries into the much lighter field diffusion.

In an effort to improve the fill factor, three new, hotter and faster field diffusion profiles were developed. Sheet resistivities were kept near 100Ω/sq., the optimal result from previous trials.

Junction Characteristics - Spreading Resistance Analysis was performed on 9 polished FZ wafers to compare diffusion profiles for both grid and field emitters. The best grid profile with the highest surface concentration was 012599_1 – yielding a 25Ω/square grid. The results are shown in Figure 5. The best field profile from this group was 070199_4.

Cell results for these diffusions are shown in Table 9. The best current gain was 1.4% from a 86 ohm/square field. Despite the lack of a passivated surface, the cell efficiency was 1.4% greater than the control group. A passivating oxide could eliminate surface recombination losses and yield an efficiency gain of 2-3%. The use of PECVD SiN would provide even further enhancement.

Table 8

SELECTIVE EMITTER - RTC TRIAL 5
Field Emitter Varied (100 & 120ohm/sq)

	--N--	EFFIC (%)	ISC (AMPS)	VOC (mV)	FF (%)	RSER (mOHM)	RSH (OHMS)	N FACT.
--	-------	--------------	---------------	-------------	-----------	----------------	---------------	---------

Unencapsulated results, not corrected for spectral mismatch *p-values based on a 2-sided t-test w/ df adj. by F-test*

Control - Standard Production Process - BTU Diffusion (Profile 880°C @22ipm)

Group 1	--8--	12.50 (0.23)	3.776 (0.051)	586.2 (2.5)	73.4 (0.6)	9.0 (0.4)	26.1 (34.9)	1.28 (0.03)
---------	-------	-----------------	------------------	----------------	---------------	--------------	----------------	----------------

30ohm/sq GDP + 97ohm/sq Vapor Doped Field Emitter (Profile 010599_2)

Group 3	--8--	12.26 (0.30)	3.846 (0.056)	582.3 (1.8)	71.2 (0.7)	12.5 (0.8)	56.3 (99.0)	1.26 (0.04)
	Delta:	-0.23	0.070	-4.0	-2.2	3.5	30.2	-0.02
	Delta%:	-1.9%	1.9%	-0.7%	-3.0%	38.8%	115.6%	-1.4%
	p-value:	.04 *	.01 *	.00 *	.00 *	.00 *	.43	.29

30ohm/sq GDP + 104ohm/sq Vapor Doped Field Emitter (Profile 121198_3)

Group 5	--8--	11.66 (0.32)	3.808 (0.054)	582.0 (2.7)	68.4 (1.3)	16.9 (2.1)	69.4 (64.9)	1.26 (0.04)
	Delta:	-0.84	0.032	-4.2	-5.0	7.9	43.3	-0.02
	Delta%:	-6.7%	0.9%	-0.7%	-6.8%	87.7%	165.7%	-1.4%
	p-value:	.00 *	.17	.00 *	.00 *	.00 *	.11	.16

30ohm/sq GDP + 115ohm/sq Vapor Doped Field Emitter (Profile 012299_1)

Group 4	--8--	11.91 (0.23)	3.829 (0.057)	580.1 (2.2)	69.7 (0.6)	14.0 (1.1)	30.7 (25.6)	1.29 (0.04)
	Delta:	-0.59	0.053	-6.1	-3.7	5.1	4.6	0.01
	Delta%:	-4.7%	1.4%	-1.0%	-5.0%	56.3%	17.4%	0.7%
	p-value:	.00 *	.03 *	.00 *	.00 *	.00 *	.75	.50

30ohm/sq GDP + 119ohm/sq Vapor Doped Field Emitter (Profile 012299_2)

Group 6	--8--	12.03 (0.26)	3.845 (0.054)	582.2 (1.8)	69.8 (1.1)	14.7 (1.4)	37.7 (22.2)	1.25 (0.04)
	Delta:	-0.47	0.070	-4.0	-3.6	5.7	11.6	-0.03
	Delta%:	-3.8%	1.8%	-0.7%	-4.8%	63.5%	44.4%	-2.6%
	p-value:	.00 *	.01 *	.00 *	.00 *	.00 *	.40	.02 *

NO PASSIVATING OXIDE ON SELECTIVE EMITTER GROUPS
CELLS PROCESSED WITH FULL-FIELD BSF BACKS
47 LINE SCREENS - (GDP 1.5Fx1.1B)
30ohm/sq PROFILE (081898_2)

Figure 5

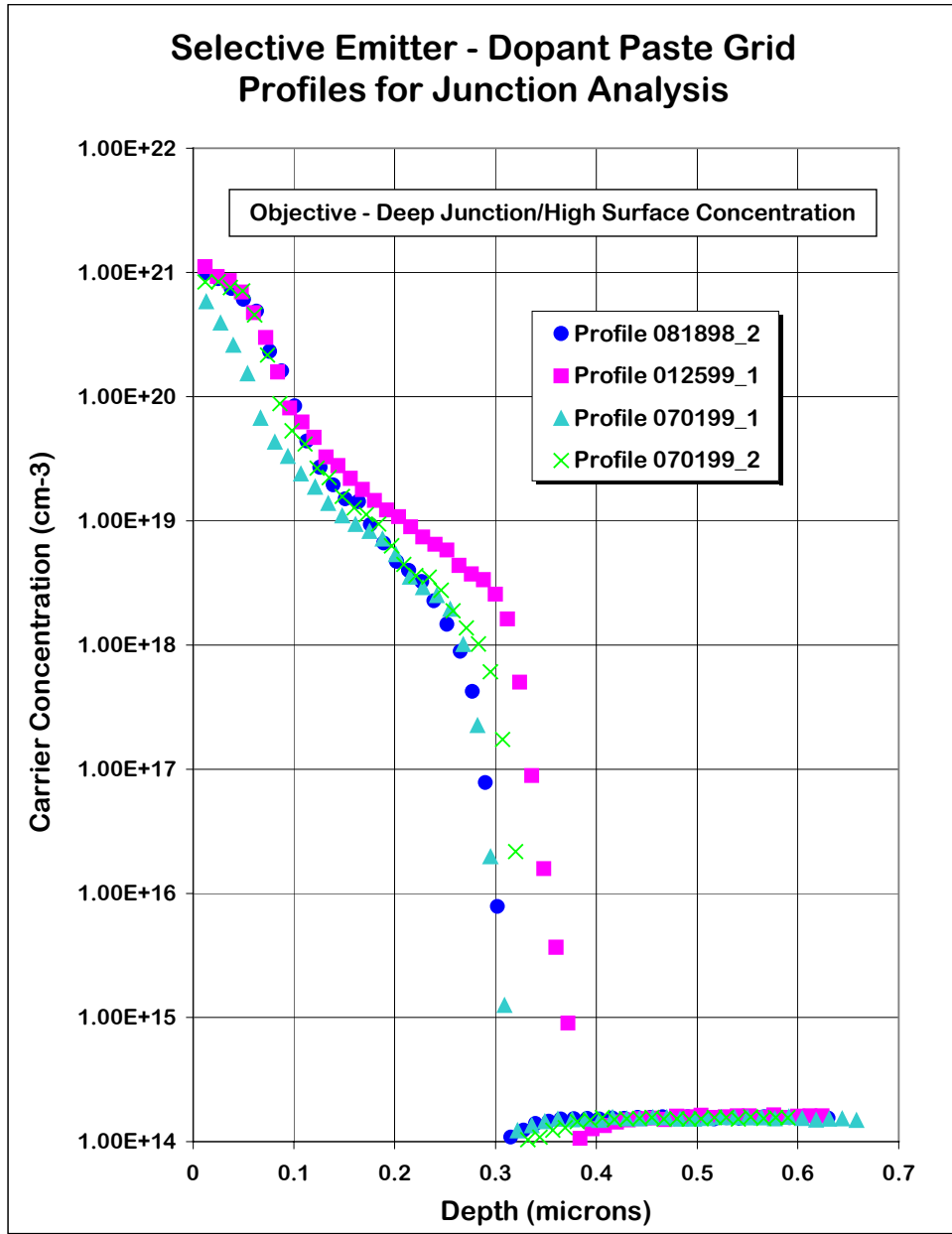


Table 9

RTC - SELECTIVE EMITTER - TRIAL 6

Optimizing Field - Increasing Temperature

--N--	EFFIC (%)	ISC (AMPS)	VOC (mV)	FF (%)	RSER (mOHM)	RSH (OHMS)	N FACT.
-------	--------------	---------------	-------------	-----------	----------------	---------------	---------

Unencapsulated results, not corrected for spectral mismatch

p-values based on a 2-sided t-test w/ df adj. by F-test

RTC Control - 44ohm/sq - Vapor Doped - Profile 070698_8								
Profile -->	910	910	910	910	890	880	860	14ipm
Group 5	--6--	12.95 (0.11)	3.880 (0.023)	589.8 (1.8)	73.5 (0.2)	9.4 (0.5)	8.8 (2.1)	1.18 (0.01)

30ohm/sq GDP + 86ohm/sq VD Field - Profile 010599_2								
Profile -->	860	860	860	860	860	860	860	20
Group 1	--6--	12.12 (0.28)	3.936 (0.011)	577.2 (4.1)	69.4 (1.2)	12.0 (0.8)	10.3 (2.8)	1.36 (0.11)
	Delta:	-0.83	0.056	-12.6	-4.2	2.6	1.5	0.18
	Delta%:	-6.4%	1.4%	-2.1%	-5.7%	28.0%	16.6%	15.5%
	p-value:	.00 *	.00 *	.00 *	.00 *	.00 *	.33	.01 *

30ohm/sq GDP + 92ohm/sq VD Field - Profile 070199_3								
Profile -->	900	900	900	900	900	900	900	70
Group 2	--6--	10.85 (0.72)	3.857 (0.025)	557.9 (12.6)	65.5 (3.1)	10.3 (1.3)	8.5 (3.0)	1.83 (0.39)
	Delta:	-2.10	-0.023	-31.8	-8.0	0.9	-0.4	0.65
	Delta%:	-16.2%	-0.6%	-5.4%	-10.9%	9.7%	-4.0%	55.5%
	p-value:	.00 *	.12	.00 *	.00 *	.17	.82	.01 *

30ohm/sq GDP + 91ohm/sq VD Field - Profile 070199_4								
Profile -->	920	920	920	910	890	880	860	75
Group 3	--6--	10.91 (0.60)	3.847 (0.022)	558.8 (10.4)	66.0 (2.6)	10.3 (1.3)	8.3 (5.4)	1.76 (0.34)
	Delta:	-2.03	-0.033	-31.0	-7.6	0.9	-0.5	0.58
	Delta%:	-15.7%	-0.9%	-5.3%	-10.3%	9.9%	-6.1%	49.4%
	p-value:	.00 *	.03 *	.00 *	.00 *	.15	.83	.01 *

30ohm/sq GDP + 92ohm/sq VD Field - Profile 070199_5								
Profile -->	950	925	900	890	880	870	860	70
Group 4	--6--	10.95 (0.75)	3.857 (0.021)	557.6 (13.4)	66.1 (3.0)	10.1 (1.2)	11.4 (3.4)	1.81 (0.38)
	Delta:	-2.00	-0.023	-32.2	-7.4	0.6	2.5	0.63
	Delta%:	-15.5%	-0.6%	-5.5%	-10.1%	6.9%	28.7%	53.5%
	p-value:	.00 *	.10	.00 *	.00 *	.25	.15	.01 *

30ohm/sq Profile (081898_2)

After a review of overall project priorities, work on selective emitter was put on hold. This process, by itself will not be cost effective. Selective emitter designs may be cost effective as part of a high efficiency cell process sequence, but not as a stand-alone addition to an existing process.

3.4.2 PECVD Silicon Nitride

PECVD application of Silicon Nitride (SiN) is a critical component of high efficiency cell processing. The process enhances cell efficiency by providing both an anti-reflection coating and hydrogen passivation of the silicon substrate. Initial contract efforts focused on demonstrating the desired efficiency gain, and then on making a set of high-efficiency modules for environmental qualification testing. The cells were diffused at BP Solar and the SiN deposition and the fire through process were completed at IMEC. Average encapsulated cell efficiency for the SiN modules was 14.6%. These modules passed IEC 61215 qualification tests.

The next step toward production implementation was to evaluate potential high-throughput equipment. A number of trials were completed with SiN deposited by Shimadzu using their equipment, and completed by BP Solar or IMEC. Up to 14.5% average cell efficiency was achieved on small initial trials.

In a subsequent, larger-scale trial, efficiencies over 15% were achieved using wafers diffused at BP Solar and SiN deposited at Shimadzu, (See Table 10). The metallization was at BP Solar using standard equipment.

Table 10

Shimadzu SiN CVD fire through Trial -3

9-Jun-99

	--N--	EFFIC (%)	ISC (AMPS)	VOC (mV)	FF (%)	RSER (mOHM)	RSH (OHMS)	N FACT.
		15.27	4.352	609.6	74.8	9.1	26.2	1.13
Group 1	--7--	(0.09)	(0.022)	(1.0)	(0.5)	(0.6)	(8.9)	(0.02)
		15.31	4.370	609.8	74.7	9.2	17.1	1.13
Group 2	--7--	(0.09)	(0.015)	(0.6)	(0.3)	(0.4)	(6.0)	(0.02)
	Delta:	0.04	0.018	0.2	-0.2	0.1	-9.1	0.00
	Delta%:	0.3%	0.4%	0.0%	-0.2%	0.6%	-34.7%	-0.1%
	p-value:	.43	.10	.59	.52	.86	.04 *	.90

To evaluate the potential gain of the new process compared to the existing one, an experiment was run to compare the standard cell line process, with BSF and TiO₂ AR coating, to a fire-through process with SiN AR. Both groups went through the BSF process in the production cell line. The SiN fire-through process averaged 7.2 % efficiency improvement over the controls. The spectral response data confirmed the improvement in collection efficiency with the SiN fire through process. A repetition of this experiment produced a 6.8% gain for the SiN fire-through process.

We also investigated a SiN fire-through process on single-crystal substrates, achieving a 16.3% average cell efficiency on 125 mm CZ. The cell efficiency under encapsulation will be about 16.5%. These

efficiencies are comparable to those achieved by the Saturn process (laser-grooved, buried contact process) on similar substrate.

At this point, a detailed cost analysis of the proposed process was prepared, and a technical evaluation was completed for internal management review. Cost and equipment uptime issues with the Shimadzu equipment led us to investigate other potential vendors for the deposition equipment. We decided to focus on the Centrotherm tube furnace as a potentially cost-effective addition to a BP Solar factory. The tube furnace was found to have higher uptime and lower capital cost per unit output than the in-line equipment used previously.

A 7% improvement in the performance, relative to the baseline process, was demonstrated on wafers with SiN deposited at Centrotherm using the sequential fire through process. A system was then purchased and installed at the Tata BP facility in Bangalore, India during the fourth quarter of 2000. The system is now in full production. Cells produced in the Bangalore facility have averaged 14.1% on multi-crystalline wafers. The Bangalore cell line is configured as a “flex” facility, capable of making both multi-crystalline and mono-crystalline cells.

3.4.3 New Doper Process

Application of phosphorous dopant at BP Solar has been done using a patented process in which hot phosphoric acid mist is deposited on the wafer surface just before they enter the diffusion furnace⁹. This process, while very cost effective, has been relatively difficult to maintain because the hot acid is hard on the process equipment. A new, proprietary design was built, using a cool vapor source instead of the traditional heated quartz tube. The reduced temperature relaxes several design constraints on materials used in construction of the doper.

A prototype unit was constructed and used in the process lab to demonstrate performance equivalent to the older method. The lab unit was then used in over a month of extensive, production trials and was found to have greater reliability than the older units. Production equipment was ordered and installed in late 2000 and early 2001 in both the Frederick facility and in the BP Solar facility in Sydney, Australia.

These units have been very well received by the operations staff. Reduction of wear parts has resulted in savings over \$20,000 per year per machine, and diffusion uptime has increased by more than 5% while overall process variability is equivalent to that obtained with the older systems.

3.4.4 Fast-cure Silver Ink and Rotary Print

BP Solar worked with several vendors to identify a fast-cure, back silver paste formulation. The baseline process was to print a back silver contact ink, to dry that ink, and to then print the aluminum BSF ink and co-fire the whole back contact system. This process requires a number of handling steps. The desired process would perform both print steps on a single, rotary table printer. The silver would be printed, as usual, then dried in-situ as the printer rotated. The aluminum would then be printed and the two inks co-fired.

Two candidate paste formulations completed environmental qualification. One of the two candidates passed the test sequence and was selected for implementation. A rotary printer was ordered and initial engineering trials demonstrated equivalent electrical performance to that of the production line. The equipment cycle time was initially slightly below what was anticipated, but this was resolved with modest mechanical and software modifications.

Control of the heated nest plates was initially poor. The heater design and its associated control system were completely retooled and subsequent trials produced satisfactory rates and electrical performance.

The process was transferred to operations in Frederick. It has been very well accepted by operations and its performance has exceeded expectations for rate and uptime. Because of the reduction in handling achieved by having both back prints done on the same printer, line yield has increased and overall process variation has been reduced.

3.4.5 RIE Texturing of Polycrystalline Silicon

The performance of commercial polycrystalline Si solar cells still lags behind crystalline Si due in part to the inability to texture poly affordably and effectively. Surface texturing of polycrystalline Si has been an active field of research. Several techniques including anodic etching¹⁰, wet acidic etching¹¹, lithographic patterning¹², and mechanical texturing¹³ have been investigated with varying degrees of success. To date, a cost-effective technique has not emerged.

In recent years, RIE (random reactive ion etching), texturing techniques have received significant attention^{14,15,16}. Random RIE texturing techniques take advantage of the extensive infrastructure developed for Si microelectronics applications, and as such can lead to significant savings in costly tool development efforts for the PV manufacturers. As worldwide PV demands increase, the use of thinner ($\leq 100 \mu\text{m}$) Si substrates is expected to increase substantially. In this context, RIE texturing techniques are critically important not only for their proven ability to reduce broadband spectral reflection ($\sim 1\%$ for $\lambda < 1 \mu\text{m}$), but also their ability to enhance oblique coupling of incident light into the semiconductor substrate. For a weakly absorptive medium such as Si in the near IR spectral range, statistical analysis by Yablonovitch has shown that optical absorption with a lambertian surface can be enhanced by $\sim 4n^2$ relative to a planar surface, where n is the refractive index¹⁷. In order to reach this statistical limit, typical texture dimensions have to be comparable, or larger than the optical wavelengths of interest. If texture dimensions are smaller than the optical wavelengths, scattering is not effective due to the inability to resolve the texture. Figure 6 demonstrates this interdependence between texture dimension and light interaction in terms of enhanced coupling into obliquely propagating diffractive modes.

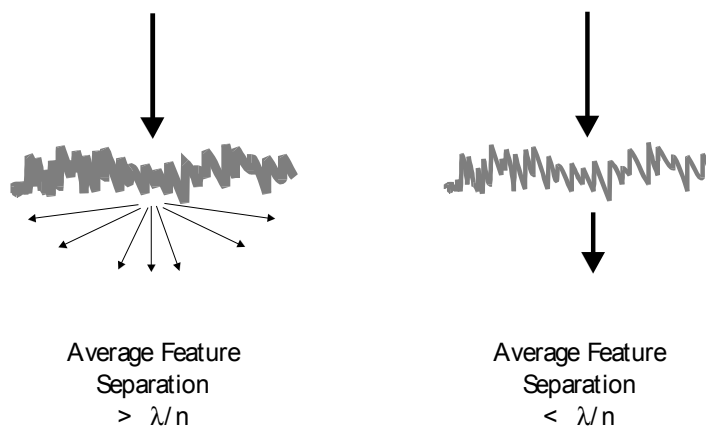


Figure 6: Optical scattering from features comparable, or larger (left) and smaller (right) than the incident optical wavelength.

Gratings, Inc. in collaboration with Sandia National Laboratories has developed large area ($\sim 187 \text{ cm}^2$), maskless random RIE texturing techniques^{18,19}. These techniques use a metal-catalyst approach to tune microstructure profile and dimensions aimed at profiles beneficial for the solar cell performance. Figure 7 shows three types of profiles achieved using these methods. Comparison of feature dimensions shows that

Cr-assisted etching produces the smallest ($\sim 0.3 \mu\text{m}$) average separation. Aluminum and conditioned texture average separations are typically an order of magnitude larger with columnar and triangular profiles. The hemispherical spectral reflectance measurements from several metal-catalyst RIE-texturing processes are shown in Fig. 8. It can be seen that typical reflectances are similar despite significant differences in microstructures. For comparison, reflectance measurements from alkaline etched and polished Si surface are also shown.

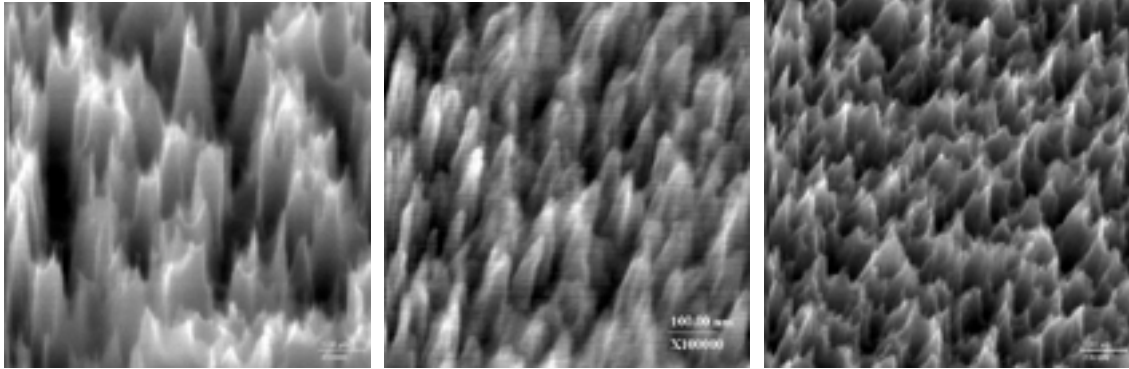


Figure 7: SEM pictures of three random RIE texture profiles, Al-assisted (left), Cr-assisted (center), and conditioned (right). SEM length scales are $1\text{-}\mu\text{m}$ for Al and conditioned, and $0.1\text{-}\mu\text{m}$ for Cr.

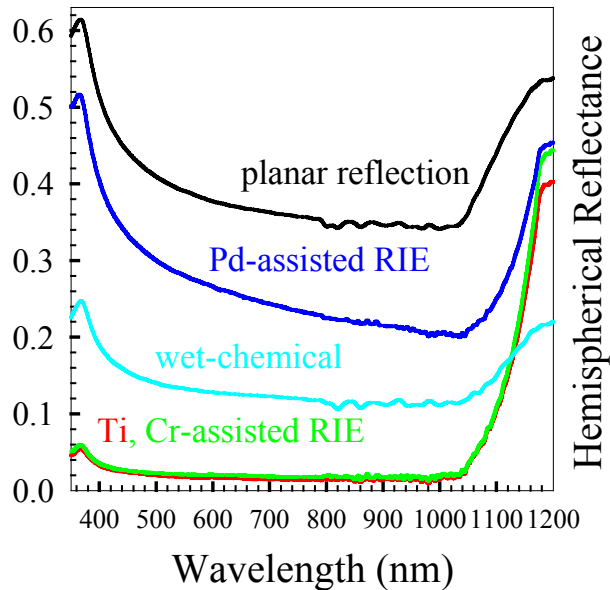


Figure 8: Absolute hemispherical spectral reflectance measurements for several textured surfaces without anti-reflection coatings.

Initial solar cell fabrication on RIE-textured surfaces revealed that the benefits of lower reflection did not result in improved solar cell performance due to several contributing factors including contamination,

RIE-induced surface damage, and the lack of optimum emitter formation. By incorporating a complete RCA clean process followed by nitric acid wet-chemical damage removal (DRE) treatment, solar cell performance comparable to wet-chemically etched c-Si cells was achieved^{18,19}.

BP Solar subcontracted with Gratings, Inc. to evaluate random RIE-texturing of its polycrystalline material for cost-effective enhancement of solar cell performance. BP Solar provided Gratings with wafers for RIE texturing. Gratings performed the texturing and sent the wafers back to BP Solar to complete the solar cells processing. Several textures and nitric acid DRE treatments were evaluated. Figure 9 shows cell efficiency and J_{SC} measurements from Cr-assisted, Al-assisted, and conditioned texture processes. The RIE-textured wafers used here were not subjected to either RCA clean, or nitric DRE treatments. For these texturing conditions, there is no significant performance enhancement relative to the planar control wafers. Figure 10 shows results of similar texturing experiments in which a complete RCA clean was employed following random RIE texturing. Comparison of Figures 9 & 10 shows similar behavior for all three textures indicating that the inclusion of RCA clean does not lead to major performance enhancements.

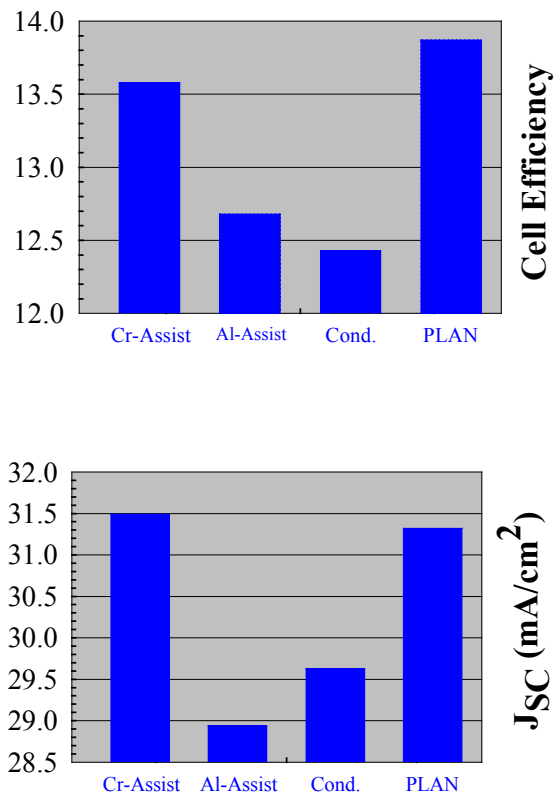


Figure 9: Efficiency (above) and J_{SC} (below) measurements on RIE textured cells of 130-cm² area. No RCA cleaning process was employed following RIE texturing.

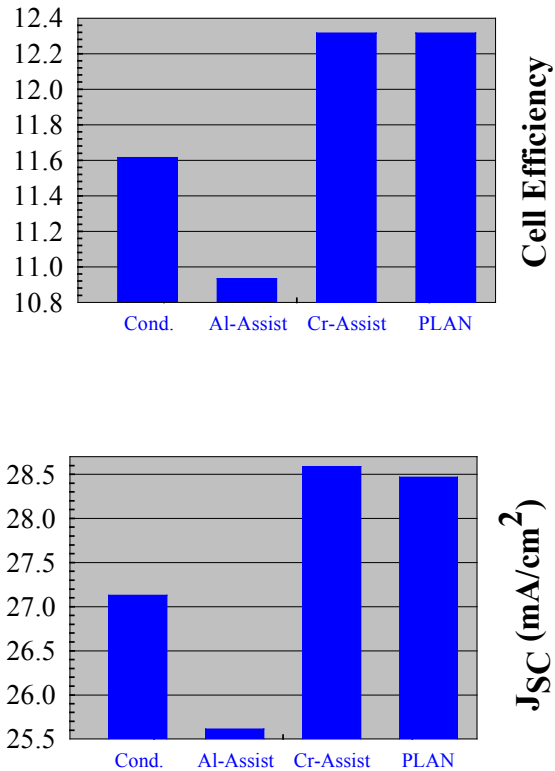


Figure 10: Efficiency (above) and J_{SC} (below) measurements on RIE textured cells of 130-cm² area. Wafers were subjected to complete RCA clean following the RIE texturing processes.

In Gratings earlier work with crystalline Si, similar lack of performance enhancement was observed. By etching surface damage layers using nitric acid, superior performance relative to planar controls was achieved. This nitric DRE treatment was also applied to BP Solar material. Figure 11 shows a comparison of conditioned textured solar cells fabricated with and without nitric DRE treatments. The cell efficiency and J_{SC} measurements are from solar cells on 130-cm² areas. For the conditioned texture process, the nitric DRE treated textured cell performance is significantly improved relative to the untreated textured surface, and slightly improved relative to the planar controls.

The lack of performance enhancement despite substantial reduction in surface reflection can be understood by looking at the internal quantum efficiency measurements. Figure 12 shows the internal quantum efficiency (IQE) and hemispherical spectral reflectance measurements from the RIE-textured cells with and without nitric DRE treatments. It can be seen that despite low reflectance (~ 3.7 SWR), J_{SC} enhancement is not observed due to substantial IQE loss in most of the visible region. By subjecting as-fabricated RIE-textured surfaces to nitric DRE treatment, the surface reflection is substantially increased due to the removal of fine texture, however, J_{SC} is increased probably due to enhanced contribution in the near IR region. This enhanced near IR response is due to oblique optical coupling caused by diffractive scattering.

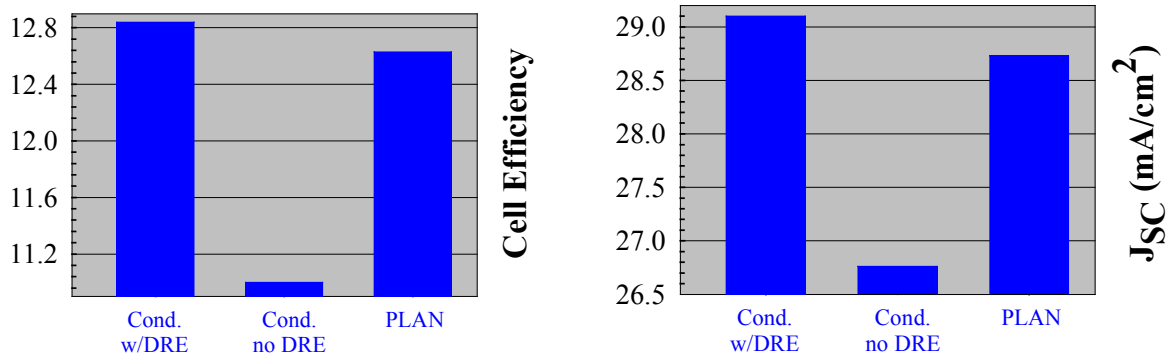


Figure 11: Efficiency (left) and J_{SC} (right) measurements on RIE textured cells of 130-cm² area. Wafers were subjected to complete RCA clean and nitric DRE treatment following the conditioned texturing processes.

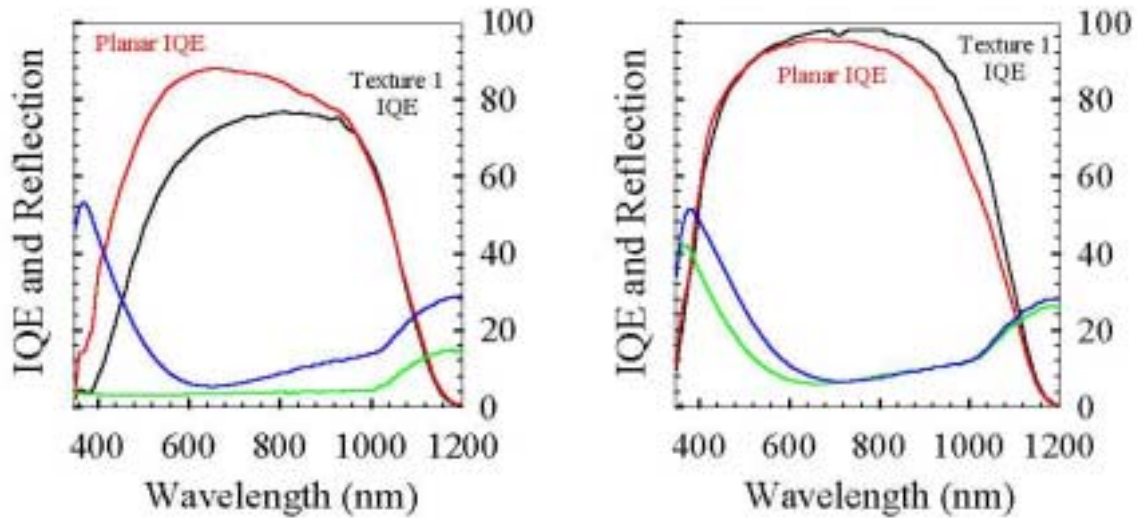


Figure 12: Internal quantum efficiency and hemispherical reflectance measurements from the RIE-textured cells without nitric DRE (left) and with nitric DRE (right) etch treatments.

Georgia Tech fabricated 4-cm² solar cells on BP Solar polycrystalline Si RIE texture etched at Gratings. The results presented here are averaged from 9 cell measurements. PECVD silicon nitride anti-reflection coatings and back surface fields were incorporated in the cell processing. Cell results from evaporated and screen-printed contacts were virtually identical. Figure 13 shows cell efficiency measurements from as-textured surfaces and from the nitric DRE-treated surfaces. Without the nitric DRE treatment, most textured cells have lower efficiency than the planar controls. Incorporation of the nitric DRE treatment, results in all textured surfaces outperforming planar control cells, with the best performance coming from the conditioned and Al-assisted texturing processes. The corresponding short-circuit current measurements for the two cases are shown in Fig. 14, and are consistent with the efficiency measurements. The 14.1 % efficiency and 33.2 mA/cm² short-circuit current for conditioned texture process with nitric DRE are the highest values observed on BP Solar material.

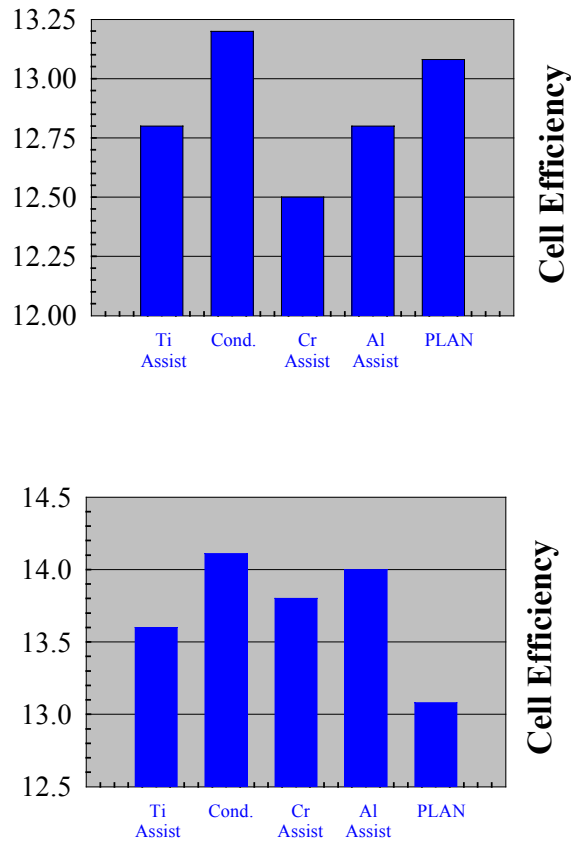


Figure 13: Efficiency measurements from 4-cm² area solar cells fabricated at Georgia Tech from BP Solar material. Measurements above are from the textured surfaces without DRE and below from the textured surfaces subjected to nitric DRE treatments.

In all cases, and for all cell areas, random RIE-texturing techniques have helped enhance solar cell performance relative to the planar controls. It is also clear that optimum cell processing for RIE-textured surfaces has not yet been developed. All the cell processing parameters applied here were developed for large (\gg optical wavelengths) surface features.

Random RIE-texturing techniques should be capable of delivering far superior performance enhancements than measured so far. Several technical issues such as optimum emitter formation and removal of surface damage need to be resolved. In order for RIE-texturing techniques to find industrial applications, the following issues have to be addressed.

- Random RIE-texturing techniques in their present form are slow (\sim 5-10 minutes), although large area cells (\sim 200 cm²) can be textured using commercially available tools. In some cases, the texture does not extend to the cell edge, leaving \sim 0.5 to 1cm wide region relatively planar. Gratings is addressing these concerns, and plans to extend its present capability both in terms of throughput and uniformity over the entire wafer.
- To date, only isotropic nitric acid etching has been investigated in detail. Due to lack of precise etch control, this may not be the best option for removing surface damage. Gratings has

investigated plasma-less XeF₂ and wet-chemical NaOH solutions. Both of these techniques are widely used in industry, and may offer more precise control and lower cost.

- Solar cell results from various laboratories demonstrate varying degrees of performance enhancements. One key to achieving maximum benefits from these RIE-textured surfaces lies in the formation of an optimum emitter. These types of surface may require non-conventional emitter formation techniques.

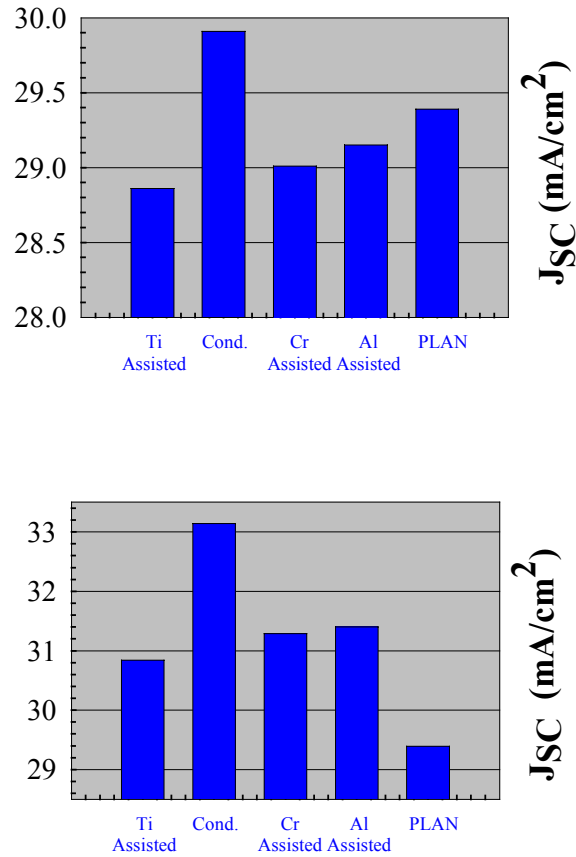


Figure 14: Short-circuit current measurements from 4-cm² area solar cells fabricated at Georgia Tech from BP Solar material. Measurements above are from the textured surfaces without DRE and below from the textured surfaces subjected to nitric DRE treatments.

In summary, random RIE-texturing techniques combined with plasma-doping methods may provide an optimum, cost-effective alternative for cell processing that is compatible with the large area, large volume wafer processing requirements of PV manufacturing.

3.4.6 Silicon Nitride AR Coating – Understanding the mechanism for improved performance

In recent years it has been shown that a post deposition anneal of silicon nitride anti-reflective (AR) layers on crystalline silicon solar cells can lead to an increase in cell efficiency^{20,21,22}. Measurements have shown that the improvement in cell performance is due to an increase in the internal quantum efficiency (IQE) of the cell and is therefore due to an improvement of the electronic properties of the bulk material.

The IQE data indicate that the anneal causes either passivation of the bulk recombination statesⁱⁱⁱ or a reduction of the surface state density^{23,24}. While the bulk passivation process could be explained by a saturation of crystal defect states through hydrogen that diffused from the coating into the bulk silicon, the surface density state reduction could be explained by the formation of a thin oxide layer during the anneal.

To determine which mechanism is responsible for the improvements of the solar cells, BP Solar subcontracted to the Physics Department at North Carolina State University (Dr. Gerald Lucovsky). The first step in their study was to determine the diffusion behavior of hydrogen between crystalline silicon and silicon nitride. The possibility of hydrogen diffusion from the heavily hydrogenated silicon nitride AR-layer into the underlying bulk Si is strongly dependent on the hydrogen density at the interface between the Si and the coating layer. Only when a sufficiently high H-concentration at this interface can be maintained during the anneal, will a permeation and subsequent diffusion of hydrogen take place into the bulk. A knowledge of the microscopic transport mechanisms of hydrogen in silicon nitride is therefore of crucial importance for the investigation of the anneal process.

In these experiments the silicon nitride films were deposited by remote plasma enhanced chemical vapor deposition (RPECVD) using silane (SiH₄) and Ammonia (NH₃) as reactants. In some experiments deuterium was used in place of the hydrogen in some regions of the deposited film. Polished single crystal silicon wafers were used as substrates since multicrystalline wafers are more textured and inhomogeneous and so are not compatible with the measurement techniques employed.

Measurement techniques utilized were:

1. Fourier Transform Infrared Spectroscopy (FTIR) to measure the types and density of chemical bonds found in the films.
2. Ellipsometry to measure the film thickness and dielectric constant.
3. Secondary Ion Mass Spectroscopy (SIMS) to determine the depth profile of hydrogen, deuterium and oxygen in the films and the silicon substrates.

Whether the hydrogen is released from the silicon nitride into the bulk silicon or only into the environment during the anneal depends largely on the transport mechanism that is dominant within the silicon nitride material. A “slow” H diffusion, with a low diffusion constant, caused by a high activation energy (2.95 ± 0.15 eV), has been reported in low pressure chemical vapor deposited (LPCVD) silicon nitride²⁵. The proposed mechanism is an atomic diffusion of H atoms that jump between covalent NH bonds. Hydrogen can also migrate through silicon nitride while it is attached to small molecules like H₂, ammonia or silane. Such molecules can only diffuse interstitially through the network and therefore have small activation energies, which means high diffusivities at high temperatures. However, unlike atomic H diffusion, this process requires a preceding chemical reaction, during which the small molecule dissociates from the network²⁶. Since these dissociation energies and the activation energy of the atomic diffusion process have the same order of magnitude (eV) the overall H bond density in a given film is reduced for both mechanisms in a similar way, making it difficult to distinguish the two effects. However, the permeation of H into the silicon substrate depends on the H density at the interface. The type of H transport mechanism in the silicon nitride is of critical importance.

While the two different diffusion mechanisms do not lead to significantly different net H content reduction, the depth profiles in the two cases can vary significantly. In either case the diffusion can be described by the diffusion equation. However, the term for creation and annihilation of the diffusing particles vanishes for the case of atomic H diffusion, but is important for molecular diffusion. This difference plus the different diffusion constants of the H atoms and molecules lead to a different density depth profile for the two mechanisms. The atomic H diffusion can sustain a relatively high concentration near the Si substrate even when most of the H near the coating surface has already moved into the

environment. However, the reduction of the H density during dissociation processes is homogeneous throughout the film since any density gradient is instantly compensated because of the high diffusivity. Therefore, for molecular diffusion the density becomes equal to the reaction rate, which is assumed to be homogeneous in the film since the film has a homogeneous chemical structure.

An experiment was designed to determine whether the H transport in silicon nitride is by atomic or molecular processes. A stack system was deposited onto a polished single crystal wafer. The stack (See Figure 15) consisted of a thin layer of silicon dioxide, a 400Å layer of deuterated silicon nitride ($\text{Si}_x\text{N}_y\text{D}_z$) and a 400Å layer of hydrogenated silicon nitride ($\text{Si}_x\text{N}_y\text{H}_z$). Variables included use of three different oxide thicknesses (4Å, 10Å, and 20Å) and five different anneal temperatures between 500°C and 900°C. Deuterium in the lower half of the silicon nitride layer works as a labeled substance whose chemical behavior is similar to hydrogen, but nevertheless is distinguishable from H using FTIR. By designing the stack system's geometry so that only negligible amounts of deuterium can diffuse out of the system, one can account for the measured changes of ND and SiD bond densities. They are entirely due to D diffusion into the Si bulk. The hydrogenated silicon nitride layer at the surface acts as a diffusion barrier for the D atoms by absorbing deuterium from the layer underneath without causing any changes in the FTIR spectra. Moreover, since the hydrogen in the top layer does not have a buffer zone, a heavy loss of H out of the system can take place, eventually leading to differences between the area concentrations of D and H.

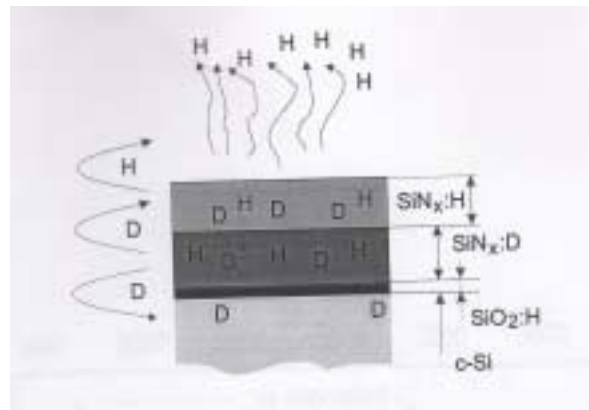


Figure 15: Stack system for the diffusion experiment.

Figure 16 shows the development of the FTIR absorbance peaks for the sample with the 10Å silicon dioxide layer. The bond density is plotted versus inverse absolute temperature in Figure 17. The values of the initial concentrations were within their error range at about $6.5 \times 10^{16} \text{cm}^{-2}$, which confirmed the expected thicknesses of about 400Å for each silicon nitride layer. In addition, within the range of error, both D and H layers initially have about the same content. The loss of both D and H bonds increases with increasing temperature.

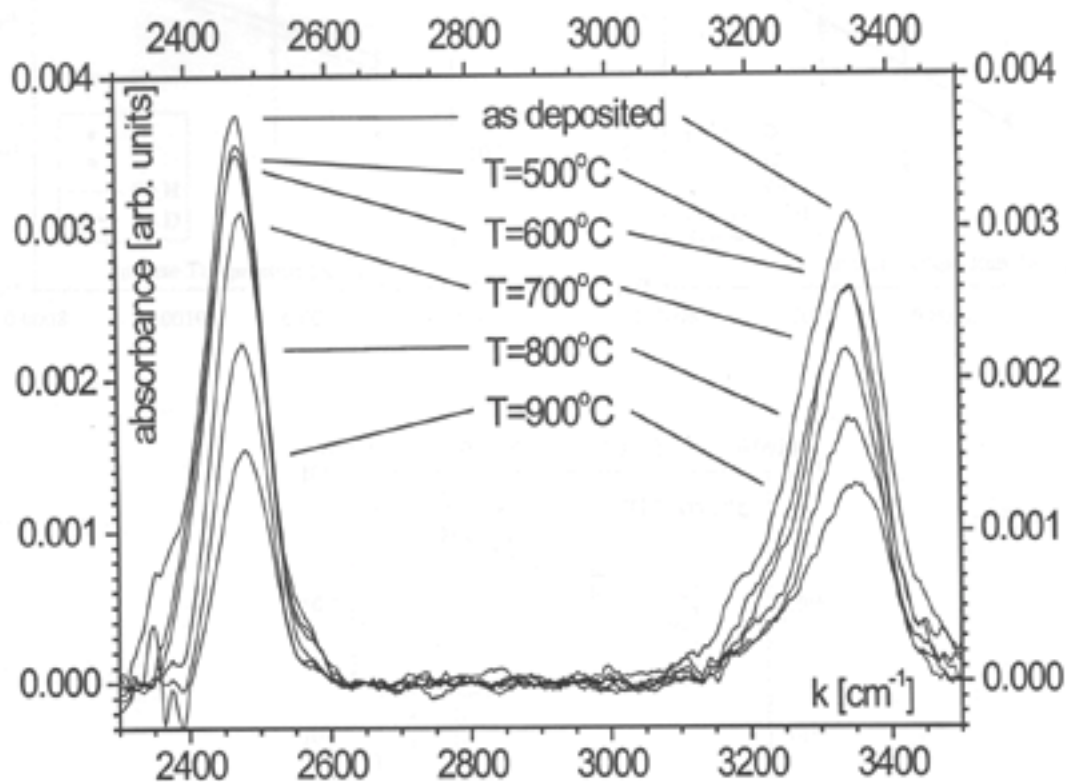


Figure 16: The ND and NH FTIR peaks for the 10Å samples.

The most interesting result of this diffusion experiment is that the magnitude of the post anneal densities of H and D are in all cases equal within their error ranges. This observation strongly supports the dissociation model. The results for different oxide thicknesses at equal temperatures are also equal within their error ranges. Different oxide thicknesses were used in order to detect a possible H or D diffusion into the Si which could be indicated through higher D/H densities in samples with thinner SiO₂ barriers. However, this higher density was expected only for the case of slow D diffusion. Both the equivalent H and D levels and the independence from oxide thickness suggests that there is no significant H permeation from the nitride into the silicon and also strongly indicates that the dissociation mechanism is dominant.

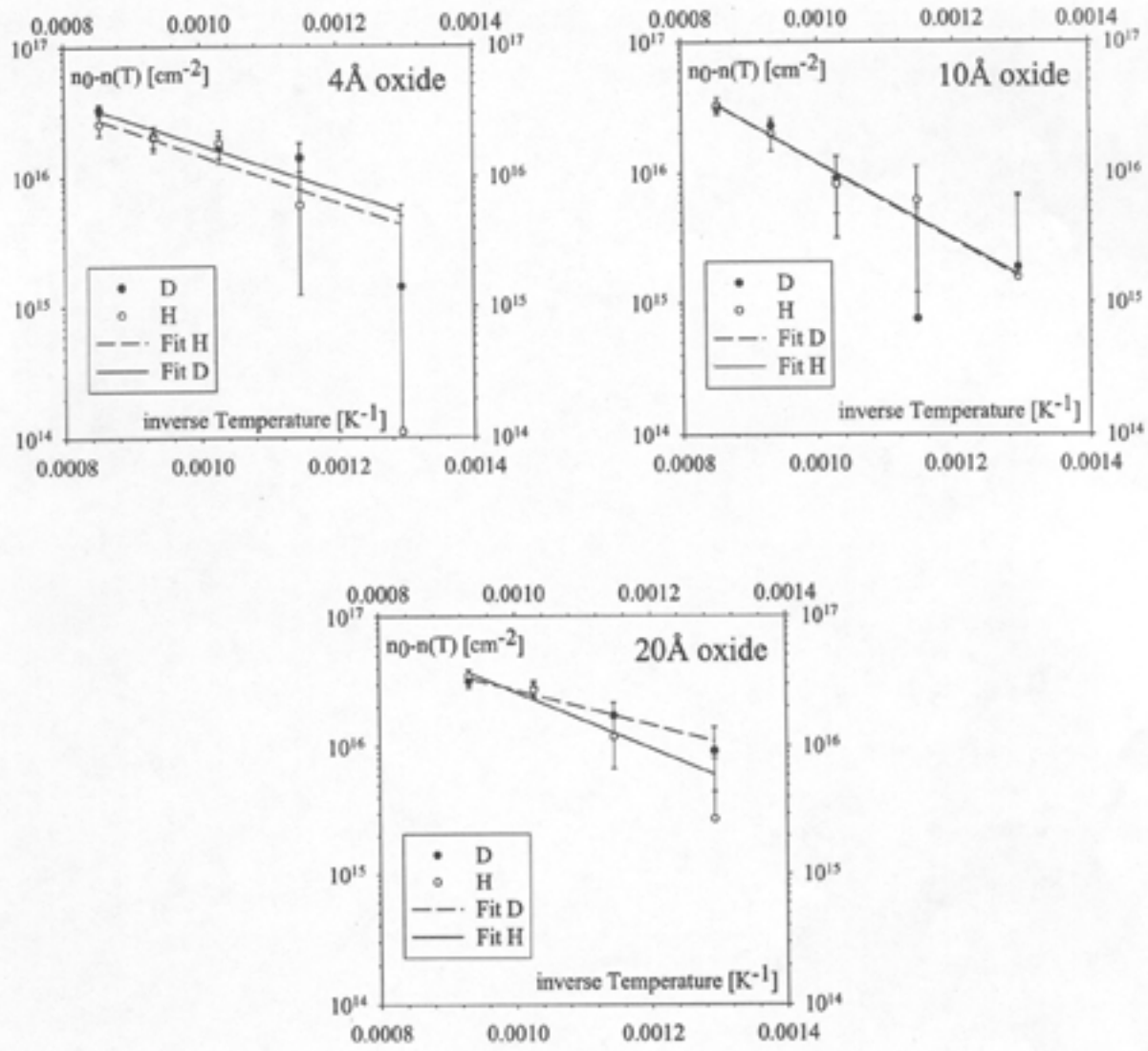


Figure 17: D and H bond density inverse temperature dependence

The results of the SIMS analysis for the stack experiment confirmed the FTIR observations. The profiles of D, H and O for the sample with 10Å oxide annealed at 900°C are shown in Figure 18. The oxide has peaks at the surface and the Si/SiN interface with minima in the SiN and in the Si. Note that the interface oxide peak has grown substantially wider, from 10Å to 150Å, presumably due to oxygen diffusion from the interface layer into the nitride and silicon, as well as some broadening due to the finite depth resolution of the SIMS process.

In spite of completely different initial distributions, both curves have almost identical shapes and are almost constant throughout the silicon nitride region. Such a shape and the order of magnitude reduction from the unannealed sample supports the conclusion that the fast diffusion molecular process dominates

the diffusion. Both H and D show a rapid decrease in concentration across the oxide region. Within 5 to 10 nm of the Si surface both H and D concentrations reduce by two orders of magnitude. In the bulk silicon the H level drops below the detection limit for H ($8 \times 10^{18} \text{ cm}^{-3}$) so no statement can be made about the H profile below that limit. The D density remains above its detection limit of $8 \times 10^{17} \text{ cm}^{-3}$ within the top 200 nm of the silicon bulk. However, the size and shape of the D density profile is likely caused by SIMS artifacts – D atoms that were sputtered from the crater edge with high D content into the silicon crater with low D content during the measurement. Therefore a significant movement of deuterium from the silicon nitride into the crystalline silicon can not be confirmed.

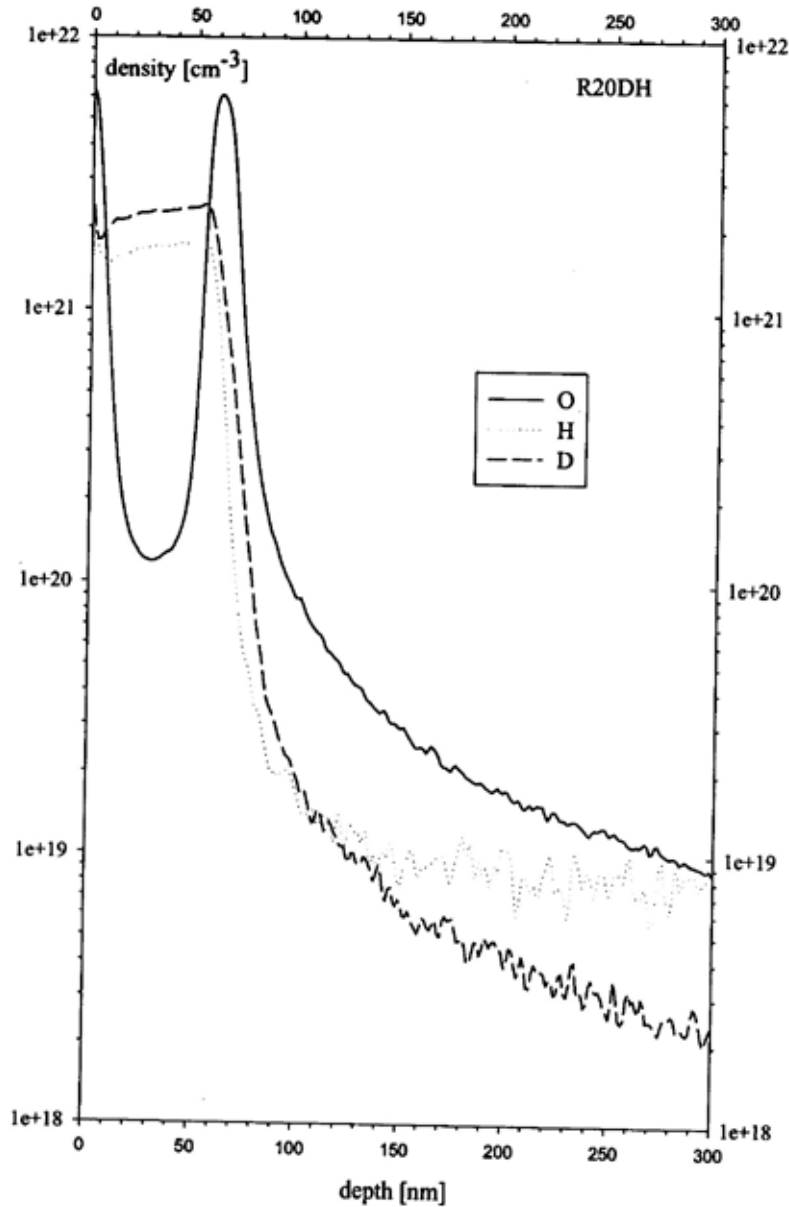


Figure 18: SIMS profile of the diffusion stack system after 900°C anneal.

NCSU conducted a second set of experiments and analysis to get a better understanding of the chemical reactions that lead to the dissociation products that are responsible for the rapid diffusion of hydrogen in silicon nitride. Since the dissociation of small molecules was anticipated, processes involving molecular hydrogen (H_2), ammonia (NH_3), hydrazine (N_2H_4), single NH and NH_2 groups, as well as silane (SiH_4), and disilane (Si_2H_6) were all evaluated. Some of the processes evaluated are shown in Table 11. The reaction enthalpies were used as one criteria for the likelihood of possible reaction because exothermic processes are far more likely than endothermic ones. Based on these considerations only 2 likely reactions were identified in Table 11.

Table 11: Chemical reactions involving $Si_xN_yH_z$ likely in silicon nitride.

E (eV) Reduc bond	Reaction	E (eV) Prod bond	ΔE (eV)	Likelihood
7.78	$2N-H \Delta H_2 + N-N$	6.23	1.55	Unlikely for low T since $\Delta E > 0$
6.34	$2Si-H \Delta H_2 + Si-Si$	6.83	-0.49	Unlikely since $n_{Si-H} \ll$
7.06	$Si-H + N-H \Delta H_2 + Si-N$	8.92	-1.86	Likely as long as Si-H bonds are present
12.68	$4Si-H \Delta SiH_4$	13.20	-0.52	Unlikely since $n_{Si-H} \ll$
22.19	$7Si-H \Delta Si_2H_6 + NH$	25.79	-3.6	Unlikely since $n_{Si-H} \ll$
12.2	$Si-N + 2N-H \Delta NH + Si-H$	7.06	5.14	Unlikely since $\Delta E > 0$
23.87	$Si-N + 5N-H \Delta 2NH_2 + Si-H$	19.11	4.76	Unlikely since $\Delta E > 0$
23.87	$5N-H + Si-N \Delta Si-H + N_2H_4$	21.01	2.86	Unlikely since $\Delta E > 0$
11.67	$Si_2N-H + 2N-H \Delta 2Si-N + NH_3$	12.10	-0.43	Likely as long as N-H bonds are present

A set of 216 samples were then fabricated using 3 different ammonia to silane ratios, two isotopes (H,D), six anneal times and six anneal temperatures. Bond densities in the films were measured using FTIR. The resultant data was compared to the results expected for the two likely reactions identified in Table 11. The data at 500°C and below fit that expected for the reaction $Si-H + N-H \Delta H_2 + Si-N$. The data for higher temperatures fit the reaction $Si_2N-H + 2N-H \Delta 2Si-N + NH_3$.

The North Carolina State University work can be summarized as follows:

- Slow atomic diffusion of hydrogen does not play a significant role for the loss of hydrogen and hydrogen bonds from silicon nitride. Fast diffusion of molecules that dissociate from the covalent silicon nitride network is much more significant.
- At 500°C only a small fraction of the NH bonds react with an equally small number of SiH bonds to produce molecular hydrogen, which leaves the system. At higher temperatures this process still takes place, but is swamped by other reactions that cause stronger H loss.
- Between 600°C and 900°C, the reaction of three NH bonds into ammonia becomes dominant and leads to exponentially increasing H loss with increasing temperature. The reaction rate decreases with increasing temperature since the reducing NH density in the film reduces the interaction probability.
- While this ammonia producing process is taking place there is not likely to be much hydrogen diffusion into the crystalline silicon.
- Beyond 900°C, the development of molecular hydrogen out of two NH bonds prevails and increases the reaction rate while lowering the bond density even further.
- Oxygen at the crystalline silicon/silicon nitride interface can diffuse slowly away from its location, but maintains a high enough concentration at its original location to produce interface passivation.

While these results would argue that there is no hydrogen passivation of crystalline silicon from the silicon nitride annealing process, these results were obtained on single crystal silicon, and therefore do not preclude grain boundary diffusion of hydrogen in some polycrystalline materials. In addition, these experiments were not performed on diffused wafers, so the results on solar cells may be impacted by the interaction of the hydrogen species with both the diffused phosphorus and the defect damage caused by the phosphorus diffusion. Some combination of surface passivation and diffusion damage passivation may explain the efficiency improvements obtained when using PECVD silicon nitride on single crystal silicon cells.

3.5 Faster Cure Encapsulant

In this effort BP Solar was to develop and qualify, through a lower-tier subcontract with Specialized Technology Resources, Inc., formerly Springborn Testing and Research (STR), an encapsulation system that meets technical and reliability requirements and can be laminated and cured in less than 6 minutes in the present BP Solar laminators.

Throughout this development effort, the industry's desire for a 30-year lifetime encapsulant has been considered an integral part of the requirements. Capitalizing on STR's prior experience in developing UV stabilized, non-discoloring EVA-based encapsulants, every effort was made to select formulation constituents that were felt to have negligible effect on the encapsulant's long-term UV stability²⁷. This effort is described in section 3.5.1 – Faster Curing Encapsulation System.

In addition to faster-curing requirements, the degradation effects caused by moisture upon aging of PV modules has recently become a PV industry focus, especially with regard to thin film technologies. Therefore, some effort was expended to examine the feasibility of modifying EVA to decrease the PV encapsulant's moisture vapor transmission rate (MVTR), thereby possibly rendering a PV module more hydrophobic. This effort is described in section 3.5.2 –Moisture Vapor Transmission Rate.

At the request of BP Solar, a portion of STR's development effort was directed towards the development of a flame retardant encapsulant system for utilization in standard crystalline silicon PV modules. An improved flammability resistance achieving a minimum UL 1703 Class B flammability rating was targeted. This is a pioneering effort, as there are no known flame retardant encapsulant systems capable of passing the flammability test requirements and appropriate for PV solar cell encapsulation. This effort is described in section 3.5.3 – Flame Retardant EVA.

During the course of this effort, it has become clear that the faster the lamination process, the more important it is to be able to evaluate the results of the lamination process quickly. Today the process is controlled by assuring that the modules reach a certain temperature for a specified time. Periodic qualification tests are performed to assure that the process remains in control. In case of expected problems, Gel tests are used to measure the cross-link density. These tests take a long time to perform and don't provide the quick feedback necessary in a production environment. An effort to develop rapid turn-around cure monitoring is described in section 3.5.4 – Cure Monitoring.

3.5.1 Faster Curing Encapsulation System

STR's efforts were initiated with an extensive literature search. Noteworthy information gathered included:

- A pertinent Japanese patent JP 93041577, entitled "High transparency laminates production by laminating sheets with thermosetting resin composition containing EVA copolymer and organic peroxide, heat-curing and UV irradiating," was awarded to Bridgestone Tire KK.
- BMC Solar in Germany is using Dyneron THV200 in its premium roof modules. Dyneron THV200 is a fluoroterpolymer that is substantially more expensive than the EVA-based

encapsulants. When its properties were compared to PhotoCap™ 15295, it was found to offer no significant advantages over EVA-based encapsulants other than its inherent flammability resistance.

- Surlyn™ resins (ionomers) were identified as potential PV encapsulant material. A review of DuPont's literature discloses that free and bound methacrylic acid is contained within the ionomer resins. The presence of the acid requires melt processing using stainless steel tooling. A further concern is the ionomer's high rate of moisture absorption, which necessitates long drying cycles prior to processing. These factors, combined with pricing at approximately two times that of EVA, eliminated the ionomers from serious consideration.
- Encapsulant systems based on ethylene butyl and methyl acrylates were also identified.
- Liquid encapsulants were eliminated as being too cost prohibitive, difficult to handle and required long curing times.

Resulting from the literature review and dialog with industry experts, it was concluded that the rate of encapsulant cure might be accelerated by multiple means. Higher lamination temperatures would dramatically reduce the curative's half-life, thereby reducing the time required to achieve an acceptable level of crosslinking. The employment of acetic acid scavengers and/or peroxide co-agents could lead to faster curing of EVA-based encapsulants at current or higher processing temperatures. Formulation of the encapsulant with a more active peroxide that has a shorter half-life versus the present 00-t-Butyl 0-(2-Ethylhexyl) Monoperoxy carbonate (TBEC) curative could speed the process. It was also postulated that the encapsulant's curative system could be formulated to be responsive to UV through incorporation of a UV Photo-activator, that on pre-treatment with UV, may reduce the curative initiation temperature. Aztec Peroxides Inc., claims that reaction between UV Photo-activator and the TBEC has been reported.

A conceived approach to reducing the encapsulant system's overall cost is to replace the encapsulant layer behind the solar cells with a less expensive material that does not have the critical optical clarity requirements as does the top encapsulant layer. Some of the concerns in doing so are lack of adhesion between the encapsulant layers and to the backsheet, and mismatches of thermal expansion and rigidity that could cause serious deformation.

Preliminary Materials Qualification

As a result of the literature search, a number of polymeric candidates were selected for consideration as candidate base resins for the faster curing encapsulant system. For screening purposes they were evaluated versus STR 15295P EVA-based encapsulant system. Those considered include: a number of EVAs ranging from 10-32% vinyl acetate supplied by 4 different suppliers; a series of ethylene butylacrylate copolymers ranging from 7-35% butyl acrylate; ethylene methyl acrylate copolymers ranging from 10-30% methyl acrylate; and, ethylene octene copolymers ranging from 20-28% octene.

Compression molded plaques were prepared for each material. Each 18 mil thick sample was then evaluated for its average percent light transmission characteristics over the wavelengths of 360 – 900 nanometers. It was noted that by compression molding of the Elvax 3185, PhotoCap™ 15295P and A9918P specimens, the measured light transmission values were actually ~3% lower than measured values for extruded specimens (probably due to surface phenomena induced in the compression molding process). Therefore, the expected light transmission values were extrapolated for the extruded specimens.

In conclusion, DuPont's 32% vinyl acetate containing EVA was found to offer the most advantage in optical properties (percent light transmission over the wavelengths of 360 – 900 nm) and is generally less expensive than other alternatives identified. The evaluation results are presented in Table 12.

Table 12:
Candidate Encapsulant Resin Percent Light Transmission Values

Commercial Name	Generic Description	% T (Measured) Molded Specimens	% T Extruded Specimens
PhotoCap™ 15295P	Fast Cure EVA	90%	93.5% ⁽¹⁾
PhotoCap™ A9918P	Standard Cure EVA	91%	94% ⁽¹⁾
Elvax 3185	EVA - 32% VA	90%	93% ⁽¹⁾
Elvax 265	EVA - 28% VA	88%	91% ⁽²⁾
Escorene LD-781.36	EVA - 33% VA	90%	93% ⁽²⁾
Escorene LD-755.36	EVA - 29% VA	90%	93% ⁽²⁾
Escorene LD-723.62	EVA - 19% VA	82%	85% ⁽²⁾
Escorene LD-706.62	EVA - 15% VA	80%	83% ⁽²⁾
Escorene LD-409.09	EVA - 10% VA	76%	79% ⁽²⁾
Ateva 2825	EVA - 28% VA	86%	89% ⁽²⁾
Ateva 1841	EVA - 18% VA	80%	83% ⁽²⁾
Ateva 1645	EVA - 16% VA	79%	82% ⁽²⁾
Evatane 33-45	EVA - 33% VA	84%	87% ⁽²⁾
Lotryl 35BA40	EBA - 35% BA	87%	90% ⁽²⁾
Lotryl 30BA02	EBA - 30% BA	86%	89% ⁽²⁾
Lotryl 28BA175	EBA - 28% BA	80%	83% ⁽²⁾
Lotryl 17BA04	EBA - 17% BA	74%	77% ⁽²⁾
Lotryl 7BA01	EBA - 7% BA	70%	73% ⁽²⁾
Lotryl 35MA05	EMA - 35% MA	87%	90% ⁽²⁾
Lotryl 24MA07	EMA - 24% MA	84%	87% ⁽²⁾
Engage 8180	Ethylene Octene 28%	84%	87% ⁽²⁾
Engage 8400	Ethylene Octene 24%	80%	83% ⁽²⁾
Engage 8411	Ethylene Octene 20%	78%	81% ⁽²⁾
Vamac E90448-28A	EMA - 31% MA	84%	87% ⁽²⁾
Chevron 6335	Ethylene Butene	72%	75% ⁽²⁾
Elite 5200	Polyethylene	68%	71% ⁽²⁾
Equistar NA345-013	Polyethylene	64%	67% ⁽²⁾
Equistar NA214-000	Polyethylene	65%	68% ⁽²⁾
(1) – As measured			
(2) – Extrapolated			

Based upon these measured results, it appears that only the highest VA content EVAs have the desired level of optical transparency for front sheet encapsulant applications. Of the other ethylene copolymers evaluated, only those of the highest copolymer contents were determined to have average light transmissions ranging from 89-91%, all of which are more costly than the EVA copolymers.

As part of the qualification of alternative lower cost encapsulants for deployment behind the solar cells, a preliminary study was undertaken. It was noted that polyethylenes of all types gave poor adhesion to 32% VA type EVA. In some cases a mismatch of linear coefficient of thermal expansion was noted, that resulted in wrinkling of the laminate. Based upon preliminary investigations, the EVA copolymers having approximately 10% vinyl acetate content appear most viable in terms of cost, coefficient of thermal expansion, and toughness.

A Qualitative Cure Test

To reduce the time necessary to qualify the achieved cure level, a simple qualitative test was conceived and proven. This test method consists of suspending cured EVA strips with a weight (approximately 3

times the encapsulant weight) in an oven at 95°C with a standard distance marked between two points (A & B). The weighted strips are oven exposed for a minimum of 10 minutes. Cured EVA strips maintained their original measured distance between points A & B. Those uncured demonstrate elongation caused by melting or softening of the EVA. Correlation between the qualitative oven test and the quantitative gel test indicates that a minimum cure level of 70% has been achieved when the sample passes the 95°C/10-min. oven test.

Feasibility Study To Achieve a Faster Curing Encapsulant

A series of additives were evaluated to determine their effects on acceleration of cure of the EVA-based encapsulants. Unfortunately, only modest gains in curing rates resulted. The single parameter that has the greatest effect on the EVA-based encapsulants' cure is temperature. TBEC peroxide is reported as having a half-life of 3.8 minutes at 150°C. At 171°C the half-life is less than 30 seconds (approximately an 8-fold increase in rate). However, prior industry experience suggests that higher lamination temperatures are unfeasible as bubble formation occurs in the EVA during lamination at temperatures approaching 155°C. At 171°C the situation only worsens.

Consulting previously published reports on the EVA encapsulant development, in 1986 JPL reported the IR analysis of the thermal effluents from EVA encapsulants²⁸. That analysis concluded that water evolves at 105°C, carbon dioxide at 120°C, acetone and t-butanol at 177°C and acetic acid at 205°C. It was further determined that at least 1.5 wt. % water can be present in a 33% vinyl acetate containing EVA following short exposure to air.

Based on that information, a series of experiments was pursued to determine what affect drying has on bubble formation during lamination. The experiments were conducted on EVA as normally packaged, partially dried and completely dried. The completely dried specimens were exposed to vacuum for 18 hours at 50°C. The partially dried 18-mil samples were vacuum dried for 1-2 hours at 50°C. Some additional samples received partial drying through storage in a desiccator at room temperature overnight. The non-dried specimens had at least one week's exposure to ambient air.

Lamination was accomplished using a compression molding press in the presence of atmospheric air. The following results were noted:

- No bubbles formed during lamination of the dried EVA encapsulants in the absence of vacuum.
- All of the partially dried EVA samples produced bubbles.
- All of the non-dried EVA encapsulants evidenced bubbling as expected.
- Additional samples of the previously dried encapsulants were exposed to ambient air for a week, and then laminated without vacuum. Bubbles resulted.

These results suggest that formulation ingredients may not be the only contributor to bubble formation; moisture may also play a role.

Dimethyl phthalate (DMP) was evaluated in conjunction with EVA to determine if it would inhibit bubble formation. By simply coating DMP onto the 15295P EVA formulation, qualitatively it appeared to reduce bubble formation. (The DMP functions by forming an azeotrope, 98% water / 2% DMP.)

Based upon speculation that moisture may contribute to bubble formation during lamination, an investigation into the amount of time EVA remains sufficiently dry to avoid bubble generation during lamination was pursued. Bubbles were noted following 66 hours exposure to ambient air, while none were noted after 48 hours. Based on these results, a series of experiments were conducted to verify that drying the EVA-based 15295 encapsulant prior to lamination would provide an advantage in reduced

bubble formation at high lamination temperatures. Unfortunately, the findings in the vacuum laminator did not correlate well with the findings performed in the hot presses. In the vacuum laminator experiments, regardless of the drying, bubble formation occurred as the EVA-based encapsulant temperature exceeded 155°C.

A series of EVA resin (based upon DuPont’s Elvax 3185) and EVA-based encapsulant samples were submitted to DuPont to ascertain the moisture content of the 32% EVA resin as received by STR prior to processing, versus the moisture content of STR’s fully formulated 15295P encapsulant. DuPont conducted its determinations in accordance with ASTM D-789, performing Karl Fischer titrations.

In addition to the DuPont moisture content determinations, STR determined the 32% EVA resin’s total volatile content under isothermal conditions at 155°C for 15 minutes under nitrogen, by Thermal Gravimetric Analysis. The moisture content and percent volatiles data are presented in Table 13.

Table 13:
Percent Moisture and Volatile Content of EVA Resin and EVA-Based Encapsulant

Item	Sample Description	Karl Fischer Titration Water, PPM (wt.%)	Thermal Gravimetric Analysis Volatiles PPM (wt.%)
1	32% EVA resin, from unopened container	288 (0.0288)	340 (0.03399)
2	32% EVA resin, 3 days in open air	286 (0.0286)	-
3	32% EVA resin, dried 24 hrs. under vacuum	-	351 (0.03510)
4	32% EVA resin, dried 3 days under vacuum	-	194 (0.01939)
5	15295P encapsulant, freshly manufactured	65 (0.0065)	-
6	15295P encapsulant, 3 days in open air	78 (0.0078)	-

Contrary to an earlier hypothesis, minimal moisture was measured within the EVA-based 15295P encapsulant, suggesting that the volatiles evolving as bubbles in the encapsulant near 155°C are probably linked to the formulation’s constituents.

Based upon the moisture content determinations carried out by DuPont through Karl Fischer analysis and STR’s TGA, the maximum measured water content of the uncured EVA encapsulant is less than 0.06%. On that basis, it’s speculated that nearly all of the volatiles emitted from the EVA during vacuum lamination likely evolve from the curative. As the half-life of TBEC peroxide at 163°C is less than one minute, approximately 80% of the peroxide should be decomposed in 2.5 minutes at 163°C.

Similar experiments were carried out using a candidate alternative “hotter” curative that has a shorter half-life than TBEC peroxide. Similar results were obtained with this curative at 154°C, versus the 163°C TBEC experiments.

Formulation Modifications

Ensuing laboratory efforts identified an experimental formulation that required a lamination cycle of seven minutes to pass the qualitative cure test. The encapsulant configuration was composed of 2 different EVA formulations. The superstrate EVA portion consisted of a modified version of the PhotoCap™ 15295 formulation, containing one additional ingredient. The substrate EVA formulation was also based on the 15295 formulation, though a 10% EVA copolymer was substituted for the 32% EVA. Both EVA-based encapsulants were dried prior to lamination.

During lamination temperature fluctuations were observed. These may be attributed to the curative’s exotherm (increasing dramatically with temperature) and the evolution of volatiles that actually cools the EVA in the laminator. The endothermic effect accelerates with increased platen temperature. Increased vacuum dramatically increases the rate of volatilization. However, the source of volatiles apparently

becomes depleted in time as the rate of volatilization decreases with time. There appears to be intense volatilization under vacuum between 145°C and 155°C. It may be possible to avoid bubble entrapment by eliminating the vacuum as the EVA's temperature begins approaching 155°C.

Processing Variables Using TBEC Peroxide vs. An Alternative Curative

STR's fast-curing 15295 and 15295P EVA-based encapsulants employ TBEC peroxide as their curative. Lamination tests at atmospheric pressure indicated that cure could be accomplished in 3.5 minutes total at 170°C, however, with substantial bubble formation. Based upon half-life determinations and experimentation, this corresponds to a 6-minute cure at approximately 160°C. Similarly, based upon kinetic predictions, an alternative curative was evaluated with expectations of behaving similarly using a 6-minute lamination cycle at 152°C. A number of variables were examined for their effect on lamination using both curative systems in the EVA-based encapsulant.

- For both curative systems, the initial vacuum should be applied as quickly as possible.
- Experiments were conducted to evaluate how quickly it was necessary to transition from vacuum to atmospheric pressure in the lower chamber. The top chamber was pressurized to one atmosphere over a 5-second interval. The lower chamber was also pressurized over the next 10 seconds. Adequate flow of the encapsulants was realized.
- Other experiments were conducted employing molecular sieves as a scavenger for volatiles. The sieves were formulated into the back layer of the EVA-based encapsulant. These experiments proceeded poorly as the sieves were difficult to disperse and actually nucleated bubble formation.
- Experimental efforts conducted using vacuum dried EVA versus EVA exposed to air for over two days, qualitatively suggested faster curing advantages during the lamination process.
- Experiments conducted with varying surface textured EVA suggest that the textured encapsulant surfaces aid in the evacuation of air from the laminate versus non-textured encapsulants.
- Experimentation with multiple temperature ramping and processing versus a single platen temperature indicated no advantage over the single platen temperature.

Based upon the above experimental results, the best lamination process was the utilization of a single platen temperature that is dependent upon the curative employed (160°C for the TBEC peroxide curative and 152°C for the alternative curative).

Faster-Curing Lamination Trials of Experimental Formulations

A series of lamination trials were conducted based upon three formulations: the first being the PhotoCap™ 15295P formulation, the second a modified version of 15295P containing an alternative curative substituted for the TBEC peroxide, and the third X15303P, an enhanced UV stabilized "Fast-Cure" EVA formulation developed under STR's PVMaT 3A contract. Two sets of lamination parameters were utilized:

1. Complete processing was accomplished using a laboratory vacuum laminator in a total 6-minute cycle. The laminator was maintained at constant temperature for the entire lamination sequence. Air evacuation was accomplished by pulling vacuum on both top and bottom chambers. Subsequently, pressure was immediately applied, requiring 5 seconds to return to atmospheric pressure in the top chamber. Immediately following pressing of the laminate, the bottom chamber was also returned to atmospheric pressure over a 5-second interval. The laminate remained in the laminator for a total time of 6 minutes. Platen temperature was maintained at 163°C for the 15295P and X15303P. The modified 15295P with alternative curative was processed at 154°C.
2. Processing was accomplished in two stages. The first stage involved a four-minute vacuum lamination cycle, followed by a 3-minute oven post cure cycle. As in (1) above, the laminator was

maintained at constant temperature for the entire lamination sequence. Air evacuation was accomplished by pulling vacuum on both top and bottom chambers. Subsequently, pressure was immediately applied, requiring 5 seconds to return to atmospheric pressure in the top chamber. Immediately following pressing of the laminate, the bottom chamber was also returned to atmospheric pressure over a 5-second interval. The laminate remained in the laminator for a total time of 4 minutes. The laminates were removed immediately and placed in an air-circulating oven that was maintained at the laminator's platen temperature and held for three minutes. The platen and oven temperatures were maintained at 163°C for the 15295P and X15303P. The modified 15295P with alternative curative was processed at 154°C.

The results are presented in Table 14.

Table 14:
Results of "Faster-Curing" Lamination Trials

Encapsulant System	Sample No.	Total Time	Process	Laminate Composition ¹	Bubbles Present	Creep @ 95°C	Glass Adhesion	Gel Content
15295P	5	6 min.	1	Glass/TPE	None	—	>43.5 lbs./in.	—
	6	6 min.	1	Aluminum/TPE	None	Passed	—	—
	7	6 min.	1	Aluminum/TPE	Some	—	—	83.2 %
	D-1	7 min.	2	Aluminum/TPE	None	Passed	—	—
	D-2	7 min.	2	Aluminum/FEP	Some	—	—	73.8 %
Mod. 15295P (using Alternative curative)	H-1	6 min.	1	Aluminum/TPE	None	Passed	—	—
	H-2	6 min.	1	Glass/TPE	None	—	>31.5 lbs./in	—
	H-3	7 min.	2	Aluminum/TPE	None	Passed	—	—
	H-4	6 min.	1	Aluminum/FEP	Some	—	—	84.6 %
	H-5	7 min.	2	Aluminum/TPE	Some	—	—	53.1 %
X15303P	J-1	6 min.	1	Aluminum/FEP	Some	—	—	79.5 %
	B-1	6 min.	1	Aluminum/FEP	Some	Passed	—	—
	B-2	7 min.	2	Aluminum/FEP	Some	—	—	77.7 %
	B-3	6 min.	1	Aluminum/FEP	Some	—	—	85.3 %
	B-4	7 min.	2	Aluminum/FEP	Some	Passed	—	—
	B-5	6 min.	1	Glass/TPE	None	—	>41.0 lb/in glass broke	—
1	Aluminum/TPE = Teflon coated aluminum plate/TPE, used to separate EVA from superstrate for testing. Aluminum/FEP = Teflon coated aluminum plate/FEP, used to isolate EVA for testing.							

From the above results, it was concluded that it is possible to use a six-minute lamination cycle to process 15295P, X15303P, and the modified version of 15295P containing alternative curative to produce bubble-free glass/EVA/TPE laminates. However, the 2-stage lamination cycle involving an oven post cure requires additional time to accomplish complete cure above 80%.

Results of Laboratory Lamination Trials Based Upon Six-Minute Lamination Cycles

Further experimentation was carried out substituting the alternative “hotter” curative in place of TBEC peroxide in EVA-based encapsulant formulations based on 15295P and 15303P. The alternative curative was evaluated for its advantage in curing rate.

In replacing TBEC with an alternative curative at similar concentration and based upon a lamination cycle of 6 minutes at $160^{\circ}\text{C} \pm 3^{\circ}$, a gel content of 74.5% results. Under the same conditions the 15295 TBEC-based formulation yielded a gel content of 58.6%. To achieve a gel content in the range of 80% or greater, both peroxides required lamination processing at higher temperatures, $166^{\circ}\pm 3^{\circ}\text{C}$, for 6 minutes. In conclusion, it appears that the crosslinking efficiency of the alternative curative is poorer than that of the TBEC peroxide at similar concentrations. At curative concentrations, 80% gel content was very difficult to achieve using the alternative curative. While 80% cure has been our target, to consume as much curative as possible, it may not be necessary to cure to 80% using the alternative curative. In this instance, all of the curative may well be consumed although a lower gel content results. In the past, prior to discoloration issues arising, EVA curing to a level greater than 65% was deemed adequate to prevent cold flow of the EVA or failure in the field.

Experiments Using a 10% Vinyl Acetate EVA Copolymer-based Encapsulant Layer For Behind the Solar Cells

A series of experiments was conducted substituting 10% vinyl acetate EVA for the 32% vinyl acetate EVA. The purpose was to evaluate the utilization of a lower cost material for behind the solar cells. The 10% vinyl acetate EVA requires less cure (due to its higher melt temperature) and may offer cost, performance and processing time advantages. The 10% EVA was formulated to contain less TBEC peroxide. It was noted that when combining this EVA with the normal 32% vinyl acetate EVA front layer, the level of EVA flashing out of the laminate decreased during lamination.

Curing of the composition for six minutes at $166^{\circ}\pm 3^{\circ}\text{C}$ by vacuum lamination resulted in a gel content of 68% for the 10% EVA layer. Qualitative testing suggests that this lower gel content results in performance that is similar to curing the 32% EVA to an 80% gel content. Both materials resist cold flow at 100°C . Additional trials using the standard loading of TBEC and a 6 minute lamination cycle at 166°C yielded a gel content of $>80\%$ for the 10% EVA.

Further Optimization Experiments to Define Processing Parameters for the EVA Formulations

A series of experiments were conducted using the formulation 15303P based upon TBEC peroxide plus that formulation substituting the alternative curative for TBEC. Experiments were performed with and without 10% vinyl acetate EVA in place of the 32% vinyl acetate EVA. Processing was carried out based upon two sets of parameters as outlined below.

Process A consisted of heat up under vacuum, then pressing for 5 seconds using 1 atmosphere, followed by rapid re-pressurization of the bottom chamber, and no compression for the balance of 6 minutes.

Process B consisted heat up under vacuum, then rapidly applying atmospheric pressure to the top chamber and holding the laminate under pressure for the balance of 6 minutes.

The results from these experiments are presented in Table 15. As a key to Table 16, the standard formulation 15303P containing TBEC peroxide is designated as the “J” series, while a similar formulation substituting alternative curative for TBEC is designated as the “K” series. Conclusions from this set of experiments are:

1. Process A yielded higher gel contents as compared to lamination by Process B.
2. Incorporation of an EVA back layer composed of 10% vinyl acetate containing EVA would resist deformation or cold flow at 100°C, even with the 10% vinyl acetate EVA layer cured to only a 68% gel content.
3. At standard curative concentration, both curative-based formulations reliably processed in 6 minutes at 166°C ±3°C to adequate gel content levels.

Table 15:
EVA Processing Experiments

15303P (Alternative Curative)	Temperature °C	Process	Gel Content (%)	Passes 95°C Creep Test	Passes 100°C Creep Test
K-10	166	A	84.0	Yes	Yes
K-30	162	A	84.6	Yes	Yes
K-32	166	A	83.6	Yes	Yes
K-28	162	A	79.5	Yes	Barely
K-27	161	A	74.4	Yes	No
K-1	160	A	74.5	Yes	No
15303P (TBEC Peroxide)	Temperature °C	Process	Gel Content (%)	Passes 95°C Creep Test	Passes 100°C Creep Test
J-12	166	A	88.2	Yes	Yes
J-42	166	A	85.9	Yes	Yes
J-3	163	A	84.5	Yes	Yes
J-1	163	A	79.5	Yes	Barely
J-32	160	A	58.6	Yes	No
15303P (TBEC or Alternative Curative) /10% EVA Layer	Temperature °C	Process	Gel Content (%)	Passes 95°C Creep Test	Passes 100°C Creep Test
J-52/G	166	B	71.1	Yes	Yes
J-50/G	163	B	68.1	Yes	Yes
K-39/G	160	B	67.5	Yes	Yes
J-47/G	166	A	85.7	Yes	Yes
J-43/G	166	A	78.3	Yes	Yes
K-3/G	161	A	74.8	Yes	Yes

Dynamic Stability Testing of Alternative Curative EVA Formulations

The ability to process the alternative curative-based formulations was assessed. Based upon a series of rheological studies conducted using a Brabender Plasti-corder to measure the encapsulant's change in melt viscosity versus time at various processing temperatures, it was determined that the formulations based upon the alternative curative are sufficiently stable to process through standard manufacturing equipment using typical EVA encapsulant processing parameters.

Determination of the Effects of Curative Concentration

Based upon a series of qualitative cure efficiency tests and then comparing those results to gel testing, it was concluded that an 80% gel content may be necessary to prevent EVA deformation in a PV module during long-term exposure at 90°C. These results suggest that EVA gel contents ranging between 75-80% may evidence cold flow or creep upon long-term exposures at 90°C.

On that basis, a series of experiments were conducted to determine the effect of curative concentration versus cure temperature at a constant lamination time of 6 minutes. Each of two curatives was evaluated, TBEC and the candidate alternative curative. The EVA was fully formulated based upon the X15303P “fast-curing” grade. The results are presented in Table 16.

Table 16:
Gel Contents vs. Peroxide Type, Curative Concentration, and Platen Temperature

Sample ID.	Curative	Curative Conc.	Platen Temp.	Gel Content
J-32	TBEC	A	160°C	58.6%
J-3	TBEC	A	163°C	84.5%
J-1	TBEC	A	163°C	79.5%
J-42	TBEC	A	166°C	85.9%
J-12	TBEC	A	166°C	88.3%
K-53	Alt. Curative	A	149°C	64.8%
K-1	Alt. Curative	A	160°C	74.5%
K-27	Alt. Curative	A	161°C	74.5%
K-28	Alt. Curative	A	162°C	79.5%
K-10	Alt. Curative	A	166°C	84.0%
K-32	Alt. Curative	A	166°C	83.6%
M-1	TBEC	D	163°C	84.4%
M-2	TBEC	D	166°C	88.7%
M-3	TBEC	D	166°C	91.8%

An additional series of gel determination experiments were conducted based upon the above experimental series of J, K, and M using a 10-minute lamination cycle at 166°C. Those gel content values are presented in Table 17.

Table 17:
Gel Contents vs. Curative & Concentration at 10 Minutes at 166°C

Sample ID.	Curative	Curative Conc.	Platen Temp./Time	Gel Content
J-67	TBEC	A	166°C/10 Min.	91.5%
K-54	Alt. Curative	A	166°C/10 Min.	85.8%
M-4	TBEC	D	166°C/10 Min.	92.0%

A third series of experiments were conducted using the “fast-curing” 15295P EVA-based encapsulant. Once again a 6-minute lamination cycle was utilized. The results are presented in Table 18.

Table 18:
Gel Contents of 15295P EVA vs. Lamination Temperature

Sample ID.	Lamination Time	Platen Temp.	Gel Content
15295P-4	6 Min.	163°C	79.7%
15295P-5	6 Min.	166°C	87.2%
15295P-12	6 Min.	166°C	88.0%

Based upon the data generated in the above experiments, it appears that each of the curative compositions will provide adequate cold flow/creep resistance at 90°C when laminated using a 6-minute cycle at 163°C or higher. The data also suggests the curative formulated at higher concentrations may adequately crosslink the EVA.

An additional series of lamination trials were conducted using larger laminates. The intent was to explore the effects of laminate size on the degree of cure. The results are presented in Table 19.

Table 19:
Gel Content Determination Using Larger Laminates vs. TBEC Concentration

Sample ID.	Laminate Size	TBEC Peroxide	% Gel Content	Lamination Time
1	6" x 6"	B	87.0	6 min.
2	5" x 5"	B	88.6	6 min.
3	6" x 6"	B	89.6	6 min.
4	6" x 6"	C	92.6	6 min.
5	6" x 6"	C	92.0	6 min.
6	6" x 9"	C	88.5	6 min.
7	6" x 6"	E	93.9	6 min.
8	6" x 6"	E	91.5	7 min.

It was concluded from these experiments that these larger laminates performed similar to the smaller laminates. It was further noted that modifying the curative concentration does not appear to modify the level of measurable gel or degree of cure.

A further set of experiments was conducted on even larger laminates. Although a tremendous degree of bubbling was encountered initially at 149-150°C, it was determined that by insuring complete air removal prior to melting of the encapsulant, the bubbles could be avoided. As a result, bubble free laminates have been demonstrated at a laminator platen temperature of 166°C.

Formulating for Lower Temperature Lamination Processing

Laboratory efforts have demonstrated that a 6-minute lamination cycle at 163° - 166°C will yield a non-cold flowing EVA at 95° - 100°C based upon STR's qualitative cure efficiency test. However, with the PV communities' difficulties associated with bubble propagation at temperatures greater than 155° - 160°C, it is desirable to maintain laminator platen temperatures at 150°C or less. It is unlikely that today any PV module processor using EVA-based encapsulant is laminating at platen temperatures above 160°C.

Prior laboratory trials demonstrated that with a slow enough temperature ramping to 165°C bubble formation can be prevented. However, it was probably a function of allowing enough time for all trapped air and evolved volatiles to be evacuated prior to cure. The encapsulant formulations developed thus far are not capable of resisting creep or cold flow at 95°C based upon a six-minute lamination cycle at 149°C. Therefore, further investigations were performed at various concentrations of curative at various platen temperatures based upon a 6-minute lamination cycle. The results of modifying the curative concentrations for the candidate encapsulant formulations are presented below in Tables 20, 21 and 22.

Table 20:
Modified X15303P EVA at TBEC Peroxide Concentration E

Experiment No.	Platen Temp. °C	% Gel Content	Qualitative Cure Testing @ 95°C/10 min.
53	149	68	Failed
87	152	72	Passed
67	154	73	Passed
79	154	74	Passed
70	157	85	Passed
80	157	83	Passed
71	160	83	Passed

Table 21:
Modified X15303P EVA at TBEC Peroxide Concentration D

Experiment No.	Platen Temp. °C	% Gel Content	Qualitative Cure Testing @ 95°C/10 min.
88	152	68	Failed
66	154	75	Passed
68	154	84	Passed
69	157	83	Passed
82	160	84	Passed
83	163	85	Passed

Table 22:
Modified X15303P EVA at Alternative Curative Concentration E

Experiment No.	Platen Temp. °C	% Gel Content	Qualitative Cure Testing @ 95°C/10 min
75	149	63	Failed
89	152	67	Failed
76	154	74	Passed
81	157	83	Passed
77	160	86	Passed

A kinetics model was developed to explain the effects of temperature and curative concentration on passage of the qualitative cure test. The rate-determining step is the decomposition rate of the curative. Then, if comparison with standard concentration of TBEC peroxide at 149°C platen temperature and a lamination cycle of 10 - 12 minutes is made, the following model results (concentration effect is first order, temperature effect is second order). The goal of any other system is to match this.

So: $1.0 = k (\text{rate constant}) (\text{conc}_2 / \text{conc}_1) (\text{temp}_2 / \text{temp}_1)^2$ where t_2 is the final value, conc_1 = standard Conc. of TBEC peroxide; $\text{temp}_1 = 149^\circ\text{C}$.

Thus: $t_2 = \sqrt{(149)^2 [1/k (\text{conc}_2 / \text{conc}_1)]}$. For the 6- minute system

The standard concentration of TBEC peroxide using a 6-minute lamination cycle at a platen temperature of 168°C was determined to result in an equivalent cure to standard concentration of TBEC peroxide processed for 12 min. at 149°C. Solving for k from the above equation results in $k = 0.79$; this means that utilizing a 6-minute lamination cycle at 149°C results in a 79% conversion of standard concentration of TBEC type into the same product at 10-12 min. at 149°C. Using this approach, processing temperatures and curative concentrations are theoretically predictable.

Qualification of the Gel Test

The data presented in Table 23 was obtained using EVA formulated with higher concentrations of TBEC peroxide, processed in our laboratory laminator using a 6-minute lamination cycle. Actual platen temperatures are presented.

Table 23:
Qualification of the Gel Test Results

Experiment No.	TBEC Peroxide Conc.	Platen Temperature °C	% Gel Content
51	E	138	2.1
65	E	143	4.8
52	D	149	45
53	D	149	68
54	E	143	1.8

Based upon the dramatic changes in the measured gel contents from one lamination temperature to another, the simple mechanism of crosslinking cannot explain the magnitude of the differences. Apparently, there is another mechanism involved, namely chain entanglement, which is a well-known occurrence in rubber curing. At some point, chain length becomes quite long and chains form an entangled super structure. Analysis for gel content involves heating in toluene at 60°C with little or no shearing. In this process the activation energy to convert swollen gels into solution isn't provided. Therefore, various levels of measured gel content may actually be crosslinked to different degrees and actually cured to different levels. Due to the chemical bond formation of some of the final crosslinked compositions, it was subsequently found necessary to substitute chloroform for toluene to achieve accurate gel content values. For some formulations the toluene had a tendency to swell the encapsulant as opposed to completely dissolving the encapsulant. As a result, the swelled EVA became very sticky and would adhere to the filter media, and result in erroneously low reported gel contents.

Quantitative Analysis of Candidate Faster-Curing EVA-Based Encapsulant Cure Kinetics

Based upon the results from gel testing, additional formulations were compounded to improve upon the EVA-based encapsulant's cure rate kinetics. These encapsulant formulations were then characterized for their curing rate kinetics using a Monsanto MDR 2000 Moving Die Rheometer in accordance with ASTM D 6204-97, Standard Test Method for Rubber – Measurement of Unvulcanized Rheological Properties Using Rotorless Shear Rheometers. The rheometer measures the cure characteristics of encapsulants through use of a sealed rotorless moving die system. The reaction torque correlates with the degree of crosslinking as a function of cure time. For each of twelve formulations submitted, including STR's 15295P commercial "fast-cure" control, measurements were carried out at 150°, 155° and 160°C over 12-minute test exposures. Torque versus time is recorded.

The graphic representations of the torque versus time values at 150°, 155° and 160°C are depicted in Figures 19, 20 and 21, respectively. As depicted in Figure 1, the control's (15295P) maximum torque was 3.15 in-lb. and required 12 minutes to achieve that level. A maximum torque for the control of 3.21 in-lb. was acquired at 155°C in 8.3 minutes and in 6.0 minutes at 160°C, suggesting that 2% additional cure could have been achieved in some timeframe exceeding 12 minutes at 150°C. The test results further suggest that increasing the control encapsulant's cure temperature by 10°C, from 150° to 160°C, results in a >50 percent decrease in cure time.

Figure 19:
Moving Die Rheometry Results @ 150°C

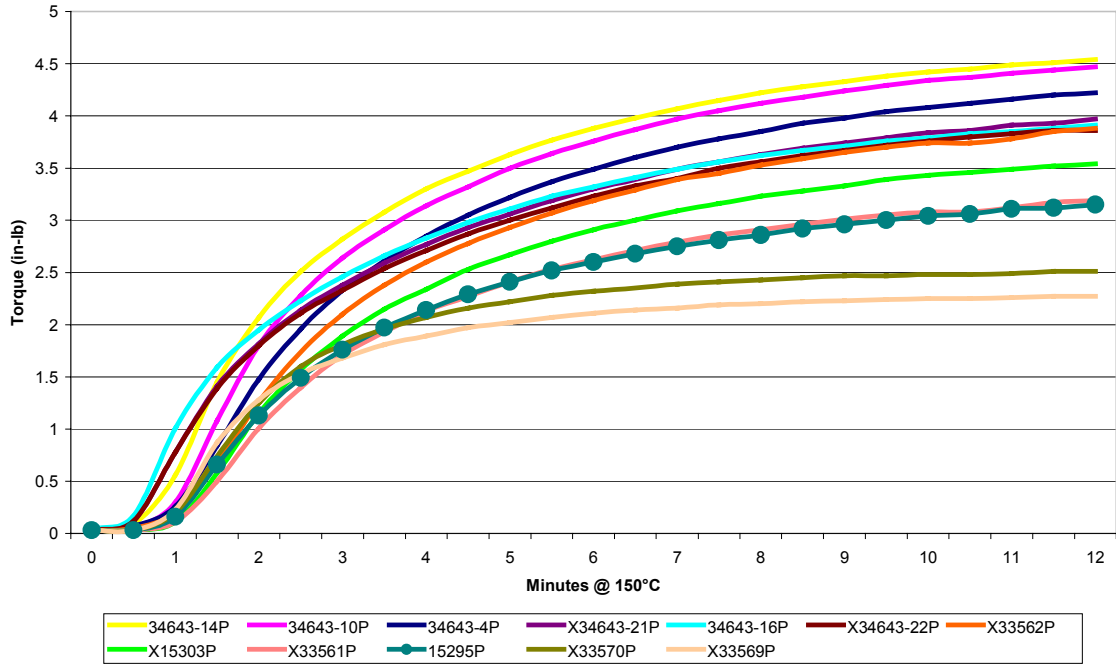


Figure 20:
Moving Die Rheometry Results @ 155°C

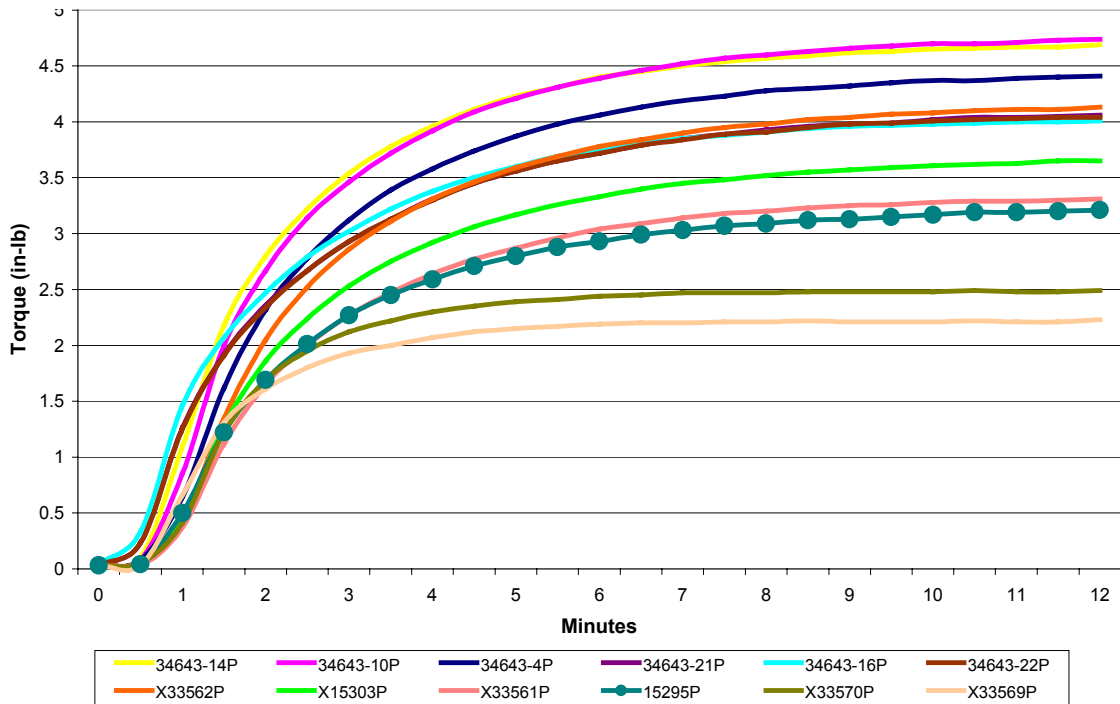
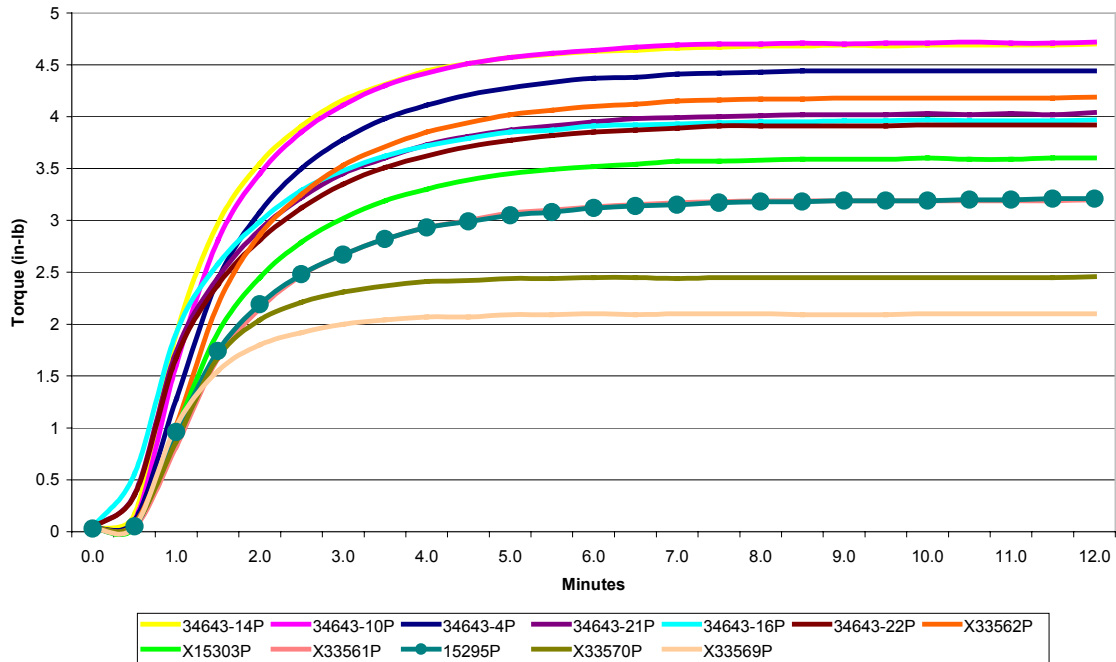


Figure 21:
Moving Die Rheometry Results @ 160°C



One of the important parameters is peak rate, a function of torque over time. This correlates with the encapsulant's curing rate at the test temperature. At 150°C, the control (15295P) EVA encapsulant has a measured peak rate of 1.1. By increasing the test temperature 5°C, the control's peak rate increased 46%. Raising the test temperature a total of 10°C further to 160°C increased the peak rate by 115% over the 150°C peak rate. The fastest-curing experimental formulation (X34643-14P) demonstrated peak rate advantages of 76%, 79% and 83% versus the control at 150°, 155° and 160°C respectively.

In addition to the Moving Die Rheometry results, gel content data resulting from the lamination of test coupons at 140°C revealed that the experimental EVA-based encapsulants could be cured to the targeted cure levels. Cure levels or gel contents exceeding 70% in 4 minute and 80% in 5-minute lamination cycles were observed at 140°C. The results of those trials are presented in Table 24.

Table 25 compares the maximum torque values, as well as the rate and degree of cure for the 11 experimental formulations tested by Moving Die Rheometry and for the control at 150°, 155° and 160°C. Each experimental formulation demonstrated varying cure rate advantages, though X33569P and X33570P cured to lower torque values, suggesting that both cure time and cure efficiency are equally important criteria. Experimental formulations X34643-10P and -14P resulted in maximum torque values approximately 45% higher than the control, suggesting a substantial increase in the number of crosslinkage sites, though not necessarily resulting in higher measured gel content. The peak rate, measure of the torque versus time relationship, indicated a 76% gain in cure rate based upon X34643-14P at 150°C.

Table 24:
Cure Level of Laboratory Laminate Specimens Prepared @ 140°C

Formulation	Cure Time	Gel Test Employing	
		Toluene	Chloroform
X33561P	6 min.	44%	49%
X33562P	6 min.	63%	70%
X34643-4P	4 min.	70%	78%
X34643-4P	5 min.	80%	84%
X34643-4P	6 min.	85%	87%
X34643-10P	4.5 min.	72%	77%
X34643-10P	5 min.	74%	77%
X34643-10P	6 min.	83%	85%
X34643-14P	5 min.	75%	80%
X34643-14P	6 min.	80%	88%
X34643-16P	5 min.	72%	78%
X34643-16P	6 min.	78%	84%

Table 25:
Moving Die Rheometry Results for the Faster-Curing Formulations vs. the Controls

Formulation	Moving Die Rheometry Results @ 150°C, 12 Minutes				Moving Die Rheometry Results @ 155°C, 12 Minutes				Moving Die Rheometry Results @ 160°C, 12 Minutes			
	Torque (in-lb)		TC 90 ⁽¹⁾	Peak Rate	Torque (in-lb)		TC 90 ⁽¹⁾	Peak Rate	Torque (in-lb)		TC 90 ⁽¹⁾	Peak Rate
	Min.	Max			Min.	Max			Min.	Max		
15295P Control	0.03	3.15	7:40	1.10	0.03	3.21	5:36	1.62	0.03	3.21	3:50	2.36
X15303P	0.03	3.54	7:35	1.22	0.03	3.65	5:37	1.84	0.03	3.60	3:43	2.72
X33561P	0.03	3.19	7:42	1.04	0.03	3.31	5:36	1.60	0.03	3.20	3:44	2.32
X33562P	0.03	3.88	7:44	1.26	0.03	4.13	5:40	1.95	0.03	4.19	3:40	2.89
X33569P	0.03	2.27	5:11	1.38	0.03	2.23	3:30	1.96	0.03	2.10	2:20	2.53
X33570P	0.03	2.51	5:21	1.29	0.03	2.49	3:36	1.77	0.03	2.46	2:30	2.43
X34643-4P	0.03	4.22	7:37	1.38	0.03	4.41	5:27	2.13	0.03	4.44	3:34	3.17
X34643-10P	0.03	4.47	7:21	1.75	0.03	4.74	5:13	2.72	0.03	4.72	3:22	4.02
X34643-14P	0.03	4.54	7:05	1.94	0.03	4.69	4:58	2.90	0.03	4.70	3:11	4.32
X34643-16P	0.04	3.91	7:15	1.91	0.04	4.01	5:04	2.78	0.04	3.97	3:16	3.67
X34643-21P	0.03	3.97	7:35	1.56	0.03	4.06	5:32	2.32	0.04	4.04	3:36	3.27
X34643-22P	0.03	3.86	7:35	1.54	0.03	4.04	5:24	2.27	0.04	3.92	3:36	3.19

(1) TC90 is the time it took to achieve a 90% level of maximum torque

Table 26 shows the cure time necessary for each candidate formulation to achieve a similar level of torque or cure versus the control at 150°, 155° and 160°C. The greatest advantage was observed with X34643-14P, accomplishing the control's 12-minute torque level in just 3.6 minutes at 150°C. Other formulations tested offered varying levels of advantages as indicated. Further, the results demonstrate the dramatic affect that processing temperature has on cure rate.

Table 26:
Time to Achieve Full Cure of Control @ Process Temperatures
(3.15 in-lb. Torque)

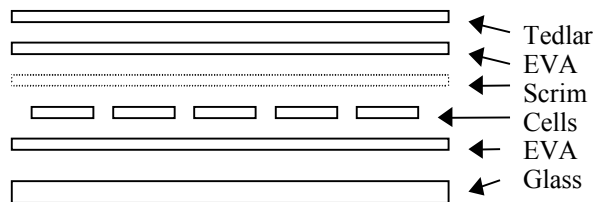
Formulation	150°C	155°C	160°C
15295P Control	12.0 min.	8.3 min.	6.0 min.
X15303P	7.3 min.	4.8 min.	3.3 min.
X33561P	10.8 min.	6.7 min.	5.7 min.
X33562P	5.6 min.	3.5 min.	2.3 min.
X33569P	NA	NA	NA
X33570P	NA	NA	NA
X34643-4P	4.8 min.	4.2 min.	2.0 min.
X34643-10P	4.0 min.	2.5 min.	1.5 min.
X34643-14P	3.6 min.	2.4 min.	1.5 min.
X34643-16P	5.0 min.	3.2 min.	2.2 min.
X34643-21P	5.3 min.	3.5 min.	2.4 min.
X34643-22P	5.6 min.	3.5 min.	2.5 min.

Prototype MSX-60 Module Lamination Trials

Multiple lamination trials were conducted on full-scale BP Solar MSX-60 PV modules as qualification for each viable experimental encapsulant.

Initial trials involved fabrication of laminates using a SPI-LAMINATOR™ 350 at platen temperatures of 150°, 155° and 160°C. The laminates employed non-tempered float glass and 11.4 x 11.4 cm polycrystalline silicon wafers in place of actual solar cells. No solder, flux or ribbons were introduced during the initial trials. Craneglas 230 nonwoven glass scrim was incorporated between the substrate side encapsulant and wafers and a Tedlar™ backsheet was employed. The configuration is depicted in Figure 22. Sixteen wafers were used per mock-up, encompassing approximately 40% of the module with cells, and the remaining 60% was cell free.

Figure 22:
Lay-up of the Prototype Laminates



Subsequent lamination trials were conducted utilizing a Spire 240A laminator with an actual solar cell matrix incorporated to fabricate actual MSX-60 PV modules. A broad range of lamination temperatures was studied based upon a total laminator process time of 5 and 6 minutes. Cure levels were determined by Gel Content tests using chloroform and/or toluene, as appropriate.

As indicated in Table 27, gel contents as high as 88-91% were measured on samples representative of actual PV modules processed in 6 minutes using PV module components and a standard production laminator. Table 28 indicates that cure levels as high as 80% were achieved using a 5-minute lamination cycles. Modules from this experiment underwent the thermal cycling portion of IEC 1215 as an initial qualification of the level of cure. Through 400 cycles, no evidence of encapsulant failure or movement was observed.

Table 27:
Six-Minute Lamination Trial Results

Lamination cycle = 6 minutes (105 sec pump, balance press)				
EVA Type	Lamination Temp. (°C)	Temp. Dot (°C)	Avg. Gel Content (%)	Comment
15295P Control	143	132	53	Good
X33561P	143	143	13	Good
X33562P	143	132	59	Good
X33569P	143	132	33	Few small bubbles
X33570P	143	132	71	Good
X33578P	143	132	45	Good
X34643-4P	143	132	91	Good
X34643-10P	143	132	71	Good
X34643-16P	143	132	63	Good
15295P Control	148	143	46	Few small bubbles
X33561P	148	143	43	Blister & bubbles
X33562P	148	143	64	Good
X33569P	148	143	66	Blisters & bubbles
X33570P	148	143	89	Blisters & bubbles
X33578P	148	148	80	Good
X34643-4P	148	143	84	Good
X34643-10P	148	143	88	Good
X34643-16P	148	143	88	Good

Table 28:
Five-Minute Lamination Trial Results

Lamination cycle = 5 minutes (105 sec pump, balance press)				
EVA Type	Lamination Temp. (°C)	Temp. Dot (°C)	Avg. Gel Content (%)	Quality
15295P Control	153	143	74	Bubbles
X33561P	153	143	71	Bubbles
X33562P	153	143	70	Good
X33569P	153	143	73	Bubbles & blisters
X33570P	153	143	71	Bubbles
X34634-10P	153	143	56	Good
X34634-16P	153	143	52	Good
X33578P	157	NA	76	Gel Specimen Only
X34634-4P	157	143	47	Good

Physical Property Determinations

Table 29 presents the measured physical properties for each formulation. Each formulation was cured in a laboratory vacuum laminator based upon a total lamination cycle time of 6 minutes. Each formulation was qualified for its degree of cure and resulting physical properties as presented. The variation in cure level is known to have an effect on the resulting tensile strengths and ultimate elongation properties and likely accounts for some of the variability.

Table 29:
Physical Properties of Candidate Encapsulant

	X3356 1P	X3356 2P	X3356 9P	X3357 0P	X3357 8P	X34643- 4P	X34643- 10P	X34643- 14P	X34643- 16P
Adhesion to Glass (lbs./inch)	Not Tested	Not Tested	>30	~14	~17	~20	~21	~24	~16
Adhesion to Tedlar (lbs./inch)	Not Tested	Not Tested	~10	~4	~3	~4	~3	~5	~2
Tensile Strength (psi)	1,770	2,030	2,330	2,050	1,580	2,010	1,590	1,480	1,580
Ultimate Elongation (%)	660	570	720	700	590	600	580	530	570
Cure Level or Gel Content (%)	80	80	89	90	92	92	93	91	92
Hardness Durometer - Shore A	72	68	70	70	68	69	67	71	72
Hardness Durometer - Shore D	21	20	22	21	20	21	20	22	23

Following the laboratory 6-minute lamination trials, and those trials conducted at BP Solar, experimental formulation X34643-4P was found to demonstrate quite promising processing attributes as well as physical properties. Therefore, it was selected for characterization of its key physical properties versus the 15295P Control. The specimens were prepared for testing at an 80% cure level. The values of those key physical properties are presented in Table 30. The data suggests that X34643-4P is quite comparable to the control 15295P formulation.

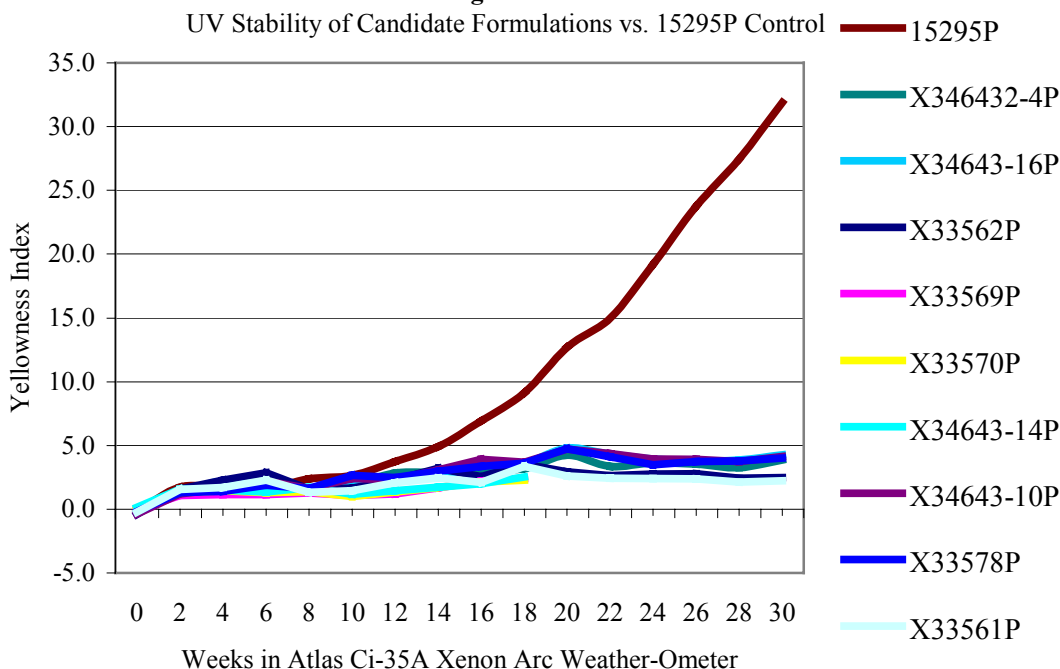
Characterization of UV Stability of Candidate Faster-Curing EVA Formulations

Samples of several candidate “faster-curing” EVA formulations were qualified over the course of the contract to evaluate their UV stability characteristics. Each formulation was laminated between a non-UV screening glass superstrate, i.e. old AFG Solite glass, and substrate composed of window glass. The laminates were prepared in accordance with a standard 15295P lamination cycle. Each EVA formulation was qualified for its UV stability versus STR’s 15295P control using an Atlas Ci-35 Xenon Arc Weather-Ometer. The conditions were based upon a black panel temperature of 89°C, 50% relative humidity, and an irradiation exposure of 0.55 watts/cm² @ 340 nm (2 suns), for up to 30 weeks. The UV was filtered at ~285 nm to more closely simulate terrestrial conditions. A graphic representation of each candidate formulation’s UV aging characteristics is depicted in Figure 23. Degradation is reported as a function of increasing yellowness index as measured by ASTM D-1925. After 30 weeks, the 15295P control had generated a yellowness index of ~32, whereas the experimental formulations were all tracking to be less than 5, a minimal level of degradation, which remained undetectable by eye.

Table 30:
Key Physical Properties of X34643-4P versus 15295P at 80% Cure Level

Property	15295P	X34643-4P
% Light transmission	91	92
Adhesion to glass (lbs./inch)	43	29
Adhesion to Tedlar (lbs./inch)	4.4	3.6
Tensile strength (psi)	2,100	2,010
Elongation (%)	575	600
Avg. % crosslinking	80	80
Crosslinking time & temp.	10 min. at 150°C	6 min. at 145°C
Hardness (Durometer – shore A)	70	69
Tensile modulus (psi)	1,750	1,800

Figure 23:



Optimization of the Best Candidate Formulations Improved Adhesion and Processing

Earlier characterization of formulations X34643-4P and X34643-16P revealed a significant reduction in adhesive strength to glass and Tedlar as compared to the 15295P control EVA formulation. The 15295P formulation, at a cure level of 80% gel content, yields an adhesive strength of 43.0 and 4.4 pounds per inch to glass and Tedlar, respectively, based upon a 180° peel at room temperature. The experimental X34643-4P formulation, at 80% gel content, yielded an adhesive strength of 29.0 and 3.6 pounds per inch

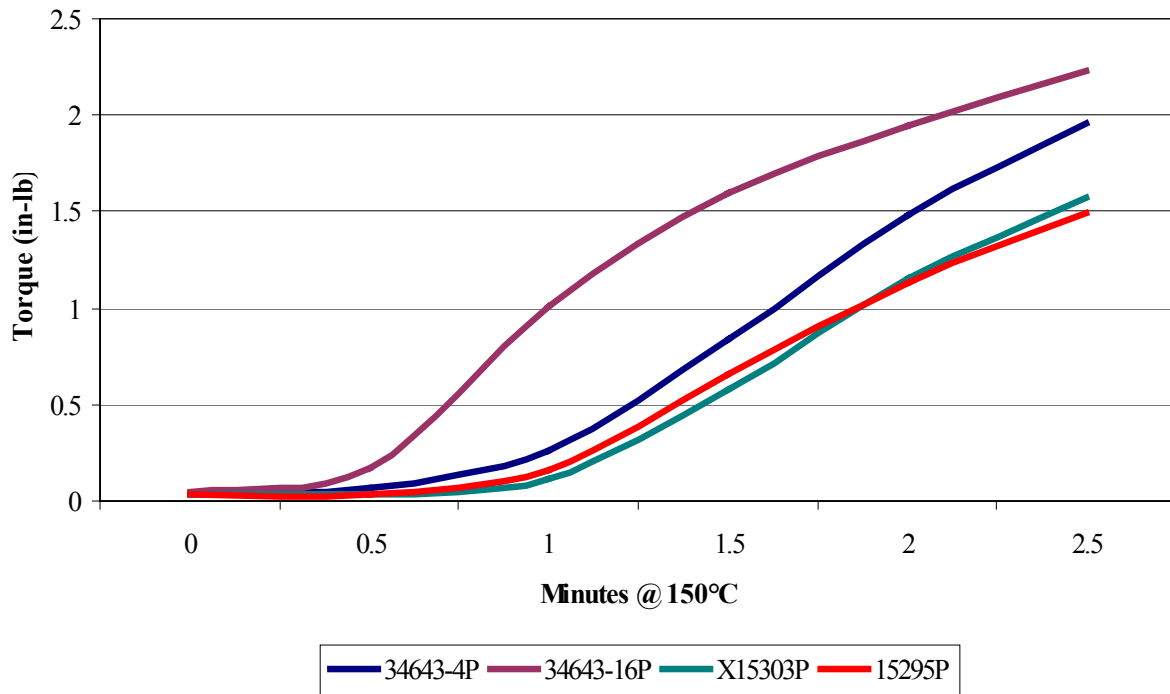
to glass and Tedlar, while the X34643–16P formulation was slightly worse yielding 16.0 and 2.2 pounds per inch, respectively.

Experimental reformulation efforts suggested that the adhesive strengths of the experimental formulations can be substantially improved by (1) incorporating additional loadings of the co-agents used to accelerate the rate of cure, or by (2) incorporation of other traditional adhesion promoters as added formulation constituents. By either method, experimental variations of the candidate formulations were modified to yield adhesive strengths to glass in the range of 70 pounds and 12 pounds to Tedlar.

However, based upon prototype processing trials, the strategy on incorporating additional concentrations of the co-agents, used to accelerate cure was aborted. The additional co-agents further increased the formulations' curing rate kinetics. As a result, premature crosslinking was noted during extrusion processing rendering the formulations non-processable.

Subsequent efforts concentrated on evaluating the processability of the slightly modified versions of the X34643–4P and X34643–16P candidate faster-curing EVA formulations. Rheological studies conducted by Moving Die Rheometer (MDR) as presented in Figure 24. indicates within the first 2.5 minutes of elevated temperature exposure, the X34643–16P EVA formulation initiates crosslinking nearly 2 times faster than the 15295P and X15303P controls, and continues to crosslink rapidly. The X34643–4P formulation initiates crosslinking only slightly faster than the controls but continues to crosslink at an accelerated rate. While the MDR characterized the rates and degree of crosslinking, it's results are not easily translatable to predict the difficulties in converting the formulations into encapsulant via extrusion methods.

Figure 24:
Moving Die Rheometry Results
(0-2.5 Minutes @ 150°C)



Prior experience gained during fabrication of candidate encapsulants of the X34643–4P and X34643–16P formulations correlated with the MDR findings, though both formulations proved difficult to process. The X34643–16P was especially difficult as the extrudate began crosslinking during extrusion conversion of the first 2 rolls of prototype product, even though processing was ultimately accomplished by processing at exceptionally slow speeds to minimize the shear rate.

Therefore, efforts were undertaken to examine the possibility of broadening the processing window for the experimental formulations using standard manufacturing equipment through minor formulation adjustments. Four sets consisting of minor formulation variations for both the X34643–4P and X34643–16P EVA formulations were evaluated versus the 15295P and X15303P EVA controls. Differentiation between formulation processing was monitored by recording the time to achieve minimum torque, the time to initiate crosslinking, the formulation temperature at the point of crosslinking and the torque imparted by the formulation at the time of crosslinking initiation using the above-described conditions. The results are presented in Table 31.

Table 31:
Brabender Processing Trials of Candidate Faster-Curing EVA Formulations

	Control 15295P	Control X15303P	34643-4P	34908-4P	34928-4P	34942-4P	34643- 16P	34908- 16P	34928- 16P	34942-16P
Date Processed	12/7/00	12/14/00	12/14/00	12/7/00	12/7/00	12/14/00	12/14/00	12/7/00	12/7/00	12/14/00
Process Temp. (°C)	99	99	99	99	99	99	99	99	99	99
Shear Rate (RPM)	60	60	60	60	60	60	60	60	60	60
Minimum Torque Value (M-G)	950	930	925	900	875	930	880	890	920	875
Time at Minimum Torque Value (Min.)	18.0	14	10.3	9.0	12.0	11.0	8.0	11.8	9.0	8.0
Time to Initiate Crosslinking (min.)	48.5	51	23	23.3	28.1	23.5	16	26.8	22	14.75
Temp. (°C) @ Crosslink Initiation	119	124	121.5	128.5	121	121	NA	120	133	123
Torque @ Crosslinking Initiation (M-G)	1,550	1,550	1,690	1,850	1,750	1,750	1,575	1,775	1,850	1,725

As presented, the control formulations 15295P and X15303P required 48.5 and 51 minutes, respectively, to initiate crosslinking, whereas the four variations of the –4P formulation ranged between 23 and 28 minutes, and the –16P formulation variations ranged between 14.7 and 26.8 minutes. Minimum torque values in all cases were felt to be similar, whereas the times to reach minimum torque are longer for the control formulations. The elevated batch temperatures noted at crosslinking initiation versus the controls were hypothesized to indicate that crosslinking is proceeding rapidly.

Pilot Manufacture of X34928-4P Faster-Curing EVA

Rheological testing has proven that the series of -16P EVA formulations undergo crosslinking initiation far too rapidly to process on standard extrusion manufacturing equipment. Crosslinking initiation occurs nearly 2 times faster than the 15295P commercial control. Once initiated, crosslinking continues rapidly at elevated temperatures. The kinetics of the crosslinking mechanism are far more favorable for the -4P formulations series, where initial crosslinking occurs only slightly faster than the control at similar temperatures, but then continues to crosslink at an accelerated rate. Those kinetic differences between the -4P and -16P formulations render the -4P formulations more favorable for processing.

Subsequently, using standard commercial EVA encapsulant production equipment, STR processed the X34928-4P experimental “faster-curing” EVA formulation using normal process temperature parameters. It should be pointed out however, that it was necessary to compensate for the higher reactivity of the X34928-4P formulation by processing at 50% of the normal throughput rate to prevent premature crosslinking in the production equipment.

Key Physical Properties of X34928-4P “Faster-Curing” EVA

Once processed, the extruded X34928-4P “faster-curing” EVA encapsulant was evaluated for its key physical properties versus the 15295P control. Those evaluations included determinations of adhesive strength to glass and Tedlar, tensile properties including elongation, plus degree of crosslinking by (toluene extracted) gel content using 5- and 6-minute lamination cycles. Those results are presented in Table 32.

Although the reported adhesion to glass strength for the X34928-4P formulation appears lower than for the control, they in fact may be similar. The 180-degree peel test specimen was laminated to the glass using an aluminum foil backing to support the EVA. During testing, the aluminum foil stripped away from the EVA, leaving the EVA bonded to the glass. The peel strength is reported to exceed the measured value at which the aluminum foil released from the EVA.

Table 32:
Key Physical Properties of Prototype X34928-4P EVA-Based Encapsulant

Physical Property	15295P @ 80% Gel Content	X34928-4P
Average adhesion strength to clean glass (lbs.)	43	>29.9
Average adhesion strength to blue Tedlar (lbs.)	4.4	18.2
Average tensile strength (psi)	2,100	1,610
Average elongation (%)	575	500
Gel Content (6 min. @ 148°C)	-	85%
Gel Content (5 min. @ 157°C)	-	67%
Gel Content of Encapsulant as Manufactured	2.8%	3.0%

Table 33 illustrates a comparison of cure levels for the experimental X34928-4P “faster-curing” EVA versus the 15295P control. Test specimens were collected from pilot production run of the faster-curing EVA-based encapsulant X34928-4P and 15295P. Each was laminated and cured in a laboratory vacuum laminator at 145°, 150° and 155°C. The degree of cure or gel content was determined in accordance with STR’s Test Protocol for the Determination of Gel Content of Crosslinked EVA-Based Encapsulant. The lamination steps consisted of an evacuation followed by a press under vacuum using atmospheric pressure. Gel contents of 80% or greater were targeted. The resulting cure levels obtained are presented in Table 33.

Table 33:
Cure Level Comparisons of X34928-4P Faster-Curing EVA vs. the 15295P Control

Formulation	Lamination Time	Lamination Temperature	Gel Content
X34928-4P	5	145°C	71.4%
X34928-4P	6	145°C	76.8%
15295P	12	145°C	80.1%
X34928-4P	5	150°C	80.3%
X34928-4P	6	150°C	82.5%
15295P	12	150°C	82.4%
X34928-4P	5	155°C	84.5%
X34928-4P	6	155°C	88.1%
15295P	12	155°C	87.4%

Sample rolls of the X34928-4P were submitted to BP Solar. Modules were fabricated using the 6 minute cure cycle. These modules were then subjected to testing in accordance with IEC 61215 with an increase in the number of thermal cycles from 200 to 500 and the addition of the wet insulation test from IEC 61646. The modules successfully passed all parts of this test sequence except for the wet insulation test performed after the damp heat test. The two modules made with X34928-4P had leakage values of 110 and 330 μ A at 600 volts measured within 3 hours of removal from the damp heat chamber. The pass criteria for this size module is 65 μ A. Modules made at the same time using the 15295 control material passed the wet high pot test.

Often modules fail this wet insulation resistance test because of humidity induced loss of adhesion between the EVA and glass. The adhesion of the EVA to glass in these samples was measured at 21.4 lbs and 32.6 lbs. respectively. From our experience anything above 20 lbs is good enough to pass the wet insulation test. So the failure of the wet insulation test is not due to poor EVA to glass adhesion. At this time we do not understand why the faster cure EVA is showing this failure.

STR reported that a switch to production of the new faster cure EVA is not a simple exercise. The kinetics of crosslinking the X34928-4P encapsulant requires far less activation energy than the control, and therefore presents processing difficulties during its conversion into encapsulant sheet. Processing runs to date have proceeded at approximately 50% the normal throughput rate. Therefore the advantages associated with the converted encapsulant is probably cost prohibitive, due to the cost of the extended machine time involved in processing. Further research and process development efforts are required to improve upon the encapsulant's processing characteristics.

Since BP Solar is looking for a faster processing material in the near term, STR recommended a renewed effort to evaluate the use of X15303. STR experiments indicate that use of this material instead of 15295 could result in a reduction of process time from 12 minutes to 9 minutes. Quantities of X15303 were prepared by STR and shipped to BP Solar. Modules were fabricated using the 9 minute cure cycle. These modules have begun testing in accordance with IEC 61215 with an increase in the number of thermal cycles from 200 to 500 and the addition of the wet insulation test from IEC 61646.

3.5.2 Moisture Vapor Transmission Rate

The degradation caused by moisture during aging of PV modules, has recently become a PV industry focus, especially with regard to thin film technologies. Therefore, some effort was expended to examine the feasibility of modifying the EVA to decrease the PV encapsulant's moisture vapor transmission rate (MVTR), thereby possibly rendering a PV module more hydrophobic. A series of experiments were undertaken to evaluate the incorporation of various additives into the EVA encapsulant, then measuring the EVA's MVTR. The study was accomplished by incorporating various additives into the EVA via standard plastics compounding techniques

Measurement of the candidate encapsulant's MVTR was accomplished using a modified test method based upon ASTM E-96, employing desiccant filled vapometers, sealed with the cured EVA-based encapsulant test films. However, as opposed to using the standard ASTM environmental conditions, conditions were set at 85°C and 100% RH. The amount of moisture absorbed by the desiccant, passing through the test film is measured versus exposure time, surface area and thickness of the test film. Each of those parameters is used to calculate the moisture vapor transmission rate (MVTR) of the test film. The MVTR is reported as grams/mil/24 hrs/100% RH/85°C/100 sq. inches. As a baseline for improvement, the unmodified 15295P EVA based on Elvax 3185 was measured to have a nominal MVTR of 900g/mil/24 hrs/100% RH/85°C/100 sq. inches. As further qualification, those formulations showing promise were further evaluated for feasibility by measuring their adhesive strength to aluminum and to the 15295P control, following lamination. Adhesive properties were monitored using a simple 180° peel test.

Initially numerous formulation modifications were undertaken with little success. Only minor reductions to the EVA's MVTR were accomplished while still maintaining good adhesion to aluminum. In summary, the inclusion of additives including talc and mica fillers at loadings ranging from 5-15% yielded poor dispersion and poor MVTR. The incorporation of glass flake having an aspect ratio of 200, at 14% by weight loading decreased the MVTR by 55%, but severely compromised the EVA's adhesion to aluminum. The incorporation of 8% by weight of Glycidexx N-10 resulted in only a 9% reduction in the EVA's MVTR. The blending of LDPE, LLDPE, and HDPE with the EVA was pursued, as they are non-polar and, therefore, more hydrophobic, though they homogenized poorly with the Elvax 3185 due to the high melt index of the EVA and were subsequently discontinued. Other experimental efforts pursued increasing the crosslinkage density of the EVA, however, only modest reductions in EVA's MVTR were observed.

A latter series of experiments researched lower vinyl acetate containing EVA's. A 19% Vinyl Acetate containing EVA was measured to have a 20% lower MVTR than the Elvax 3185, and 15% Vinyl Acetate containing EVA had a 40% lower MVTR. Experiments were pursued with both EVAs where low density polyethylene (LDPE) or linear low-density polyethylene (LLDPE) at various melt indexes were blended into the EVAs. The formulations based upon the 15% Vinyl Acetate containing EVA blended with LDPE in various ratios provided the most promising results. As the LDPE content is increased, the MVTR decreases, though the adhesion to aluminum is compromised concurrently. To overcome the adhesion deficiency, further incorporation of additional primer was pursued, however, the approach proved ineffective at overcoming the substantially lower adhesive strength to aluminum versus the standard EVA formulations.

A further series of experimental formulations was prepared composed of EVA having various vinyl acetate contents blended with low-density polyethylene, and EVA vinyl silane grafts, and polyethylene vinyl silane copolymers. Measured MVTRs were reduced by as much as 10 fold versus the 15295P control, down to the range of 60-80 g/mil/24 hrs/100% RH/85°C/100 sq. inches, though the adhesion to aluminum was severely compromised for those best specimens. Those results are presented in Table 34.

Table 34:
Moisture Vapor Transmission Rates and Adhesion
Properties of Candidate Encapsulants

Formulation	Nominal MVTR	Adhesion to 15295P (lb./inch)	Adhesion to Aluminum (lb./inch)
15295P	900	NA	≥ 40
35504-A-3	170	30.1	2.9
35504-B-3	250	22.5	8.5
35504-C-1	140	11.2	10.1
35504-C-3	340	31.8	7.7
35504-D-3	330	30.5	5.4
35504-F-1	240	19.2	15.3
35504-G-2	260	25.9	4.4
35504-H-1	340	25.3	4.4
35504-I-2	80	20.5	0.2
35504-J-1	270	18.7	16.4
35504-J-1	250	18.7	16.4
35504-O-2	60	16.9	0.2
35504-P-2	300	20.4	10.3
35504-Q-2	170	22.5	2.5
35504-U	220	35.9	19.8
35504-W-2	380	19.3	13.7
35504-Y	140	20.3	12.3

Additional reformulation efforts were undertaken to improve the adhesion of the above-modified candidate encapsulants. A series of experiments were conducted using high boiling point plasticizers/carriers (having boiling points greater than 150°C) to aid in the incorporation of adhesion promoters into the encapsulant’s surface to promote improved adhesion. The following outlines those high boiler additives evaluated, along with a description of their relative absorption rate to the candidate encapsulant:

<u>Plasticizer/Carrier</u>	<u>Relative Absorption Rate</u>
FR-2 tris (dichloropropyl) phosphanate	very slow
p-cymene (isopropyl toluene)	fast
di (2-ethylhexyl) phthalate	slow
cyclohexanone	fairly fast
dimethyl methyl phosphanate	slow
Stoddard solvent	fast (least residue)

Unfortunately, the results failed to demonstrate any advantage of incorporating the adhesion promoters to the encapsulant in conjunction with high boiling point plasticizers. No gains in adhesive strength were measured.

3.5.3 Flame Retardant EVA

As more PV modules are used in residential rooftop applications, the need for a fire resistant PV module becomes more acute. For practical utilization in a PV module, an acceptable flame retardant encapsulation system has to maintain a high degree of optical clarity in the encapsulant layer above the solar cells, while

the layer behind the solar cells could be opaque. Formulation considerations are that the additives cannot have detrimental effects on the PV modules' performance and longevity.

Literature Review

From a chemical property perspective, EVA or ethylene vinyl acetate copolymers are more difficult to flame retard than are polyethylenes. At temperatures exceeding 200°C the EVA encapsulant volatilizes acetic acid, which is flammable and contributes dramatically to burning during combustion. STR's 15295P "fast-cure" encapsulant can volatilize up to 23% by weight acetic acid at temperatures below 300°C, based upon its vinyl acetate content of 32 percent.

The most common flame retardant additives, aromatic halogens, do not react below 400°C and, therefore, would be ineffective in an EVA-based encapsulant. On the other hand, based upon data provided by Albemarle Corp., some aliphatic bromides and chlorides are reactive below 300°C as depicted in Table 35.

Table 35:
Flame Retardant Reactivity Temperatures

Albemarle Corp. Product	BCL-462 (°C)	BC-48 (°C)	HBCD (FR1206HT) (°C)	BC-56HS (°C)
1% weight loss	121	137	164	170
5% weight loss	151	167	224	213
50% weight loss	205	224	246	256
Melting point	72	103	186	190

Through laboratory compounding efforts, it was observed that both BCL-462 and BC-48 melt and disperse well in the EVA-based encapsulant. All of the Albemarle flame retardants cited are reactive in the temperature range where acetic acid is being vigorously released from the EVA. Based upon a thorough review of the literature and from interviews conducted with a number of commercial flame retardant manufacturers, it became apparent that no commercial flame-retardant additives were considered effective for high vinyl acetate containing EVA copolymers. Most commercial products were specific to the wire and cable industry, and were of little to no value for this PV application.

Common wire and cable practice is to incorporate large concentrations (>50% by weight) of magnesium hydroxide or zinc borate into the plastic. However, at a more reasonable loading of 20% by weight for this application, these flame retardants were virtually ineffective.

Stemming from the literature review, three commercial flame retardant systems were identified for possible incorporation into the superstrate EVA encapsulant layer. However, each of those flame retardant systems severely discolored the encapsulant during lamination and were subsequently abandoned.

Proposed Mechanisms to Flame Retard EVA and Preliminary Evaluations

The mechanisms by which flame retardants are proposed to work in high vinyl acetate containing EVAs are:

- Halogenated flame retardants release the halide as hydrogen bromide or chloride, which intercepts and converts hydroxyl free radicals into water (H₂O), preventing carbon monoxide (CO) from forming carbon dioxide (CO₂).

- The halogen compound or hydrogen halide is inert and envelops the burning zone, excluding oxygen from the air.
- The flame retardant additive is endothermic and releases water or volatilizes, absorbing energy.
- The utilization of a basic mineral (pH>8) that neutralizes the acetic acid, forming a less flammable salt.

If a basic mineral were incorporated into the EVA substrate layer, it may partially neutralize the acetic acid that will be released during the flame exposure. It may even act like a chromatographic column to slow passage of acetic acid, diffusing it into the less heated mass and lowering its temperature. Various minerals tested have yielded very different results. Magnesium hydroxide and calcium carbonate have captured the acetic acid, even caused cooling for a few minutes, but eventually burst into flame with vigorous burning. Zinc borate formulated into the EVA at a 20 percent loading demonstrated slight improvement in the EVA's flammability resistance. The addition of zinc oxide further improved the flammability resistance, whereas talc and mica had very little effect. Of all the inorganic flame retardant additives evaluated, the most advantageous additives for imparting flame retarding properties were fibrous wollastonite and very fine silica.

In addition to the inorganic flame retardant additives, STR also pursued a number of experiments based upon organic additive, to evaluate the potential for imparting flame retardant properties to the EVA encapsulants. From those laboratory evaluations, the best organic flame retardants identified were halogen based. Compared with halogenated organic flame retardants, those formulations composed of non-halogenated organic flame retardant systems were not effective. Formulated at up to 22 percent loadings the non-halogenated organic flame retardants were not effective at preventing combustion, whereas lesser amounts of halogenated flame retardants, specifically those that decompose between 150-200°C, were quite efficient by comparison.

A further consideration included the family of intrumescent flame retardants. A series of laboratory results indicated that these types of flame retardants appeared to offer the best advantage over all other alternatives evaluated. The plastics community has employed various types of chemical intrumescent systems as flame retardants for over 50 years. Their effectiveness is directly related to the amount of heat induced during decomposition of the polymeric/organic composition. The thermal decomposition causes the intrumescent system to foam, leading to the formation of a char layer held together by the polymeric composition acting as a binder. Foaming can be as much as 100 fold. The char layer acts as a physical boundary and insulates the composite from the heat source.

However, there are some concerns related to an intrumescent system's possible contribution towards electrical conductivity and corrosiveness. To evaluate these concerns, sample formulations containing 5, 10, 15, and 20 percent of intrumescent additives were dispersed into formulated EVA. Surface resistance was measured and ranged from 10^7 - 10^{10} ohms (semi-conductive to non-conductive); when immersed in room temperature water, the pH in water was measured at 3.2 initially and 3.1 after one week. Through addition of alkaline additives to the EVA, the pH can be returned to neutral or basic.

Role of the Backsheet During PV Module Combustion

Over the course of the preliminary laboratory evaluations, based upon simulated UL-94 flammability testing using mini module compositions, it was observed that the Tedlar backsheet might play a role in catalyzing the burning of the PV module. That hypothesized role is attributed to the high temperature at which the backsheet combusts. It is postulated that as the flame front impinges the front of the module, it causes the EVA to melt and/or burn away clearing the way for the flame to ignite the Tedlar. Once ignited, the module combustion temperature increases. The increased combustion temperature results in

more rapid deacetylation of the EVA causing the formation of fuming acetic acid, which is readily combustible.

Supporting this hypothesis, similar observations were made by substituting other polymeric films in place of the Tedlar backsheet. Those substituted films included polycarbonate, PET, ULTEM polyetherimide, polysulfone, polyarylate, polyimide, Nylon 4,6, polyphenylene sulfone and polyethylene. Originally, it was postulated that these high temperature films might help to reduce flammability of the PV module, though the opposite was actually observed. In all cases, the higher temperature films appeared to contribute towards vigorous burning as had been observed with a Tedlar backsheet.

Experimental Flame Retarding Efforts

The intention of the laboratory efforts was to develop a flame retardant EVA encapsulant that could be utilized as part of an encapsulant system to help render a PV module more fireproof, i.e., improving the PV module's flammability resistance from a UL 1703 Class C level to a Class B or A level. It was envisioned that the newly formulated encapsulant would replace the EVA layer in a PV module situated behind the solar cells so as not to interfere with or block any of the light transmitted to the cells. The flame retardant EVA layer would have substantial enough flammability resistance to overcome the lack of flammability resistance of the superstrate EVA layer, thus preventing the flame front from penetrating through the back of the module and reaching substructures below the module. Based upon the information uncovered by STR during the literature search, a number of experimental flame resistant opaque EVA-based formulations were conceived.

To ensure repeatability, testing of each formulation was subsequently based upon a flammability test method modeled after 16 CFR Part 1610, The Flammability of Clothing, Textiles. Initial test specimens consisted of laminates comprised of transparent commercial EVA/flame-retardant EVA/5 mil Craneglas 230. Exposure was by direct butane flame-impingement at 1,895°C to the transparent superstrate EVA surface for 15 minutes. Observations were keyed upon the burning and/or dripping characteristics of the encapsulant.

Later test specimens more closely simulated actual PV module construction, composed of superstrate glass/EVA/cells/EVA/substrate film. Fifteen-minute resistance to combustion was accomplished utilizing non-FR EVA as the front EVA layer, with newly formulated candidate FR EVA as the back EVA encapsulant layer.

Although there were concerns related to the utilization of intrumescent additives as part of the additive scheme for flame retarding the EVA encapsulant (as the intrumescent additive's pH is 3.1 and its electrical resistivity is 10^9 ohms), STR's objective was to formulate the EVA in a manner resulting in a non-corrosive, insulating encapsulant. The ensuing laboratory formulation efforts yielded a basis of formulating flame resistant EVA-based encapsulants, which had pH's in the range of 9.3 (after one week's immersion in water), surface resistivities in the range of 10^{12} ohms/cm and volume resistivities in the range of 10^{13} . Upon flame impingement, this formulation resisted combustion for as long as 15 minutes, passing the initial laboratory qualification criteria.

Based upon the above findings, STR concluded that the inclusion of chemical intrumescent systems incorporated into EVA that is modified via additional flame retardant strategies, offer the most effective means for improving the flammability resistance of a PV module. A number of formulation variables based upon this strategy were pursued to examine the affects of varying the inorganic filler and flame retardant additive concentrations, the EVA base material's vinyl acetate content, and melt viscosity on achieving enhanced flammability resistance in a PV module. One of the deficiencies noted with the flame retardant system, was that the formulated EVA poorly cured during lamination. Cure was consistently

measured in the range of 50 percent, which is lower than the normally accepted target of 65 percent or greater.

Pilot Manufacture of the Flame Retardant EVA Encapsulant

Subsequent to the above experimental efforts, a single flame retardant EVA formulation, 34779-2A, was recommended for flammability testing in full size PV modules at BP Solar. A pilot run of 34779-2A encapsulant was processed. Product was manufactured in configurations of 18 mil encapsulant laminated to 5 mil Craneglas scrim and as 28 mil encapsulant without scrim. Representative sample rolls of the 34779-2A formulation were forwarded to BP Solar for incorporation as the back encapsulant layer in MSX-60 PV modules for flammability testing. A total of 5 MSX-60 PV modules were manufactured as presented in Table 36, based upon BP Solar’s standard production cycle time and platen temperature.

Table 36:
Description of the Prototype MSX-60 Fire Resistant PV Modules

Module #	Substrate EVA Composition	Backsheet	Comments
1	Scrim/18 mil 34779-2A /Scrim	None	EVA stuck to the laminator’s release liner, though could be removed. EVA flowed over ribbon.
2	Scrim/18 mil 34779-2A /Scrim	White Tedlar	EVA flowed over ribbon
3	Scrim/18 mil 34779-2A /Scrim/18 mil EVA	White Tedlar	EVA flowed over ribbon.
4	Scrim/28 mil 34779-2A /Scrim	White Tedlar	EVA flowed over ribbon.
5	Scrim/28 mil 34779-2A /Scrim	White Tedlar	EVA flowed over ribbon.

PV Module Flammability Testing

BP Solar utilizing two of the above-prepared modules performed fire resistance testing based upon UL-1703. Fire exposure was performed on module # 2 and module # 4. The module constructed with Tedlar backsheet failed to meet the Class B rating requirements, while a module with Craneglas 230 substituted for Tedlar backsheet met the Class B criteria. Further characterization was not pursued for that flame retardant system due to its low cure level, as the module was expected to fail subsequent testing, i.e., thermal cycling.

Reformulation Efforts to Overcome Cure Inhibition and Improve Flame Resistance

Gel testing of the 34779-2A flame retardant EVA-based encapsulant and variations thereof, indicated that maximum attainable cure levels were only in the 50 percent range, presumably due to cure inhibition caused by the flame retardant additives employed.

Further formulation optimization and characterization proceeded at the laboratory level, with positive results acquired in regard to the degree of cure. Reformulation efforts yielded formulation X33579P-FR which following lamination had measured gel contents in the range of 80 percent and 90 percent based upon 6 and 8-minute lamination cycles respectively. Laboratory flame testing demonstrated further improved resistance to combustion upon direct flame impingement exceeding 2 hours, without evidence of encapsulant dripping, flame spread or smoke generation. Formulation X33579-FR is nearly halogen free, containing only 0.7 percent halogen by weight, with the flame retardant additives comprising only 15 percent of the total module composition. The surface resistivity of the flame retardant encapsulant layer measured at 1.44×10^{12} ohms/cm and is, therefore, characterized as an insulator.

Pilot Manufacture and Testing of the Reformulated Flame Retardant EVA Encapsulant

The X33579-FR flame retardant EVA formulation was processed through STR's extrusion line into encapsulant. BP Solar produced test modules with Superstrate glass/15295P EVA/Cell Strings/Craneglas 230/FR EVA/Craneglas 230. Flame testing of a MSX-60 PV module containing X33579P-FR EVA as the substrate EVA layer resulted in a failure with the flame retardant EVA layer collapsing away from the module allowing the flame front to penetrate to the simulated roof structure. While the flame retardant EVA layer is resistant to burning, it is apparently not structurally strong enough to overcome the internal gas pressure developed within the module during module flame exposure.

Flammability testing of the flame retardant EVA layer demonstrated that the EVA is strongly resistant to combustion. It is doubtful that the flammability resistance can be further improved upon. Therefore, further module testing and qualification should focus on lending structural support to the substrate EVA layer to prevent collapse or failure of the EVA.

Investigation of Improving the Structural Integrity of a Flame Resistant PV Module

Substantial efforts were devoted towards investigation for appropriate substrate materials for attachment to the flame retardant substrate EVA layer in a flame retardant PV module. The following describes the results of screening those candidate substrate materials.

A series of candidate materials were evaluated for possible incorporation (lamination) to the back surface of a PV module that is constructed using the X33579FR experimental flame retardant EVA-based encapsulant. Qualification of each system was accomplished utilizing the flame exposure apparatus from 16 CFR Part 1610, The Flammability of Clothing, Textiles, where the test specimen is held at a 45° angle to a butane flame (1,895°C) source. The materials were evaluated for resistance to burn through or combustion. The results are presented in Table 37.

Table 37:
Flammability Resistance of Various Candidate Substrates

Candidate Substrate	Burn Through or Combustion Time
Craneglas 230 (5 mils)	< 10 seconds
Nomex Paper (2 mils)	< 10 seconds
Nomex Paper (3 mils)	<20 seconds
Fiberfrax (20 mils)	>> 10 minutes (badly weakened)
JM 8440 glass matte (13 mils)	< 10 seconds
JM 5018 glass matte (26 mils)	~120 seconds
Mutual Industries 7781 glass matte (6 mils)	>> 10 minutes
SAM 20 (Coarse glass fibers ¾ oz.)	> 10 minutes

It was obvious during testing that the organic binder contained on the Craneglas 230 scrim material is highly flammable and, therefore, performed poorly. Although three of the above materials were resistant to burn through or combustion for greater than 10 minutes, through observations gleaned during testing, it was concluded that the Mutual Industries 7781 glass matte offered the greatest advantage for lamination to the FR EVA encapsulant. The organic binder system employed by the Fiberfrax product burnt away during testing, and although the glass matte prevented burn through, the product was severely weakened and is prone to failure in a PV module. The SAM 20 product was discounted as it consisted of coarse long fibers that would prove difficult to work with during module fabrication.

To further qualify the Mutual Industries (MI) 7781 as a possible backing candidate in conjunction with the X33579FR flame retardant, a determination of compatibility through adhesive strength was pursued. Sandwiched compositions consisting of MI 7781/X33579FR/MI 7781 were laminated and cured. The composition was then evaluated for adhesive strength by performance of a 180° peel test. The adhesive strength was measured to exceed 20 pounds per inch peel strength, suggesting good compatibility.

Further flammability testing revealed that the combination of the 7781 glass scrim and an aluminum foil back layer resists the fire and hot gases generated by a butane flame for 15 minutes.

Surprisingly, it was later determined that a 0.5 mil. aluminum foil alone was resistant to flame penetration for up to 15 minutes. This was contrary to what had been anticipated as the butane flame temperature is nearly 3X greater than the melting point of aluminum (660°C). The ability of the aluminum to resist flame penetration may be attributed to:

1. the generation of a thin layer of aluminum oxide upon flame exposure, whereas the aluminum oxide's melting point is greater than 2000°C, and/or
2. the heat was rapidly conducted away from the flame impingement site, thus, never reaching the melting point of the aluminum.

In addition, a 12-mil PVC copolymer film, designated as PolyOne, was tested for its flammability resistance. The PVC film charred but resisted combustion throughout the direct flame impingement exposure; a further advantage is its low-cost.

3.5.4 Cure Monitoring

EVA cannot provide the required mechanical strength and sufficient heat resistance if it is not properly crosslinked. Crosslinking also improves the moisture barrier properties of EVA. Therefore, the degree of crosslinking achieved during the lamination process is an important quality control parameter and should be closely monitored, in real time if possible.

In practice, the degree of crosslinking is not or is only loosely monitored due to technical difficulties. The gel content of the EVA can be measured, but this takes a long time partially because the analysis itself needs 48 hour to complete. The late results cannot meet the need for timely process control. It is important to devise a procedure that is capable of obtaining a measure of the degree of crosslinking in nearly real-time fashion.

The degree of crosslinking is a function of temperature and time. EVA starts to crosslink when it is heated to an elevated (cure) temperature. The higher the temperature is, the faster EVA cures. The degree of cure achieved for EVA inside a particular module during a lamination cycle depends greatly on what temperature the EVA actually reaches and how long the module stays at that temperature. Unfortunately, manufacture the process is not flexible enough to accommodate the differences. The lamination cycle is pre-set and normally is not modified for a particular module. EVA in any two modules, especially those of different sizes, may experience very different temperature history of what temperature it actually reaches and how long it stays at a particular temperature. These issues only get worse for faster cure EVA as the total time decreases the actual module temperature becomes even more critical.

Two different approaches are being investigated to provide rapid feedback on the adequacy of the EVA cure process. The two methods under evaluation are tensile strength and Nuclear Magnetic Resonance (NMR).

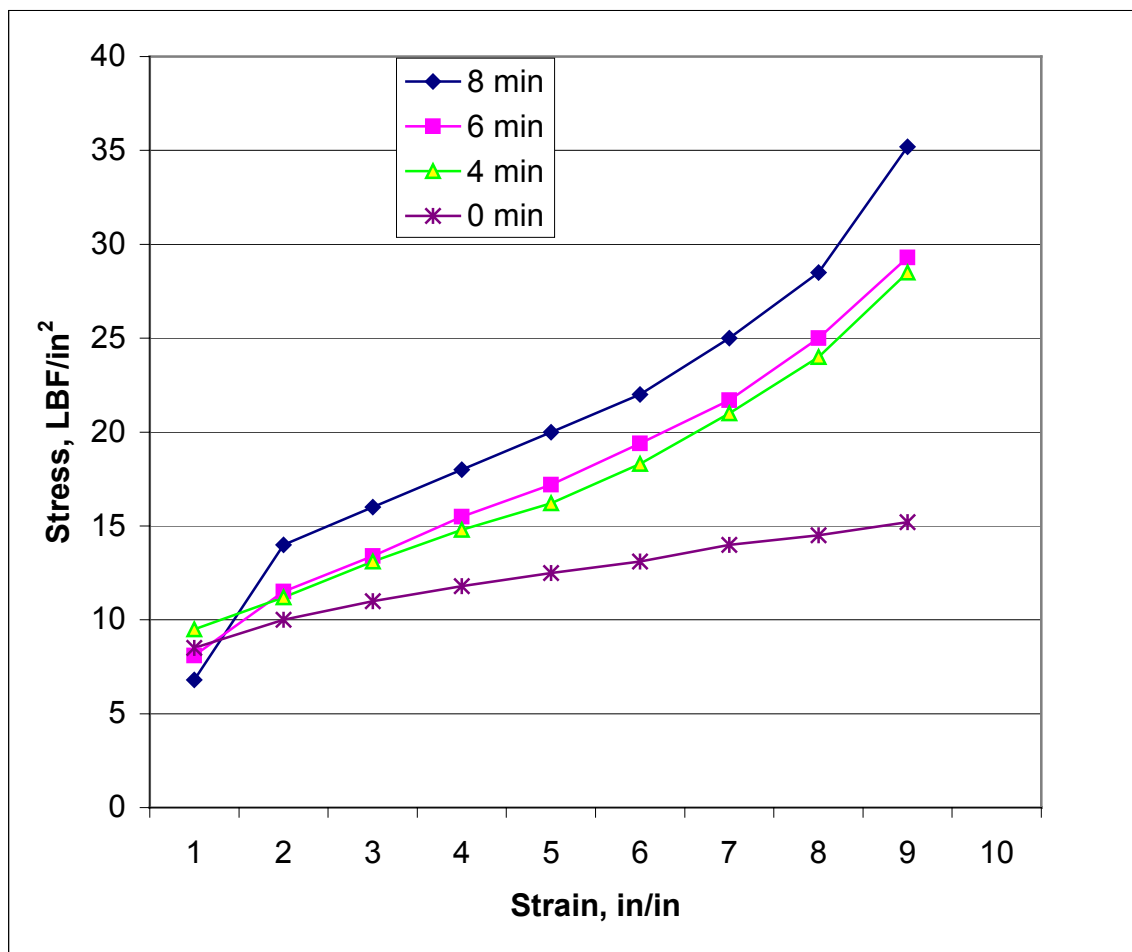
Tensile Test

Tensile tests are widely used to study thermosetting polymers and composites. Tensile strength increases and elongation at break decreases when the degree of crosslink increases.

Tensile tests must use free standing films. Samples were prepared with no glass or cells. All samples were processed in the same laminator with the same heat up time under vacuum. Each was then cured at the standard temperature and pressure for different lengths of time from 0 to 8 minutes.

These samples of EVA film with different crosslink density were cut into the appropriate size to be tested on our Instron machine. Figure 25 shows the stress–strain plots. The height of the stress–strain curve is related to the length of time cured, thus to the degree of crosslink, i.e., the gel content. The longer the cure time, the longer the crosslink time, and so the higher the curve's height.

Figure 25: Stress – strain curve of EVA films with different degrees of crosslinking. Samples were cured for 0, 4, 6 and 8 min after 4 minutes of heat up in vacuum



In practice, a master graph can be generated for a particular type of EVA. The master graph includes stress-strain curves of EVA of different crosslink density. Gel content measurements will be used to obtain the crosslink density for each individual sample. A free EVA film can be prepared with the procedure outlined above side by side with a module during the lamination process. The film will be tested to obtain a stress-strain curve. Overlaying this curve onto the master graph will yield gel content or crosslink density.

Nuclear Magnetic Resonance

Nuclear Magnetic Resonance Crosslink Density Spectrometer is a new low cost tool for very fast, accurate and automatic crosslink density measurements of rubbers, elastomers and other polymer networks. Samples of polymer to be studied need no sample modification or chemical treatment. Samples are placed directly in the equipment and a reading of bond density is provided within a few minutes.

Seven EVA samples (A - G) were fabricated and analyzed using NMR. The seven samples were cured for 6 (D), 8 (E), 10 (B), 12 (A), 14 (C) and 16 (F) minutes (each had the same standard heat up under vacuum). The results are shown in Table 38. According to the NMR results, using the Chemical crosslink density (Chem-XLD), there is no obvious chemical crosslink in unprocessed samples. The NMR data indicates increasing crosslinking with increased time at temperature as we would expect. A repeat of the 12 minute data resulted in almost identical results.

Table 38:
NMR measurements of EVA film crosslinking density

Cure time, min	0	6	8	10	12	14	16
Chem-XLD	0	0.8	2.26	5.48	8.20	8.58	12.1

Most NMR measurements of crosslink density have been performed on rubbery materials. This is the first time it has been applied to measure EVA samples. The initial analysis of EVA samples indicated that measuring temperature condition has a great effect on data accuracy. Rubber has a transition temperature (T_g) around -100°C or lower and its NMR measurements are conducted at room temperature. On the other hand, the T_g of the EVA encapsulant is in the range of -20 to -40 °C, much higher than that of rubber. No meaningful result was obtained when the measurement for EVA was performed at room temperature. Therefore, a heating cell was installed to the instrument so the EVA sample can be measured at elevated temperature (80 – 100 °C). The results shown in Table 38 are at 80 °C. The instrument is being conditioned for more precise temperature control and to determine the optimum measurement temperature for EVA.

The main advantages of NMR analysis are its minimum sample preparation requirement and the capability of obtaining crosslinking information in minutes. A rice grain size sample will be sufficient for NMR analysis and the sample need not to be in any regular shape. Normally a measurement takes between 5 to 8 minutes.

3.6 Handling

In this effort BP Solar was to develop improved product and materials handling techniques (including efforts in at least 3 separate areas) to increase line yield by 3% and reduce handling labor to save \$0.05/watt. BP Solar was supported in this task ARRI.

3.6.1 Assembly Automation

The first handling project selected was the development of a fully automated module assembly line. Besides the obvious advantages of automating the process to reduce labor, this line was designed for production of larger modules, up to 240 watts in size, and to minimize the rework and yield losses.

This line is now fully operational. Individual operators handle modules with vacuum lifts, roller tables and flip tables. Modules up to 45 inches (1.14 m) by 75 inches (1.9 m) with weights up to 75 pounds can be produced on this line. Modules are stacked in automatic buffers to avoid damage caused by direct stacking of modules.

The line consists of the following components.

- Glass handling system (See Figure 26)
- Cell tabber (See Figure 27)
- Cell stringing and lay-up equipment (See Figure 28)
- Transport, inspection and lay-up buffer (See Figure 29)
- Automatic load-unload laminator (See Figure 30)
- Transport, rotary table for trimming and light inspection table (See Figure 31)
- Framing system (See Figures 32 and 33)
- Vacuum lift (See Figure 34)
- Inverted solar simulator (See Figure 34)
- Module flip for inspection (See Figure 35)
- Boxing (See Figure 36)

The new line has dramatically reduced the requirements for rework with the number of rejects being reduced by 85%.

Figure 26
Glass Handling Vacuum Pickup



Figure 27:
Cell Tabbing Machine



Figure 28:
Cell Stringing Machine



Figure 29:
Transport, Inspection Table and Lay-up Buffer



Figure 30:
Automatic Load-Unload Laminator



Figure 31:
Transport Tables, Rotary Table for trim and Flip Table for Inspection



Figure 32
Framing Magazine and Butyl Pump



Figure 33:
Automatic Framing Table



Figure 34:
Vacuum Module Lift and Solar Simulator



Figure 35:
Flip Table for Final Inspection



Figure 36:
Boxing System



3.6.2 Ceramic Handling

As the ceramic pieces get larger and larger, removing them from the molds becomes more difficult. This is particularly an issue for the new single piece crucible. BP Solar engineering developed a method of removing the crucibles using an inflatable bladder inside of the piece. ARRI utilized this concept to design a fixture for removing crucibles from their molds and placing them onto a drying table.

Various techniques for removing the ceramic crucibles from the molds were studied. Raising and transporting the crucibles using the interior walls appeared to be a feasible approach. The first design approach was to utilize industrial grade inflatable deep-sea lifting bags, customized to meet the requirements necessary for lifting/transporting the ceramic crucibles. The bags are vulcanized in a dry heat autoclave to achieve high strength and durability. Such a unit was procured and tested as reported last year. It was difficult to insert even the smallest unit into the crucible, even while in a deflated state because of the large amount of friction between the neoprene bag material and the inside surface of the crucible. However, once the bag was in place inside the crucible and inflated to approximately 2.5 psi, the crucible could be securely lifted without any difficulties.

It was later found that the simplest and most cost effective method of improving the insertion procedure was to weight the bottom of the airlift bag. This causes the bag to be elongated into a conical shape, which can easily be lowered into the crucible and then inflated.

This handling system was not put into manufacturing, largely because the operators were more comfortable handling the pieces manually. The technique is available for use on larger, later-generation casting stations, where manual handling will no longer be an option.

Slip Dispensing

The focus of this task thus far has been to locate a dispensing system that will meet the need to dispense the slip material for making the grinding balls, lids and spouts. The single most significant dispensing process parameter is fluid viscosity. Viscosity is the proportionality constant relating the speed differential between fluid layers along the direction of flow and the resulting shearing force; it is a measure of resistance to flow. Table 39 illustrates viscosity values for a few common reference fluids:

Table 39:
Viscosity of Common Liquids

Reference liquid	Viscosity at 70°C (centipoise)
Water	1.00
Kerosene	3
Hydraulic oil	43
SAE 50 oil	1,100
Molasses	10,800
UV adhesives	60,000
Epoxies	>200,000
Pastes	up to ∞ (no flow)

Equipment is available to handle fluids in the million-centipoise range. The primary effects of increased viscosity, from the perspective of the type of equipment used, is the need to utilize higher pressures and larger orifices to push the fluid, and the potential need for a so-called snuff-back valve or vacuum pull method to avoid *stringing* (and thereby achieve a clean cut-off of the fluid stream). Although UV cured

adhesives vary in viscosity depending on the specific formulation, they can be collectively categorized in the medium or moderate viscosity range.

A second key dispensing process parameter is the shot size, which, combined with the net volume of liquid to be dispensed per appropriate time interval (units assembled, hour, shift, day, week), determines whether to use disposable syringe-style barrels or a continuous feed from a reservoir. Equipment exists in both of these configurations to handle volumes from nanoliters to liters. UV cure adhesive dispensing requirements will vary depending upon the application; syringe-style equipment is available to perform high-precision dispensing for small dot applications, while high production rates or high delivery volume patterns (lines and surfaces) must be served by continuous-feed systems.

Fluid viscosity and shot size are the most important of a long list of factors that influence the choice of a dispensing system. Collectively, such parameters may be classified as being related to the fluid characteristics or the manner in which it is to be delivered, as reflected in the list below:

Fluid-related parameters

- Physical characteristics:
 - ⇒ Viscosity.
 - ⇒ Type (e.g., liquid, gel, suspension, paste...).
 - ⇒ Density or specific gravity.
 - ⇒ Pot life.
- Is substance tacky or stringy?
- Is viscosity readily affected by heat (e.g., will product flow considerably faster if temperature rises by 10-20 F)?
- Is heating required for proper delivery? What temperature?
- Is agitating required to prevent settling of pigments or suspended solids?
- Is fluid moisture sensitive?
- Must solvent be applied at regular intervals to prevent the substance from “skinning over”?
- Is vacuum degassing required?
- Is fluid corrosive or abrasive?
- Is mixing of two or more components required (e.g., two-part epoxy)?

Delivery-related parameters

- Shot size (cc.)
- Dispense rate (cc/sec.)
- Cycle time (sec.)
- Syringe/reservoir size (cc.)
- Bead application:
 - ⇒ Length (mm.)
 - ⇒ Diameter (mm.)
 - ⇒ Pattern (dot, line, square, circle...)
- Receiving surface geometry (open vs. cavities or bores.)
- Needle gauge or diameter (mm.)
- Reproducibility required (shot-to-shot, stated in +/- % of volume dispensed.)
- How many shots at one time (parallel stations)?
- Is there required post-processing (curing)?

UV cured adhesives are single-part fluids whose curing times are dramatically reduced when exposed to UV light (in the seconds to tens of seconds range.) They usually do not require heating during their

application, and are of stable, yet moderate viscosity which can lead to stringing. They are slightly denser than water (≈ 1.2 specific gravity). Because some formulations also cure in the presence of visible range, the containers and feed lines must be made of opaque materials. In (*non-UV*) light of the fact that curing is required, consideration must be given to integrating the dispensing equipment with a suitable UV source.

There are challenges intrinsic to dispensing. Aside from the parameters previously discussed, there are also application-dependent factors that may influence the specific equipment choice:

- Bubble formation and cavitation; this occurs if the material is being aspirated into a chamber with sufficient force to cause it to separate (typical of high-viscosity fluids and pastes.)
- Incompatibility with dispensing equipment material; clogging.
- Exact measurement of liquid dispensed (mass flow) and process verification.
- Abrasive/corrosive materials requiring stainless steel equipment or special valving which uses pneumatic rather than mechanical contact methods.
- Fluid reservoir size and type, refill interval.
- General maintenance: dry air for pneumatic systems, periodic cleaning of wetted components, etc.
- Conflicting parameters: higher pressures and shorter cycle times lead to increased throughput but decrease accuracy and repeatability and require more expensive equipment (high-performance seals.)

Dispensing Equipment Classification

A breakdown of current-day state-of-the-art dispensing equipment by the type of technology used was generated. Table 40 contains a summary list of the categories identified.

Table 40:
Dispensing Equipment Classification

Time/Pressure	Positive Displacement
Timed-air pulse syringe (varimeter) Dispense (metering) valve	Collapsing tube valve Reciprocating piston Rotary valve Positive displacement syringe Peristaltic pump Valve less (progressive cavity) pump

As shown, a logical technology division exists between time/pressure and positive displacement devices. Time/pressure systems rely on the adjustment of fluid pressure and valve open time to allow the passage of fluid, while positive displacement devices rely on the stroke adjustment of a particular mechanism. The typical tradeoff is initial cost / low maintenance / disposability for the former, versus accuracy / repeatability for the latter.

For the BP Solar application a Peristaltic Pump was been selected to dispense the slip material.

- Principle: eccentric rotor presses against a pinch tube, creating a vacuum to pull the fluid from the reservoir and pushing it out at the same time.
- Operator unit allows setting the pump speed and cycle time.
- Small shot sizes possible (down to 0.0006 cc.)

- Advantages:
 - ⇒ High precision, user-friendly operation.
 - ⇒ Self-priming; can retrieve fluid directly from container (no syringe.)
 - ⇒ Wetted components easily replaced.
 - ⇒ Pump can be operated in reverse to return the fluid in the line back to the reservoir.
- Disadvantages:

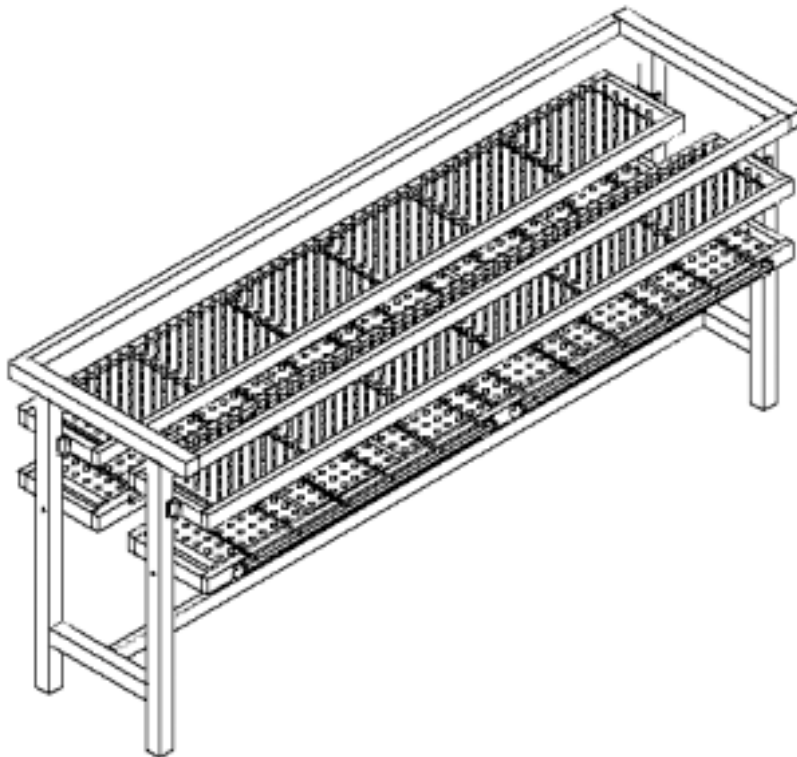
Motor unit adds level of complication and lowers reliability.

ARRI tested this dispensing system with BP Solar slip. From these tests they were able to determine the appropriate dispense rates. The prototype system offers the following features.

- Easy set up and cleaning
- Dispensing rates comparable to current method to dispense balls
- Elimination of the need to carry buckets of slip for lid dispensing process
- Consistent flow rate
- Minimum parts, tube and fittings, come in contact with the slip
- Low cost

Tests of this slip pumping method were satisfactory. ARRI then developed three potential system configurations for improving the slip dispense process. It was agreed to proceed with an enhanced manual method that uses a peristaltic pump and a rack layout that diminishes floor space requirements and is able to shrink current production requirements into a single shift operation. (See Figure 37)

Figure 37:
Ball Mold Rack



The completed rack holds two rows of six ball molds. Each row has an upper and lower tray for supporting the upper and lower ball mold halves, respectively. Once the molds are loaded into the trays, the trays are clamped to firmly secure the molds. The operator performs the slip dispensing process in the standing position using the peristaltic pump. Once the drying process is completed, the operator raises the tray supporting the upper mold halves with a manually operated winch. For convenient unloading of the balls, the tray containing the lower ball mold halves rotate 180° on a central axis, allowing the balls to drop into a catcher bin. The operator sits on a mobile cart and move along the side of the rack to remove any balls that stick in the lower ball molds.

The completed rack was delivered by ARRI to BP Solar for testing.

A study of milling ball formation within the mold was also undertaken in order to increase the density of the cast piece and increase the uniformity and working life of the milling balls.

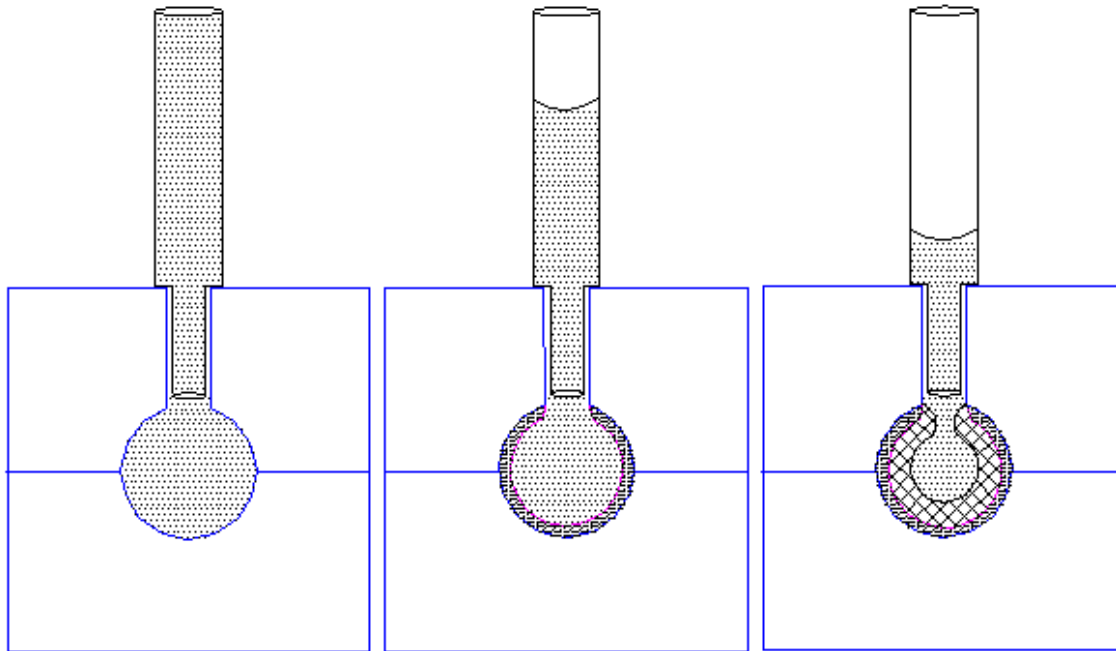
The presence of a central air pocket in the cast milling balls causes them to break up and wear out quicker during mill use. In order to understand the cause of the formation of air cavities within balls, the behavior of the slip during the mold filling process was studied. As the drying process begins, moisture is drawn out of the slip through the walls of the ball mold cavity. In the initial stages, the solidifying slip adheres to the inner walls of the ball mold cavity, forming a thin-walled sphere (Fig. 38(a)). As the drying process progresses, the solidifying slip begins to adhere to the previously solidified slip, and the wall thickness of the sphere increases (Fig. 38(b)). As the slip continues to adhere to itself, a problem begins to develop at the upper fill opening of the ball mold cavity (Fig. 38(c)). The solidifying slip eventually closes off the upper opening of the sphere, trapping a *fixed volume of liquid slip* in the center of the ball (Fig. 38(d)). As the liquid slip loses moisture through the solidified layers and into the mold, an air pocket is caused by the decrease in volume of the trapped slip (Fig. 38(e)).

ARRI considered alternative methods for resolving this problem that would allow the solidification pattern of the slip to be controlled, while still maintaining the spherical shape of the grinding balls. These involved either slightly modifying the mold geometry, or making a minor adjustment to the dimensions of the fill tubes. Since modifying the fill tubes was the least disruptive to the slip dispensing process, this approach was tested first.

ARRI modified several fill tubes so the fill neck extends into the ball cavity by 0.5 cm. A slight improvement in the grinding ball formation was observed. The grinding balls formed using the fill tube with the extended neck showed a significant reduction in the volume of trapped air. However, while the large air pocket was been reduced to a cluster of star-shaped pores, it was believed that rapid break-up during the mill process would still occur. In an attempt to completely eliminate the presence of any air pockets, the upper half of the ball mold was coated with latex. Thus, drying could occur only through the lower mold half. This would force the solidification process to occur from the bottom upward rather than radially. The resulting grinding balls were completely solid, exhibiting no air pockets or pores

Figure 38:

Stages that occur during the ball drying process, illustrating the formation of a grinding ball and possible development of an air pocket. (Dots~liquid slip, Hatches~solidified layers, Blank~air pocket)



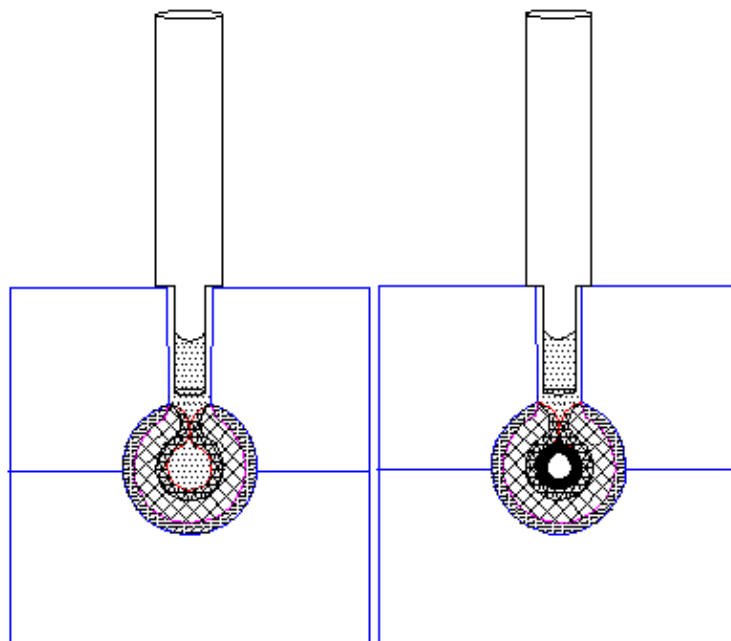
(a)

(b)

(c)

(d)

(e)



3.6.3 Handling in Casting

This task has been broken down into two parts. The first part involved a BP Solar redesign of the casting station to allow for automatic ingot unloading of the station. This task was begun during the first year, with a prototype unit designed and built by an outside vendor. This unit was installed and tested during year two of the program. Modified versions of the prototype were then installed on the new quad described in Section 3.2.1. Photographs of the new handling system are shown in Figures 39 and 40.

Figure 39:
New Ingot Loading Cart – Extended



Figure 40:
New Ingot Loading Cart – In Place



3.6.4 Handling in Cell Line

See discussion of “fast-cure ink” in Section 3.4.4 above. The rotary printer, which is enabled by the fast-cure process results in improved yield and process reliability by eliminating the need to move and dry the cells between the two back-print processes.

3.7 Measurement and Control

In this task BP Solar developed process measurement and control procedures for use on the production line (including efforts in at least 3 separate areas) to improve yield by 3% and reduce rework by 50%. In order to improve process measurement and control in the production line and reduce rework BP Solar, with support from a lower-tier subcontract with ARRI, has implemented an improved information system, performed a factory measurement and control survey to determine what areas require improvement and selected 3 measurement and control projects that were implemented during the program.

3.7.1 Brick ID System

One approach to improve data collection would be to mark and track each wafer. Our plan was to develop a process whereby the face of every silicon brick is marked before wafering. Hopefully, these marks would be readable on the wafers all the way into the finished product and identify the brick from which each wafer came and its position within the brick. In the first year of the program, we found a vendor, who was able to scribe very shallow but easily sensed troughs along the brick edge. The bricks were then wafered without yield problems and run through the cell line. Cell line yields were acceptable. However, the scalloped edges of the trough were visible in finished laminates and were not thought to be cosmetically acceptable. This work was halted as having a low probability of success.

3.7.2 Doping and Diffusion Measurements / MES

There was consensus of the BP Solar engineering staff that diffusion was the most important place to begin improved measurement and control. A prototype measurement and control system for the diffusion area was proposed. ARRI identified the sensors, computer hardware and software necessary for such a unit.

In the first contract year, ARRI assembled a prototype unit with sensor interface modules for thermocouples, frequency counters and generic RS-232 interfacing (such as digital scales, bar code readers, digital voltmeters, etc.). A major issue involved the wafer sensor selection and placement for counting. ARRI identified a potential source that eventually resulted in procurement of a sensor that could identify and therefore count silicon wafers.

A prototype system was partially deployed in Year 2. Hardware was installed on the line, and a preliminary operator interface was set up. At that point the deployment was stopped due to uncertainty about how to interface the system with the rapidly evolving internal computer network, the specifications of which were likely to change because of the information systems requirements of our new parent company.

Instead of tackling this problem at the single node of diffusion, a generic approach was taken. This resulted in the deployment of a plant-wide, prototype manufacturing execution system (MES). The system is in the form of an intranet web site, collecting data from a number of nodes around the Frederick factory. The web site was completed in late 2001 and is now being expanded to include the Sydney and the Bangalore factories.

The web site offers a great deal of real-time information. It is accessible from any computer on the global BP network. Because an Internet Browser is the only software needed to view the site, cost is kept down while providing all users with the same data presented in a consistent and easy to use form. Most of these pages are dynamic, automatically updated with the most recent data each time the page is visited.

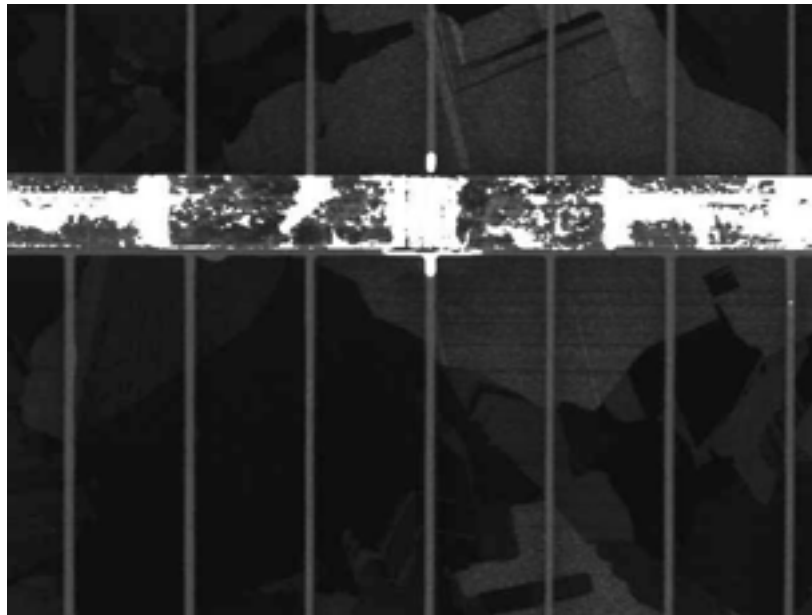
Pages exist for each area in the process. Information is available for Casting, Sizing, Wafering, Cleaning, and Cell Line, among others. The page for each area typically shows how much product was made at each process, what is the yield for each process and what are the yield losses. Most processes also show the Coefficient of Variation (CoV). Some of the pages allow viewing of specific information that is user selectable. For example, on the cell line page, the user can select a particular period of time, or a particular cell size or a particular cell line. Most pages present the information in tabular form, but many also allow the user to display the information in graph form.

3.7.3 Vision Inspection of Solder Tab

Uniformly reliable solder bonds between interconnect ribbon (“tabbing ribbon”), and the front and rear cell metallization, are critical to the long-term field reliability of PV modules. Present manufacturing practice relies on destructive testing of sample bonds to control the soldering process. This practice is expensive, and limited sampling runs the risk of missing potentially defective joints. ARRI and BP Solar began to look for a method by which the solder joints might be effectively 100% tested using a non-destructive method.

The first approach was to apply automated vision inspection of the tabs, looking for signatures characteristic of good or of unacceptable joints. It was determined that a vision system with standard vision tools was capable of measuring the amount of surface area where the solder had re-flowed along the tabbing ribbon (see Figure 41). The length of re-flow, or “met-back” of the solder is an indication that the ribbon received the correct amount of heat during the soldering process. This is true for top and bottom solder joints.

Figure 41:
Solder Reflow Inspection Using Vision System



However, additional testing showed many cells solder joint signatures that were not clearly discernible by machine vision, even after trials with several different structured lighting configurations.

The vision approach was subsequently dropped in favor of infrared sensing. This approach was itself dropped after the solder machine vendor proposed an improved soldering control development study. This was initiated under subcontract with ASCOR in mid-2001.

The goals of this subcontract included:

- Monitoring and documenting the consistency of the soldering process over time.
- Determining the optimum method and hardware to economically monitor the process (i.e. temperature, resistance, current, voltage, etc.).
- Determining if closing the loop is feasible, and what the associated costs and gains would be.
- Determining the impact on quality and/or cycle time provided by pre-heating the cell.
- Determining the ability of the system to handle different types of tabbing ribbon including, but not limited to plated and hot dipped ribbon.

ASCOR procured a high speed IR sensor along with the appropriate data collection hardware, and utilized these tools to provide a “benchmark” measurement of the process. A bench top ASCOR soldering controller was set up to run a typical soldering cycle and to collection data on the heat profile of the solder tip, along with both voltage and current. ASCOR is using this data to determine the repeatability of the system and how well the temperature correlates to voltage, current, and resistance. ASCOR hopes to use the results of this study to improve the uniformity and control of the solder joints that its production equipment makes.

Completion of this work is expected to lead to improved uniformity of solder joint strength from site to site on an individual cell, and also to improved performance over the life of each soldering tip.

In addition, work was done on the configuration of the existing solder tips. It was determined that a modified solder head, in which the tips were rotated with respect to their original position, was more robust with respect to variation in the cells being delivered to the process as well as being potentially easier to control. BP Solar manufactures both multi-crystalline and mono-crystalline cells, and this modification reduces the length of time required to changeover tabbing equipment from one type to the other.

3.7.4 Wafer Fracture Detection

Wafer breakage during processing is a very high cost issue. This is particularly true when wafers fail during one of the print steps, generally resulting in several minutes of downtime while the operator cleans up the scattered parts and the wet paste. This is also a source of potential contamination. It is believed that wafers frequently fail at the print steps, not because they come into the process already cracked and the crack then fails when it is stressed during the process step. ARRI and BP Solar are investigating methods for detecting and rejecting cracked wafers before they are processed.

Several potential methods and vendors were identified initially.

Eddy Current Testing

This company says they are using eddy currents successfully to detect micro cracks in wafers. Eddy current sensing is fast enough for on-line use and less costly than ultrasonic testing.

Laser-based Ultrasound

This method is based on using a short laser pulse directed at the wafer to cause a sudden rise in temperature of the wafer material. The temperature rise initiates a sudden but minor expansion of the

silicon. The acoustic energy released from the expansion can be used to distinguish between elastic or plastic expansion. The strain energy emitted from the cracks will produce acoustic waves having frequencies characteristic of plastic deformation.

The technique is fast enough so it can be implemented on-line, is a non-contact approach and can be described as "low-cost."

Samples of good and of damaged solar cells were submitted for eddy current testing. The supplier reported that wafers that have not yet been through the metallization process tend to yield better readings, however they went ahead with the testing. The metallization gave a signal of ~100,000. The silicon produced a response of ~1000 and a flaw response of ~10. Variations in the metallization will tend to swamp any flaw response. This method was subsequently dropped as not viable.

Cells were also sent to test the feasibility of using Laser Based Ultrasound (LBU). The vendor demonstrated that laser-based ultrasound inspection is a viable method for detection of micro-cracks in wafers. The inspection technique involves the use of two lasers. The first laser scans the wafer in 5-mm increments along the *x* and *y* directions to create localized heating of the wafer, which causes the targeted region to expand, emitting acoustic signals. The acoustic emission is measured by the second laser, which takes the place of contact sensors normally used in acoustic emission sensing.

Finally, an acoustic emissions-based crack detection approach was proposed by Lasson Technologies, and a prototype system jointly developed by Lasson and ARRI. A meeting was then held between BP Solar, ARRI and Lasson discuss which approach would be pursued of three feasible options available: (1) An independent portable micro-crack inspection station, (2) An in-line micro-crack inspection station designed for the tabbing station, or (3) An in-line micro-crack inspection station designed for the rotary screen printing station. Based on the material handling requirements and the cycle time associated with the acoustic emission (AE) inspection system being developed, the decision was made to develop the inspection station for the rotary screen printing station. This would require the shortest development time, and will allow BP Solar to quickly evaluate the performance of the AE system operating on-line. (If BP Solar is satisfied with the results, and are still interested in testing the wafers at different stages in the production line, ARRI/Lasson Technologies can then proceed with the development of a portable independent inspection station.)

Logic circuitry for the inspection system was completed. Testing was performed to ensure immunity to electromagnetic noise that can be encountered in a typical manufacturing environment. Packaging of the electronics and the sensor tip was also completed. A bench-top prototype handling system was developed by ARRI and the handling and sensing units were then mated at ARRI.

The performance of the prototype acoustic emission (AE) based inspection system was very reliable and proved to be repeatable over a series of tests conducted with a representative sample of wafers. From a mixed set of good and bad wafers, the system was able to easily detect the cracked wafers and deposit them in a designated reject bin. System speed was well within the requirement for integration into high-speed production equipment.

After the successful test of the system at ARRI, the system was "hardened" for use on a more production-like environment. The rebuilt unit was delivered to BP Solar in Frederick for large-scale testing. The unit was used in several tests on production wafers and cells.

One sample test was on completed cells after electrical test, the final step in cell production. A small percentage of completed cells fail electrical test due to low shunt resistance. Many of these failures are

thought to be caused by cells, that have been cracked prior to one of the metallization steps. When metal is printed over a crack, it causes a local shunt.

Four packages of accumulated shunt rejects were run through the prototype unit. The results are shown in Table 41. Physical inspection of the cells confirmed that they were, in most cases, actually cracked.

Table 41:
Test of Shunted Cells on Crack Detection System

Package	Number of cells that Pass Inspection	Number of cells that Fail Inspection	Percent Failed (%)
1	35	17	33
2	32	20	38
3	36	13	27
4	38	12	24

Tests were also conducted on other failure mechanisms, as well as on regular production wafers and cells. Although the results were generally good, the system produced some false positives and failed several test/retest cycles. This performance was very different from the earlier tests performed at ARRI in which the system was virtually flawless. Feedback from the testing at BP Solar will be utilized to further improve the performance of the crack detection system.

Ultimately, BP Solar plans on implementing the micro-crack inspection system into their production line in order to achieve 100% inspection of the wafers at various points, for example, tabbing, screen printing and diffusion.

REFERENCES

- ¹ J. H. Wohlgemuth, "Cast Polycrystalline Silicon Photovoltaic Module Manufacturing Technology Improvements" Final Subcontract Report, NREL/SR-520-26071 – June, 1999.
- ² J. H. Wohlgemuth, D. Whitehouse, T. Koval, J. Creager, F. Artiglieri, T. Tomlinson, J. Cliber, A. Buckman, M. Perry, S. Narayanan, S. Shea, M. Roy, G. Kelly, M. B. risson, R. Dominguez, and M. Conway, "Progress in BP Solar's Crystalline Silicon PVMaT Program, *Proceedings of 26th IEEE PV Specialist Conference*, p. 1055, 1997.
- ³ J. H. Wohlgemuth, "PVMaT Improvements in the BP Solar Photovoltaic Module Manufacturing Technology" First Annual Subcontract Report, NREL/SR – in press, 2000.
- ⁴ J. H. Wohlgemuth and S. P. Shea, "PVMaT Improvements in the BP Solar Photovoltaic Module Manufacturing Technology" Second Annual Subcontract Report, NREL/SR – in press, 2001.
- ⁵ J. H. Wohlgemuth, "Cast polycrystalline Silicon Photovoltaic Cell and Module Manufacturing Technology Improvements", *NCPV Photovoltaic Program Review*, AIP Conference Proceedings 462, p. 747, 1998.
- ⁶ J. H. Wohlgemuth, "Casting Polycrystalline Silicon for Photovoltaics", Proceedings of International Symposium-Workshop on Silicon Technology Development and Its Role in the Sun-Belt Countries, 14-18, June 1987, Islamabad, p. G-1.
- ⁷ R. Gehringer, "Method for hydrofluoric acid digestion of silica/alumina matrix material for the production of silicon tetrafluoride, Aluminum tetrafluoride and other residual metal fluorides and oxides", US Patent 5,242,670.
- ⁸ S. Narayanan and J. Wohlgemuth, "Cost-benefit analysis of High-efficiency Cast Polycrystalline Silicon Solar Cell Sequences", *Progress in Photovoltaics*, Vol. 2 No 2, p. 121, 1994.
- ⁹ T. Koval, "Vapor deposition of H₂PO₄ and formation of thin phosphorus layers on silicon substrates", US Patent 4,360,393, 1982.
- ¹⁰ S. Strehlke, D. Sarti, A. Krotkus, O. Polgar, M. Friend, J. P. Roger, C. Levy-Clement, "Porous silicon emitter and high efficiency multicrystalline silicon solar cells", **14th EC PVSEC**, 2480 (1997).
- ¹¹ S. DeWolf, P. Choulat, E. Vazsonyi, R. Einhaus, E. Van Kerschaver, K. De Clercq and J. Szlufcik, "Towards industrial applications of isotropic texturing for multi-crystalline silicon solar cells", **16th EC PVSEC**, pp. 1521 (2000).
- ¹² S. Winderbaum, O. Reinhold, F. Yun, "Reactive ion etching (RIE) as a method for texturing polycrystalline silicon solar cells", *Solar Energy Materials & Solar Cells* **46 (3)** pp. 239 (1997).
- ¹³ P. Fath and G. Wileke, "Polycrystalline silicon wafer engineering for photovoltaic applications", *Semicond. Sci. Technol.* **9**, 101 (1994).
- ¹⁴ H. Jansen, et al., *J. Micromech. Microeng.*, Vol. 5, 250 (1996).
- ¹⁵ A. R. Burgers, C. J. Tool, J. D. Hylton and A. W. Weeber, "Silicon solar cells textured by reactive ion etching and processed with screen printing", **2nd World Conf. PV Conversion**, 1531 (1998).
- ¹⁶ K. Shirasawa, F. Fukui, K. Okada, Y. Inomata, H. Takahashi, Y. Fukawa, and S. Fujii, "Over 17% large area multicrystalline silicon solar cells", **14th EC PVSEC**, pp. 384 (1997).
- ¹⁷ E. Yablonovitch, *J. Opt. Soc. Amer.* **72**, 899 (1982).

-
- ¹⁸ D.S. Ruby, Saleem H. Zaidi, and S. Narayanan, "Plasma-Texturization for multicrystalline silicon solar cells," *PVSC-28*, 75 (2000).
- ¹⁹ S. H. Zaidi, D. S. Ruby, and J. M. Gee, "Characterization of random reactive ion etched-textured silicon solar cells," *IEEE Trans. Elect. Dev.* **48**, 1200 (2001).
- ²⁰ Duerinckx, F., Szlufcik, J., Ziebakowski, A., Nijs, J., and Mertens, R. "Simple and efficient screen printing process for multicrystalline silicon solar cells based on firing through silicon nitride" *Proceedings of the 14th European PVSEC*, Barcelona, 1997.
- ²¹ Duerinck, F., Szlufcik, J., De Clercq, K., De Schepper, P., Laureys, W., Nijs, J., and mertens, R> "PECVD silicon nitride passivation and ARC layers for screenprinted multicrystalline silicon solar cells" *Proceedings of the 13th European PVSEC*, Nice, 1996.
- ²² Szlufcik, J., De Clercq, K., De Shepper, P>, Poortmans, J., Buczkowski, A., Nijs, J., and Mertens, R> "Improvement in multicrystalline silicon solar cells after thermal treatment of PECVD silicon nitride AR coating" *Proceedings of the 12th European PVSEC*, Amsterdam, 1994.
- ²³ Lucovsky, G., Wu, Y., Niimi, H., Misra, V., and Phillips, J.C. "Bonding constraints and defect formation at interfaces between crystalline silicon and advanced single layer" *Applied Physics Letters*, p. 2005, (1999).
- ²⁴ Nagoyoshi, Hiroshi, Ikeda, Makoto, Yamagushi, Misako, Uematsu, Tsuyoshi, Saitoh, Tadashi, Kamisako and Koichi "SiN_x:H/SiO₂ double-layer passivation with hydrogen-radical annealing for solar cells" *Journal of Applied Physics* Vol. 36, p. 5688,(1997).
- ²⁵ W. M. Bik, R. N. Linnsen, F. H. Habraken and W. F. van der Weg, "Diffuson in low pressure chemical vapour deposited silicon nitride films", *Applied Physics Letters*, **56**, p. 2530, (1990).
- ²⁶ H. J. Stein and H. A. Wegener, "Chemically bound hydrogen in CVD silicon nitride – dependence on ammonia to silane ratio and on annealing", *Journal of Electrochemical Society*, **124**, no. 6, p. 908, (1977).
- ²⁷ Holley, W., Agro, S., "Advanced EVA-Based Encapsulants" Final Report, NREL/SR-520-25295, September 1998
- ²⁸ Willis, P., JPL Contract 954527 Final Report , p. V-15 and V-32, 1996.

REPORT DOCUMENTATION PAGE			Form Approved OMB NO. 0704-0188	
Public reporting burden for this collection of information is estimated to average 1 hour per response, including the time for reviewing instructions, searching existing data sources, gathering and maintaining the data needed, and completing and reviewing the collection of information. Send comments regarding this burden estimate or any other aspect of this collection of information, including suggestions for reducing this burden, to Washington Headquarters Services, Directorate for Information Operations and Reports, 1215 Jefferson Davis Highway, Suite 1204, Arlington, VA 22202-4302, and to the Office of Management and Budget, Paperwork Reduction Project (0704-0188), Washington, DC 20503.				
1. AGENCY USE ONLY (Leave blank)	2. REPORT DATE April 2002	3. REPORT TYPE AND DATES COVERED Final Subcontract Report, 4 May 1998 – 30 November 2001		
4. TITLE AND SUBTITLE PVMaT Improvements in the BP Solar Photovoltaic Module Manufacturing Technology, Final Subcontract Report, 4 May 1998 – 30 November 2001			5. FUNDING NUMBERS CF: ZAX-8-17647-05 PVP26101	
6. AUTHOR(S) J. Wohlgemuth and S. Shea				
7. PERFORMING ORGANIZATION NAME(S) AND ADDRESS(ES) BP Solar 630 Solarex Court Frederick, Maryland 21701			8. PERFORMING ORGANIZATION REPORT NUMBER	
9. SPONSORING/MONITORING AGENCY NAME(S) AND ADDRESS(ES) National Renewable Energy Laboratory 1617 Cole Blvd. Golden, CO 80401-3393			10. SPONSORING/MONITORING AGENCY REPORT NUMBER NREL/SR-520-32066	
11. SUPPLEMENTARY NOTES NREL Technical Monitor: R.L. Mitchell				
12a. DISTRIBUTION/AVAILABILITY STATEMENT National Technical Information Service U.S. Department of Commerce 5285 Port Royal Road Springfield, VA 22161			12b. DISTRIBUTION CODE	
13. ABSTRACT (<i>Maximum 200 words</i>) This report describes the advancement of BP Solar PV manufacturing technologies in order to design and implement a process that produces polycrystalline silicon PV modules that can be sold profitably for \$2.00 per peak watt or less and that increases the production capacity of the Frederick plant to at least 25 megawatts per year. Achieving these major objectives was based on meeting the following specific task goals: (1) Develop a process to produce silicon feedstock from Na ₂ SiF ₆ that can be sold profitably for less than \$15/kilogram in large quantities. Demonstrate the process in a pilot facility. (2) Optimize and improve control of the casting process to increase the process yield by 7% and to improve material quality such that average cell efficiency increases by 4%. (3) Reduce the center-to-center cut distance on the wire saw to less than 450 μm in production, and develop a wire saw process that reduces the consumable costs by at least \$0.05/wafer, that does not require organic cleaners, nor result in generation of hazardous waste material. (4) Develop, demonstrate, and implement a cost-effective cell process that produces a minimum average cell efficiency of 15% and improves the cell line electrical yield by 5% when applied to BP Solar cast polycrystalline silicon wafers. (5) Develop and qualify an encapsulation system that meets all technical and reliability requirements and can be laminated and cured in less than 6 minutes. (6) Improve BP Solar's product and materials handling to increase line yield by 3% and reduce handling labor to save \$0.05/watt. (6) Improve process measurement and control in the production line to improve yield by 3% and reduce rework by 50%.				
SUBJECT TERMS: PV; polycrystalline silicon; solidification casting process; etched wafer; thick film paste; module lamination; anti-reflection coating; optical scattering; hemispherical spectral reflectance; short-circuit current; secondary ion mass spectroscopy; ellipsometry; moisture vapor transmission rate; acoustic emissions-based; PVMaT			15. NUMBER OF PAGES	
			16. PRICE CODE	
17. SECURITY CLASSIFICATION OF REPORT Unclassified	18. SECURITY CLASSIFICATION OF THIS PAGE Unclassified	19. SECURITY CLASSIFICATION OF ABSTRACT Unclassified	20. LIMITATION OF ABSTRACT UL	